The Dissolution of Regenerated Cellulose Multifilament Bundles in Ionic Liquid of 1- ethyl-3-methyl- imidazolium acetate [C2mim]+ [OAc]-

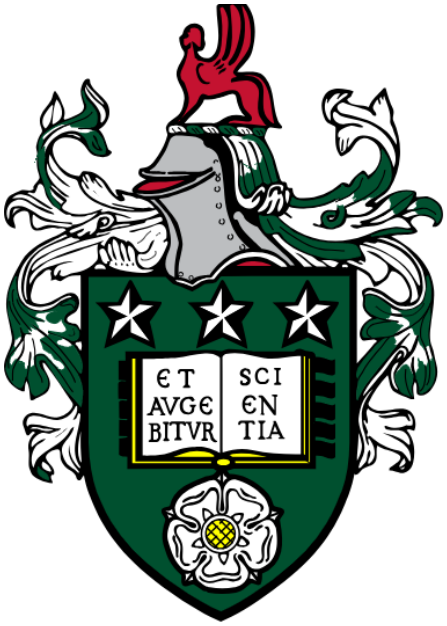

Maer. Hael. Alnazi

Submitted in accordance with the requirements for the degree of

Doctor of Philosophy

The University of Leeds

School of Physics and Astronomy

January, 2024

The candidate confirms that the work submitted is his own, except where work which has formed part of jointly authored publications has been included. The contribution of the candidate and the other authors to this work has been explicitly indicated below. The candidate confirms that appropriate credit has been given within the thesis where reference has been made to the work of others.

Acknowledgements

I am grateful to my supervisors, Mike Ries and Peter Hine, for their ongoing mentorship and never-ending supply of fascinating tasks. Their humble approach to research and science is an inspiration. This approach is evident in their simple but obvious writing style, which I aspire to emulate throughout my PHD journey.

I am forever thankful for my parents, family, husband (Bader) and my children (Basil and Meshari) and my friends (Wafa Ezzawam and Hind Albalawi). Without their encouragement and motivation, I would not have been able to complete this journey.

Special thanks to the university of Tabouk and Saudi Arabia Culture Bureau in the UK for scholarship and funding.

Finally, I would to like to extend my sincere gratitude to all of the participants and friends (Xin Zhang, Yunhao Liang, Danial Baker, James Hawkins, Amjad Alghamdi, Fatimah Albarkati, Samiah Alqarni and Norah Alrefaei) in my study. Their willingness to share their experiences and insights has been invaluable to my research and has helped to make this thesis a success. Thank you for your time and contribution.

Author's Publications

Paper 1: **Dissolution of viscose rayon multifilament yarn in the ionic liquid 1-ethyl-3-methylimidazolium acetate studied using time–temperature superposition.**

Alanazi, M., Ries, M. E., & Hine, P. J. (2023). Dissolution of viscose rayon multifilament yarn in the ionic liquid 1-ethyl-3-methylimidazolium acetate studied using time–temperature superposition. *Cellulose*, *30*(14), 8739-8751.

Authors' contributions: MA: Methodology, formal analysis, investigation, and writing–original draft. MER: Supervision, conceptualization, writing–review & editing, project administration. PJH: Supervision, conceptualization, writing–review & editing, project administration.

Abstract

Regenerated cellulose fibres like Cordenka and Lyocell have been studied for their potential use as reinforcement in polymer composites. These fibres are attractive candidates for improving the mechanical and environmental characteristics of various polymer materials. In our research group we have devolved the idea of manufacturing 'all-cellulose' composites from a single cellulosic source. The idea is to create the 'matrix' of all cellulose composite by selectively dissolving the surface of each fibre or filament, which on coagulation forms the matrix. Being also cellulose, this should give excellent compatibility/adhesion between the phases.

This thesis has studied the dissolution of two commercial regenerated cellulose yarns, namely Cordenka™ and Lyocell™. Optical microscopy, Wide-angle X-ray diffraction (WAXS) and mechanical testing techniques have been used to track the dissolution of these multifilament bundles in the ionic liquid 1-ethyl-3-methyl-imidazolium acetate $[C_2mim]^+$ $[OAc]^-$ for different times and temperatures. This allowed both the speed of the dissolution to be determined at different temperatures as well as the dissolution activation energy E_a from time-temperature superposition.

The different nature of the multifilament bundles (Cordenka™, which was untwisted and Lyocell™ where the bundles were twisted) resulted in different techniques being most suitable for their study. For Cordenka, WAXS and mechanical measurements on partially dissolved composite filaments proved most successful. In the dissolution process, the oriented cellulose II crystals in the regenerated cellulose fibres dissolve and then reform into randomly

oriented crystals to form a matrix phase. This change in orientation enabled the dissolution process to be followed and hence determine the growth of the dissolved matrix fraction of v_m with time and the dissolution activation energy. On the other hand, optical microscopy was found to work very well with the Lyocell multifilament bundles to directly determine the dissolved matrix volume fraction v_m. Mechanical measurements of Young's Modulus and ultimate tensile strength on partially dissolved composites proved successful for both Cordenka and Lyocell multifilament yarns.

The change in the average molecular orientation P_2 determined from an azimuthal (α) X-ray scan, allowed the growth of the matrix volume fraction $v_m$to be calculated with time and temperature. This is an indirect measurement and relies on using a rule of mixtures approach.

The optical microscopic method offered a direct method to measure the growing area of the dissolved and coagulated fraction for the Lyocell multifilament bundle with increasing time and temperature. The twisted fibres meant that the dissolved fraction formed a ring on the outside of the multifilament, allowing a measurement of the decrease of the inner core (the undissolved original fibre fraction) and the increase in the area and thickness of the dissolved and coagulated outer ring. The decrease of the inner core and the growth of coagulation fraction C.F. and the thickness and area of the dissolved and coagulated outer ring was found to follow time temperature superposition, with an Arrhenius behaviour, giving consistent values for the activation energy of E_a= 141 ± 15, E_a= 141 ± 16 and E_a= 127 ± 14 respectively.

Young's modulus and ultimate tensile stringth was measured on all the resulting processed composites for Cordenka and Lyocell multifilament

bundles. The fall of Young's modulus and ultimate tensile strength with dissolution time and temperature was found to follow time-temperature superposition for the Cordenka multifilament bundle, with an Arrhenius behaviour giving a value for E_a= 198± 29 kJ/mol. The Young's Modulus and ultimate tensile strength results were plotted against v_m determined from the WAXS measurements and were found to agree well to the Voigt upper bound parallel Rule of Mixtures. This suggests that the resulting composites are well bonded and that the dissolved Cordenka material (which has a higher molecular weight compared to the Lyocell material) is a suitable matrix material for to make all a cellulose composite.

For the Lyocell multifilament bundle, the Young's modulus of the processed composites was found to be quite scattered and so it could not be ascertained if this followed time-temperature superposition. However, the fall of the ultimate tensile strength of the composites with dissolution time and temperature was found to follow time-temperature superposition, with an Arrhenius behaviour giving a value for Ea= 144± 27 kJ/mol. The ultimate tensile strength results plotted against v_m determined from the optical microscopic method was found to lie significantly below the Voigt rule of mixtures. This suggests that either the dissolved Lyocell material is less successful as a matrix, or that the twisted nature of the Lyocell multifilaments does not allow dissolution to happen in the interior of the bundle as the ionic liquid cannot penetrate.

In terms of the difference between the Cordenka and Lyocell multifilament bundles, it was found from the Optical microscopic results, that the geometry of the Cordenka multifilament bundle is untwisted with a few hundred individual

multifilaments, which appeared as a loose microstructure with significant inner spaces in between. On the other hand, the geometry of Lyocell multifilament bundle is twisted with few hundred individual fibres that are close to each other without significant inner spaces. The Cordenka multifilament bundle has higher average orientation, and a higher Young's modulus, ultimate tensile strength, and activation energy compared to the Lyocell multifilament bundle, which we attribute to the fibres being untwisted. The Lyocell bundle has lower average orientation, which was shown to be due to the significant twist of the bundle.

These findings, especially the geometry and molecular weight lead to the Cordenka multifilament bundle having a faster dissolution rate than the Lyocell multifilament bundle. The comparative geometry (untwisted fibres), the speed of dissolution and the higher molecular weight, lead to the important result that the Cordenka multifilament bundle would make an excellent basis for an all-cellulose regenerated fibre composite (ACC). However, it is appreciated that if woven cloth is to be used to manufacture all-cellulose composites (ACC) then some degree of twist will be required to stop the individual fibres from breaking during the weaving process, so there is maybe an optimum bundle twist to be discovered in any future work.

Table of contents

Contents

List of Tables

List of Figures

Preface

[C2mim][OAc]: 1-ethyl-3-methylimidazolium acetate.

WAXD: wide angle X-ray diffraction.

ILs: ionic liquids.

NMMO: N-methylmorpholine-N-oxide monohydrate.

NaOH: Sodium hydroxide.

TTS: time-temperature superposition

$C.F$: coagulated fraction.

Vm: Matrix Volume fraction.

Vf: fibre volume fraction.

Ea: activation energy

t: time

R: gas constant

A: Area

σ: Ultimate stress

p: force

x: Thickness

ε: strain

Δl: difference in length

T: dissolution temperature.

lo: original length

E: Young's modulus.

$P2$: Orientation degree.

σ_{UTS}: Ultimate tensile strength

Chapter 1 Introduction

1.1 Cellulose.

Cellulose is a natural polymer found in plants and is the most abundant organic polymer on Earth [1]. It is a polysaccharide and can be extracted from various plant materials such as flax and cotton. It also found in wood in combination with other materials such as hemicellulose and lignin [4, 5].

Cellulose has garnered significant attention over the last two decades [6, 7] due to the growing emphasis on renewable resources, sustainable techniques, and the need to reduce environmental pollution caused by fossil fuel-based polymers like traditional plastics [8-11]. Cellulose is a renewable resource and can be used in sustainable production of fuels and other materials due to its low cost and biodegradability [12]. It has a highly ordered, crystalline structure [13-15], composed of β-1,4-linked D-glucose residues, as shown in Figure 1.1 [12, 16, 17] and discovered by Anselm Payne in 1838 [12, 18].

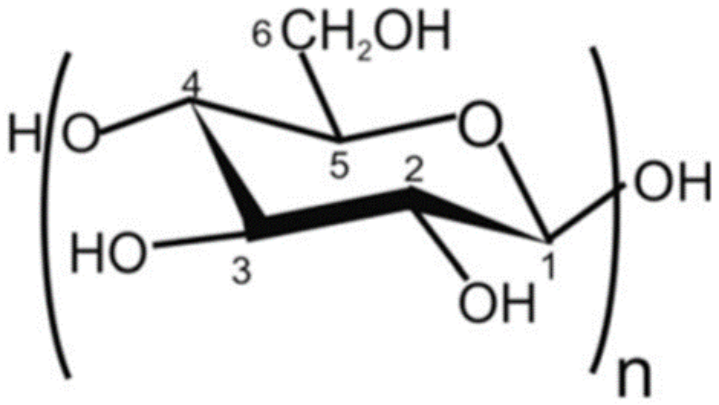

Figure 1.1: The cellulose structure of single glucose unit, taken from ref [19]

1.1.1 Cellulose Literature Background.

Cellulose is a naturally occurring polymer made up of repeating units of glucose. Each unit consists of a six-carbon pyranose ring, with an oxygen atom at the C5 position and an aldehyde functional group. There are several different allomorphs of cellulose, including cellulose I and cellulose II, which are the most common polymorphs [20].

Cellulose is a long chain of glucose molecules linked by glycosidic bonds [12]. These chains are attracted to each other by inter and intra hydrogen bonds, forming a stiff and strong crystal structure. The cellulose fibres are held together by weak van der Waals forces and are insoluble in water due to inter and intramolecular hydrogen bonding between the hydroxyl groups [21, 22]. The long chains of cellulose form helical microfibers, and the cellulose fibres are divided into two regions, a crystalline region called microcrystalline and an

amorphous region within a crystalline material where the atoms or molecules are arranged in a more disordered configuration [4, 12].

The intermolecular hydrogen bonding in cellulose is formed between the hydroxymethyl (-CH_2OH) groups on one molecule and the carbonyl oxygen atoms on another molecule. The energy orientations and positions of the hydroxymethyl groups relative to the pyranose ring in the glucose units can affect the strength and pattern of these hydrogen bonds, leading to the different physical properties of cellulose I and cellulose II[23]. Cellulose I (most often found in nature) has a parallel highly, ordered arrangement of chains [24]. There are two main phases of Cellulose I, known as Iα and Iβ, which are determined by the position of the hydroxyl groups on the glucose units. The ratio of Iα to Iβ can vary depending on the source of the cellulose. Both Iα and Iβ can be found within the same microfibers of cellulose crystals [25].

The β configuration in tunicates and plants is a specific arrangement of glucose units in a mono-clinic unit cell called the β crystal. This crystal has two chains, and every second glucose unit is flipped 180 degrees, with the hydroxyl group at C_1 on the opposite side. The glycosidic bond 1 – 4 is formed between C_1 of one pyranose ring and C_4 of the next pyranose ring, joining them with a single oxygen atom. This leads to the extraction of water molecules and the formation of acetal linkages, which are created from the reaction of an alcohol and a hemiacetal. The α configuration in bacterial and algal cellulose, such as in Valonia, is characterized by a triclinic unit cell and a single chain of β-1,4-linked glucose units. The glycosidic bond between C_1 of one pyranose ring and C of the next ring forms, with the hydroxyl group at C_1 on the same side of the ring, which results in a "right-handed" helical structure.

This configuration is common in natural cellulose fibres, and is responsible for its high strength and crystallinity. [12, 20].

The hydroxyethyl group is a functional group that consists of a hydroxyl (-OH) group attached to an ethyl (-C2H5) group as shown in Figure 1.2a. The confirmation of energy orientation has three substituents: trans-gauche (tg), gauche-trans (gt), and gauche-gauche (gg). The torsion angle between certain atoms in the molecule (O_5-C_5-C_6-O_6 and C_4-C_5-C_6-O_6) determine the conformation, with a 180-degree rotation resulting in the tg conformation, and 60-degree rotations resulting in the gt and gg conformations. These conformations also affect the formation of intermolecular hydrogen bonds between oxygen atoms in the molecule. as shown in Figure 1.2b [3].

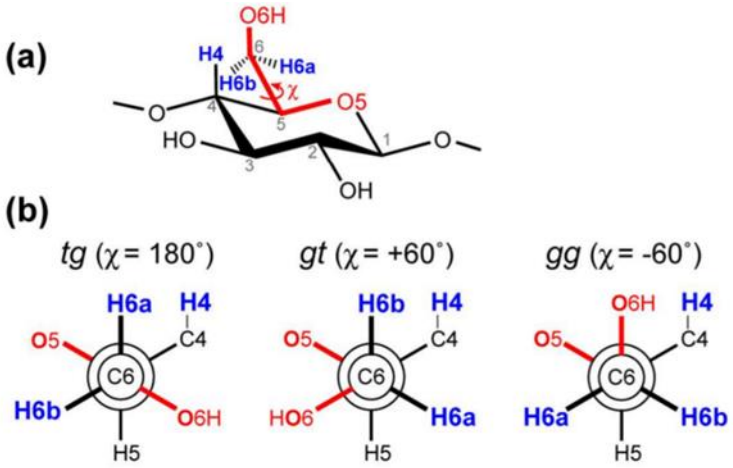

Figure 1.2: a) the hydroxyethyl group is a functional group that consists of a hydroxyl (-OH) group attached to an ethyl (-C2H5) group. It can exist in different rotational positions, such as tg, gt, and gg. The tg conformation can form intermolecular hydrogen bonds between the oxygen atoms O(2) and O(6), as indicated by the blue dashed lines. These hydrogen bonds are absent in the gt and gg conformations. Additionally, the tg conformation can also form an intermolecular hydrogen bond between the oxygen atoms O(3) and O(6), as indicated by the black dashed line taken from ref [3].

The hydroxy groups in cellulose make it hydrophilic, allowing it to interact readily with water, while the CH groups contribute to its hydrophobic nature, leading to interactions with other hydrophobic compounds [26]. Bj¨orn Lindman in 2010 found that the number of hydroxyl groups that have protons capable of forming hydrogen bonds is less than the number of oxygen atoms that would like to form such bonds. As a result, when hydrogen bonding is the only interaction, cellulose should be highly soluble in the presence of excess water [27]. Cellulose is an amphiphilic polymer that exhibits amphiphilic self-assembly. This phenomenon is well-documented for surfactants, lipids, and

block copolymers [28, 29]. Lindman et al., hypothesized that the ability of a polymer system to dissolve in water can be influenced by its amphilicity and tendency to self-organize. For instance, within cellulose, the hydrophobic sides of the structure tend to stick to each other in an aqueous environment, which ultimately causes a decrease in solubility.

Björn concluded that cellulose is amphiphilic, meaning it has both hydrophobic and hydrophilic properties. This is often the case with many natural polymers, including cellulose. Amphiphilic molecules have portions that are attracted to water (hydrophilic) and portions that repel water (hydrophobic). The idea that the low aqueous solubility of cellulose is primarily due to hydrophobic interactions is a reasonable hypothesis. Hydrophobic interactions occur between non-polar (hydrophobic) parts of molecules and are the driving force behind the aggregation of such molecules in aqueous solutions. However, Burchard et al.'s criticism highlights an important point. The dissolution of cellulose is a complex process involving multiple intermolecular forces, including the hydrogen bonds: Cellulose molecules contain hydroxyl (OH) groups, which can form hydrogen bonds with water molecules. These hydrogen bonds need to be disrupted for cellulose to dissolve in water. Van der Waals Forces, these forces are attractive forces between molecules due to fluctuations in electron density. Van der Waals forces play a role in cellulose dissolution [30]. Hydrophobic Interactions: As mentioned, hydrophobic interactions play a role in cellulose solubility, especially if there are hydrophobic regions within the cellulose molecule or in its interactions with other molecules. The interplay between these forces is indeed intricate. Initially, hydrogen bonds between water and cellulose need to be broken for

cellulose to dissolve. After these bonds are disrupted, hydrophobic interactions can become more important in stabilizing the dissolved cellulose [27]. The relative significance of these forces can vary depending on factors such as temperature, cellulose structure, and the concentration of cellulose and other solutes in the solution. In essence, both Bjorn's perspective and the criticism from Burchard et al. highlight the complexity of cellulose dissolution and emphasize that it is not solely driven by one type of intermolecular interaction. The relative importance of hydrogen bonds, Van der Waals forces, and hydrophobic interactions can depend on the specific conditions and context of the cellulose dissolution process [27-29].

1.1.2 The Comparison Between Structure of Cellulose I and Cellulose II.

Cellulose I and Cellulose II are two different conformations of cellulose, a complex carbohydrate that is the main component of plant cell walls. Cellulose I is considered a "tg" conformation, meaning the orientation of the glucose units in the cellulose polymer is such that the O_2 and O_6 atoms are able to form hydrogen bonds with each other, as well as with the O_3 and O_5 atoms of adjacent glucose units. This results in a stable and rigid structure. Cellulose II has a "gt" conformation, meaning the orientation of the glucose units is such that the O_2 and O_6 oxygen atoms are not able to form hydrogen bonds with each other. Instead, the O_3 and O_5 atoms of adjacent glucose units form hydrogen bonds. This results in a more stable and less rigid structure [3, 31, 32] as shown in Figure 1.3.

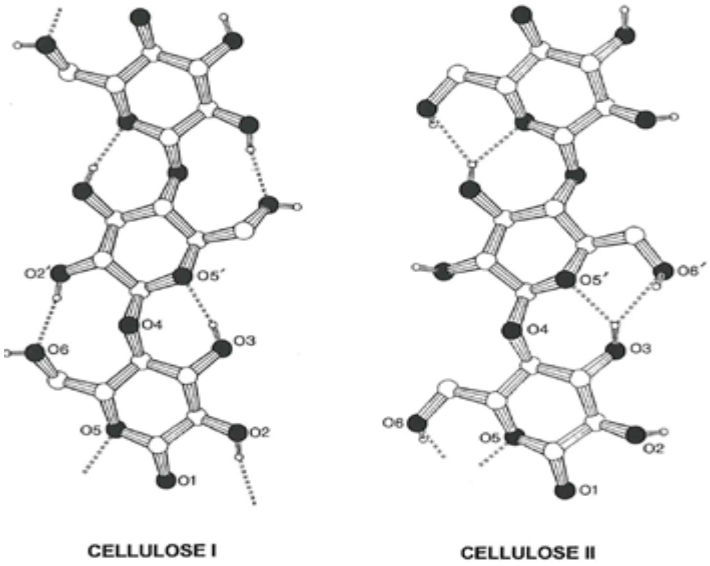

Figure 1.3: The conformation of cellulose I and II chains with hydrogen bond pattern taken from ref [32].

Cellulose II is a crystalline form of cellulose that is more stable than cellulose I. This is because cellulose II has a different structure than cellulose I, with the chains of cellulose molecules folded in an antiparallel configuration, which makes it more difficult to unravel. This increased stability means that cellulose II cannot convert back to cellulose I [20, 31, 32]. In general, naturally occurring materials (e.g. flax, hemp, cotton etc) are predominantly Cellulose I, whereas commercially manufactured fibres (such as those investigated in this thesis) are predominantly Cellulose II as once the natural source is dissolved it will not reform into Cellulose I.

1.1.3 The Mechanism of Cellulose Dissolution.

The mechanism of cellulose dissolution is complex and not fully understood. This is due to these processes depending on various factors and can involve intricate molecular interactions. Cuissinat and Navard's research aimed to understand and categorize the swelling behaviours of wood and cotton fibres in response to solvents**,** as the swelling is a pre-condition of cellulose dissolution. The process of cellulose dissolution often starts with swelling in a solvent system [33], particularly in N-Methylmorpholine N-Oxide (NMMO). Swelling refers to the process in which cellulose fibres absorb and retain a solvent, causing them to expand or swell. This is a crucial step before dissolution can occur. During the swelling process, the molecules of the solvent (for instance, NMMO) penetrate the cellulose structure. This penetration leads to the extension of the cellulose structure. As the NMMO solvent molecules enter the cellulose structure and interacts with the cellulose chains, it can cause changes in the molecular arrangement or chain conformation of the cellulose biopolymer. The cellulose fibres swelling behaviour in solvent system of NMMO depends on cellulose origin, temperature range, the presence of water level in NMMO solvent system and the quality of solvents [34]. The swelling process has identified five distinct modes in the swelling behaviours of fibres. These modes likely represent different ways in which the fibres respond to various solvents or solvent concentrations, which are no swelling and no dissolution and then homogeneous swelling. A large swelling by ballooning, and partial dissolution, to reach completely dissolution and final result saw the fibre disintegration into rod-like fragments [33]. Although this swelling is very important process in

cellulose dissolution, it is worth pointing out that in this work we will only follow the complete dissolution of each individual cellulose II filament.

1.1.4 Mechanism Dissolution of Cellulose in Solvent Systems.

Cellulose has potentially limited applications due to its insolubility in most common solvents. To overcome this limitation, researchers and industries use various methods to dissolve cellulose, making it more versatile for different applications. The two main processing methods for dissolving cellulose are derivatizing solvents and non-derivatizing solvents.

In the derivatizing solvents method, cellulose is first chemically modified or derivatized to make it more soluble. Derivatization involves introducing functional groups onto the cellulose structure, which changes its chemical and physical properties. These functional groups can enhance solubility, leading to the formation of derivatives of cellulose that can be dissolved in specific solvents. Common derivatizing solvents such as DMSO/paraformaldehyde, the N,Ndimethylformamide (DMF)/N2O4, dimethyl sulfoxide (DMSO) and Alkali metal hydroxides [35] can dissolve cellulose by breaking the hydrogen bonds between the glucose units, leading to the formation of a homogeneous solution. The resulting solution can then be used to create various cellulose derivatives, such as cellulose acetate or cellulose ethers.

There are a number of derivatising procedures used to extract cellulose, the most common of which is the viscose process. The viscose process is a chemically produced fibre from the natural substances cellulose. A downside of this process is that it releases carbon disulphide during manufacturing.

Carbon disulphide is known to be toxic and can also have adverse effects on the environment and human health if not handled properly, so this could be a significant disadvantage of this process. Additionally, the viscose process can be time-consuming and complex, as it involves multiple stages and chemical treatments to produce the fibres, this can make the process expensive and less efficient compared to other methods of producing fibres [36].

For the Non-Derivatizing Solvents approach, cellulose is dissolved directly without requiring any chemical modification or derivatization. Non-derivatizing solvents can interact with cellulose and break its intermolecular forces (hydrogen bonds), resulting in the dissolution of the cellulose molecules. Some of the most widely used non-derivatizing solvents are N-Methylmorpholine-N-Oxide (NMMO), ionic liquids, lithium chloride and dimethyl sulfoxide (DMSO) widely used for producing Tencel® fibres [36].

The most common cellulose solvent is NMMO (N-Methylmorpholine-N-Oxide) which can be used as either a derivatizing or non-derivatizing, depending on the specific application and the properties required for the dissolved cellulose.

1.2 Ionic Liquids and Dissolution of Cellulose.

Ionic liquids are attracting attention as a potential green solvent for dissolving cellulose fibres. They are seen as more environmentally friendly than traditional solvents such as N-alkylpyridinium chloride. 1-ethyl-3-methyl-imidazolium acetate has been found to be very efficient in dissolving cellulose and for this reason will be used exclusively in this work. Ionic liquids research

is ongoing to find new and more effective ways of using ionic liquids to dissolve cellulose fibres. [25].

1.2.1 Ionic liquid.

Ionic liquids are a solvent often considered as a green solvent and eco-friendly to the environment. An ionic liquid (IL) is usually defined as a salt which has a melting point below 100 ℃ [16, 37]. Ionic liquids were defined by Walden in 1914 [38, 39]. An ionic liquid has excellent properties which are nontoxicity, recyclability, thermal stability, and low vapour pressure [21, 38, 40, 41], all of which give good ‘green’ credentials.

Ionic liquids have a wide range of potential applications, such as in electro-elastic materials, heat storage, energy, and chemical analysis [29]. However, one limitation of using ionic liquids in industry is that they are relatively expensive to prepare [30].

Ionic liquids are a class of compounds that are composed of ions, typically a positively charged cation and a negatively charged anion. As described above, they have a unique combination of properties such as low vapor pressure, high thermal stability, and non-flammability. They can be used in a variety of applications such as solvents, catalysts, and electrochemical devices. Some common types of cations used in ionic liquids include dialkylimidazolium, N-alkylpyridinium, alkylammonium, and phosphonium. The dissolution of cellulose in ionic liquid was reported initially in 1934 by Graenacher. However, it was found that pyridinium salts have high melting point (118℃–120℃). Therefore, this original patent does not attract much attention [42]. Swatloski

in 2002 found that the dissolution of cellulose was highest in imidazolium based ionic liquid like 1-butyl-3-methylimidazolium chloride, [BIMIM] $[Cl]^-$ [43] due to low viscosity and high thermal stability [44] and have the ability to dissolve cellulose [40].

The ionic liquid 1-ethyl-3-methyl- imidazolium acetate used within this work, is an organic solvent which contains imidazolium cations $[C_2mim]^+$ and, acetate anions $[OAc]^-$ [38, 40, 45]. Figure 1.4 shows the chemical structure of the $[C_2mim]^+$ $[OAc]^-$ solvent. This IL $[C_2mim]^+$ $[OAc]^-$ has good properties such a low melting point and low vapour pressure, as well as being biodegradable [46]. It has the ability to dissolve a high concentration (~20 wt %) of cellulose in certain applications. [47]. It is worth noticing that the purity of the IL could also affect the dissolution due to additional side reactions or derivatizing reactions. [48] caution that additional side reactions with cellulose can occur if the IL contains significant impurities. Furthermore, Zweckmair, T., et al., described how acetylation reactions can occur with cellulose for aged ILs (they studied 1,3-dialkylimidazolium acetate) with resultant impurities. They propose that pure ILs do not show this reaction [49].

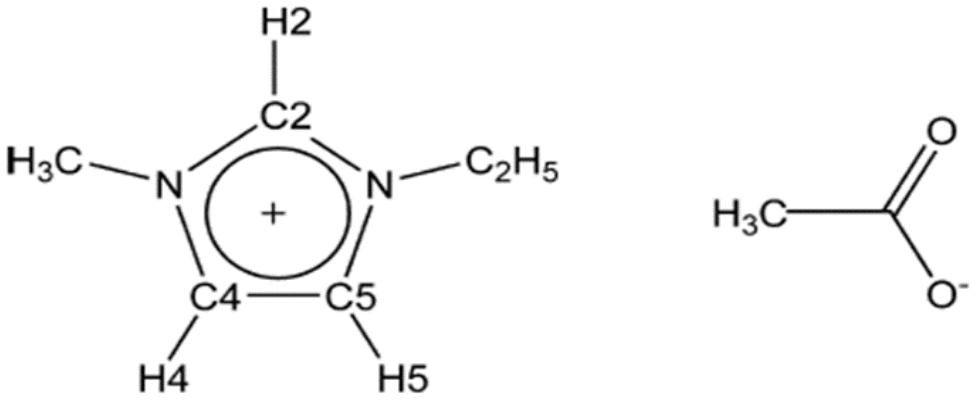

Figure 1.4: the chemical structure of the ionic liquid -1- ethyl-3-methyl- imidazolium acetate $[C_2mim]^+ [OAc]^-$, it taken from ref [50].

1.2.2 Mechanism of Dissolution of Cellulose in 1-ethyl-3-methyl-imidazolium acetate.

Although there is still significant discussion and research in this area, it is usually considered that cellulose dissolution occurs through the interaction of hydrogen bonds between the hydroxyl molecules of cellulose and ions of the ionic liquid [40, 41]. The anions of the ionic liquid interact with the hydrogen atoms of the hydroxyl groups of cellulose and the aromatic protons in the imidazolium cation associates with the oxygen atoms of hydroxy. These interactions lead to the deconstruction of the cellulose chain and the breaking of hydrogen bonds, resulting in the dissolution of cellulose [23, 33]. Figure 1.5 shows an example of the dissolution of cellulose process in ionic liquid.

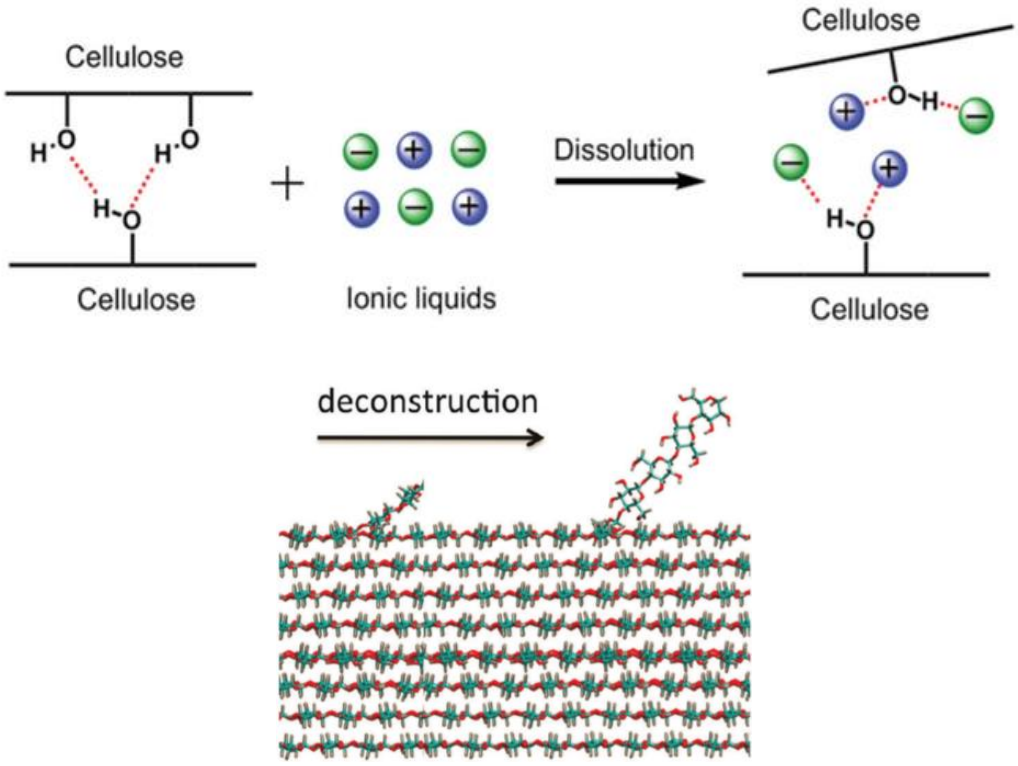

Figure 1.5: the diagram of dissolution of cellulose in ionic liquids, this taken from reference [42].

1.3 Regenerating Cellulose Fibre Manufacturing.

Cellulose fibres have gained popularity in various industries, including in woven textiles, due to their eco-friendly characteristics. One form of cellulosic fibres is known as cellulose II "regenerated cellulose fibre." [51]. Regenerated cellulose is a synthetic polymer produced from natural cellulose (cellulose I) sources such as wood pulp. It is produced through processes such as Viscose and dry-jet wet spinning [42]. It is commonly used in the textile industry to produce materials [43, 44] such as Cordenka and textile fibres [12].

Regenerated cellulose fibre manufacturing involves creating fibres from a natural cellulose source, a natural polymer found in plants. Regenerated

cellulose fibres have a wide range of applications, including textiles, paper, packaging materials, and even some advanced materials like cellulose nanocrystals for high-tech applications [36, 52]. The procedure of regenerating cellulose fibres typically involves the viscose process, or the Lyocell process or dry-jet wet spinning process. In the following section each of these is described in more detail.

1.3.1 Viscose Process

The Viscose Process was discovered by Charles Cross and Edward Bevan in 1892, They were two English chemists who developed this method while working at the Courtauld Institute in London.[53]. The mechanism of the derivatization process is based on a mercerization process to dissolve cellulose and produce cellulose II fibres. The native cellulose is first dissolved in sodium hydroxide. During dissolution, the molecules of sodium hydroxide interact with water molecules and break the intermolecular hydrogen bonds between the cellulose molecules. This leads to a change in the properties and the morphological structure of the native cellulose. The change in morphology of the structure is due to the sodium hydroxide, often termed a mercerization process. In this process, the NaOH solvent swells the spaces between the structure, where the ions diffuse into the crystalline section after swelling the amorphous section between the fibres as shown in Figure 1.6. This phenomenon of mercerization changes the crystal structure under the swollen state from cellulose I to cellulose II without cellulose dissolution [35].

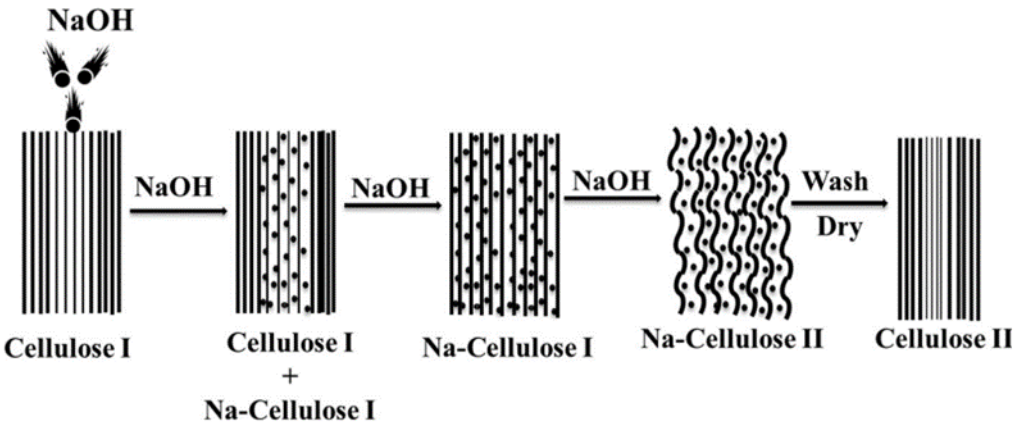

Figure 1.6: The mechanism of derivatization process using the NaOH solvent to swell the inter cellulose fibres, where the ions diffuse into the crystalline section after swell the amorphous section between fibres, to produce cellulose II.

The viscose process, also known as the viscose rayon process, is a method for producing a type of 'artificial' cellulose II - based fibre known as viscose rayon. The viscose process involves chemically treating wood pulp with sodium hydroxide, breaking the hydrogen bonds in the cellulose I structure, and then transforming the resulting alkali cellulose into a viscose solution. This solution is then extruded and regenerated to produce viscose rayon fibres (cellulose II), which can then be used to make various textile products.

The viscose process involves several steps as shown in Figure 1.7, and in more details is as follows: The process begins with wood pulp, which is first treated with a solution of sodium hydroxide (NaOH) and sometimes sodium carbonate (Na2CO3).

This treatment (mercerization) uses sodium hydroxide to swell the cellulose fibres in the wood pulp. Breaking hydrogen bonds, the sodium hydroxide in the solution interacts with the water molecules and with the cellulose molecules in

the wood pulp. Sodium hydroxide is a strong base, and it disrupts the hydrogen bonds that hold the cellulose chains together in their natural structure. This disruption of the hydrogen bonds causes the cellulose fibres to become more soluble in water. The interaction between the sodium hydroxide and the cellulose creates a compound known as "alkali cellulose." Alkali cellulose is a semi-liquid substance that is formed when the cellulose fibres lose their natural crystalline structure due to the disruption of hydrogen bonds. Next, the alkali cellulose is allowed to age, which means it is left to stand for a period of time. During ageing, the properties and morphological structure of the pulp cellulose continue to change. The ageing process is essential for achieving the desired properties in the final viscose product. After aging, the alkali cellulose is treated with carbon disulfide (CS2). This chemical reaction is known as xanthation. Xanthation converts the alkali cellulose into a compound called cellulose xanthate In the next stage, the cellulose xanthate is dissolved in a dilute solution of sodium hydroxide, forming a thick viscous solution known as "viscose." This viscose solution contains cellulose dissolved in sodium hydroxide and is the precursor for making viscose rayon fibres. The viscose solution is then forced through spinnerets into a chemical bath usually containing sulfuric acid (H2SO4) or another acid. This bath causes the cellulose xanthate to be regenerated back into cellulose (II) fibres. As the viscose solution solidifies in the bath, it forms long filaments of cellulose. These filaments can be spun into fibres, which are then processed further to produce viscose rayon textiles. Finally a washing step Is carried out in water on the cellulosic fibres followed by drying to make the regeneration cellulose

Fibre [54]. The regenerated cellulose fibres from viscose prosses have different applications such as clothing, coated fabric, and automobile tyres.

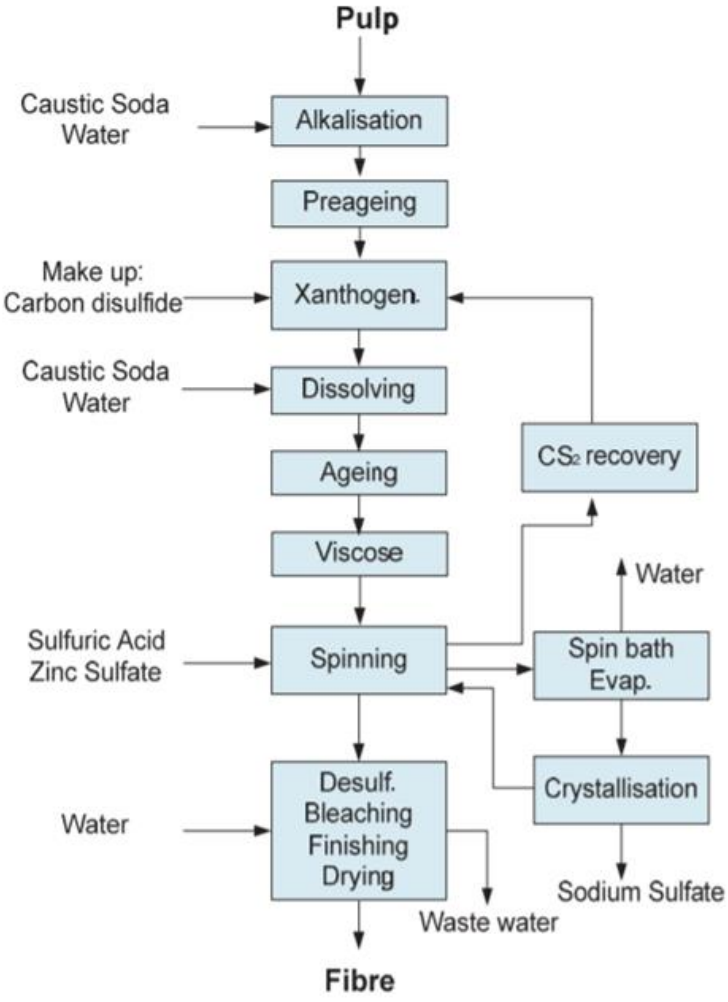

Figure 1.7: Viscose process, taken from ref [54]

1.3.2 Lyocell Process.

The Lyocell process is used directly to dissolve cellulose without requiring activation, and so the obtained cellulose fibres are often classified as eco-environmental. The Lyocell process is based on using two solvents, which are N-Methylmorpholine-Noxide (NMMO) and an ionic liquid, which is used as a non-toxic solvent to dissolve higher capacity of cellulose compared to other solvents like DMSO and DMAC [36, 55]. In this process, the wood pulp is first swelled and then dissolved directly in the NMMO solvent.

The proposed mechanism of swelling and dissolution in NMMO in the production of fibres has been described above in section 1.1.3. In the Lyocell process using NMMO, the activity and strong dipolar of N-O moiety in NMMO leads to the oxygen group interacting with the cellulose units and forming complex intermolecular hydrogen bonds between hydroxyl group of the cellulose chain and the NO group of NMMO. This results in a change in the structure and properties of cellulose and results in a homogenous solution. The production of lyocell fibre is shown schematically in Figure 1.8. In this method, the resulting homogenous solution is spun and stretched in the air gap in the filament form. After that, the fibres are regenerated after coagulation in a mixture of a water/NMMO spin bath, and then washed and dried.

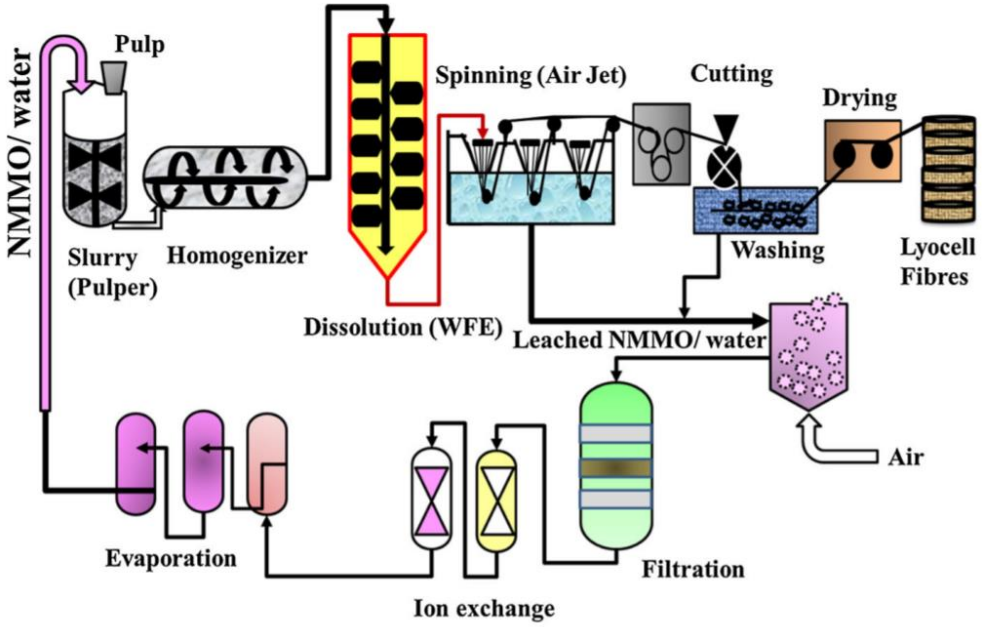

Figure 1.8 : Diagram of lyocell process and this taken from ref [55]

1.3.3 Dry-jet wet Spinning Process.

This procedure using ionic liquid of 1-ethyl-3-methyl-imidazolium Diethyl phosphate [EMIMDEP] with co-solvent of DMSO, to dissolve cellulose and form solution. The solution transfers into the extruder, then, the air bubbles are removed from the solution by using a vacuum oven at a temperature of 80°C. After heating, the solution is injected into holes with a diameter of 150 μm into a water bath for coagulation. There is an air gap of 3cm between the water bath and the nozzle, allowing the extruded filament to dry for a short time, as shown in Figure 1.9. The resulting fibre reaches the winding unit with a fixed velocity of 2.1 m/s. Subsequently, the fibre is immersed in water for 48hrs , to remove ionic liquid from fibre [56].

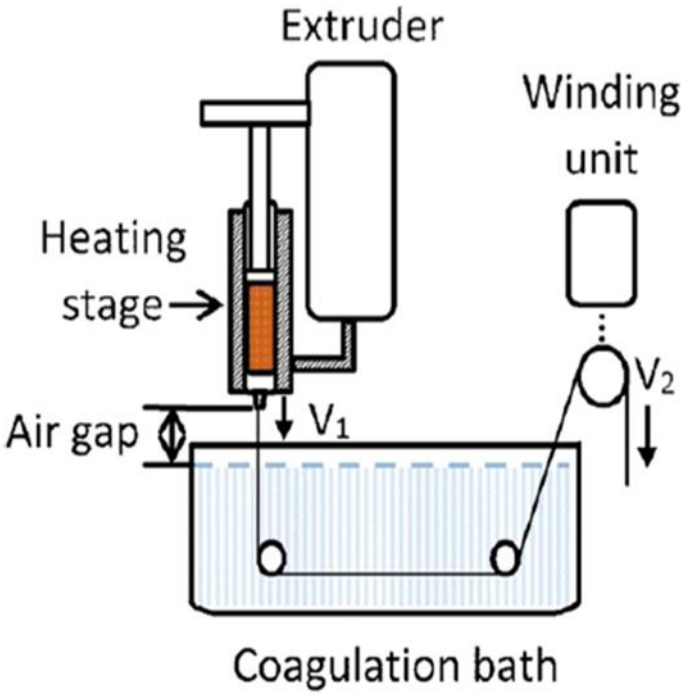

Figure 1.9: Dry-Jet wet process. This taken from ref [56]

1.4 Regenerating Cellulose Fibres.

In the 21st century, renewable resources of fibre materials have been gaining significant attention from researchers as they can offer low environmental impact, low carbon usage and can be biodegradable [57, 58]. Regenerated cellulose fibre is a man-made fibre of cellulose II. It is regenerated from natural cellulose I fibre sources such as wood pulp and has found many uses to produce textile materials in the industrial area [54, 59]. All regenerated cellulose fibres may be produced as continuous filament yarns and two most common are named Cordenka and Lyocell [36]. These two different regenerated cellulose II fibres have been studied extensively in this work.

1.4.1 Cordenka Fibre.

Cordenka fibre is a man-made cellulose fibre derived from wood pulp through the viscose process. It was originally developed by Glanzstoffweke, a German company, in 1938. Cordenka fibres are characterized by their exceptional properties, particularly their ability to withstand high temperatures and stress. This makes them valuable for various applications, especially those requiring durability and stability under challenging conditions. [60].

The unique combination of properties that Cordenka fibres offer has allowed them to play a significant role in enhancing the performance and durability of various products across multiple industries. These properties of Cordenka fibres are heat resistance and high tensile strength, which makes them suitable for applications that involve heavy loads or stress. These fibres are resistant to a range of chemicals, adding to their versatility in different industrial settings. Given these properties, Cordenka fibres have found applications in various industries: one of the most notable applications is in the automotive sector. Cordenka fibres are used in car tires to reinforce and enhance their durability, contributing to better performance and longer lifespan. They are also utilized in automotive brake hoses for their strength and heat resistance. Cordenka fibres are incorporated into rubber goods such as conveyor belts, hoses, and other industrial products. Their reinforcement capabilities enhance the mechanical properties of these products. The high tensile strength and heat resistance of Cordenka fibres make them suitable for use in composite materials. These composites can be used in aerospace, construction, and other industries where lightweight and durable materials are crucial [61].

1.4.2 Lyocell (Tencel) Fibre.

Lyocell fibre is a man-made cellulose fibre produced using the Lyocell process. The first fibre was produced commercially in 1948. The name of Lyocell fibre has been derived from Greek word (lyo), which means dissolve and cell from cellulose. In 1989, The name of Lyocell was recognised by (International Bureau for the standardization of Rayon and Synthetic Fibres, Brussels) (BISFA) and the Federal Trade Commission (USA). There are two types of lyocell on the market. The Lyocell name is used for technical or industrial application and Tencel name used in clothes applications. Tencel fibre is green fibre and friendly for the environment.

Lyocell fibre, often marketed under the brand name Tencel, is indeed a unique and versatile textile material that combines the advantages of both natural and synthetic fibres. This is primarily due to its production process, which involves the regeneration of cellulose from wood pulp in an organic solvent. Lyocell's eco-friendly production process, which uses a closed-loop system to recycle solvents, makes it a popular choice for environmentally conscious consumers and designers looking to incorporate sustainable materials into their creations. Its versatility in terms of texture, appearance, and performance has contributed to its adoption in a wide range of clothing styles and fabric types [36].

1.5 All Cellulose Composites

The combination between different constituents with different properties , is known as a composite material [62] . The first work on cellulose based composite materials was done by the Nishino group in 2004, to make all

cellulose composite. All cellulose composite (ACC) is combination between fibre and matrix of cellulose material. The Nishino group found that during composite processing they faced an issue which was a low quality of adhesion between the fibre and the matrix [63]. This issue caused by mixing the difference components of fibres and matrix [64-66]. To solve the adhesion issue the cellulose was used as a reinforcement to get cellulose composite with excellent physical properties such as tensile strength and elastic properties [67, 68].

There are procedures applied to make all cellulose composite, where called as one and two steps. The first processing starts by partially dissolving the fibre in solvent, then removing the solvent by using water and then drying. The Nishino group applied a two-step approach based on first making a cellulose and ionic liquid solution (which will form the matrix phase), then adding cellulose fibre to this solution to weld between matrix and fibre composite [8, 11, 69].

1.6 Project Objectives and Aim.

Regenerated celluloses have drawn attention, since they are easy to fabricate, have low toxicity, are biocompatible, biodegradable, and are thermal and chemically stable. These properties make regenerated cellulose fibers a sustainable and popular choice in various industries, including textiles, healthcare, and packaging, where eco-friendly materials are sought after to reduce the environmental footprint of products.

Regenerated cellulose fibres like Cordenka and Lyocell have been studied for their potential use as reinforcement in polymer composites. These fibres are attractive candidates for improving the mechanical and environmental characteristics of various polymer materials. When used as a reinforcement, they can enhance the strength, stiffness, and other mechanical properties of polymer composites while maintaining some of the environmental benefits associated with regenerated cellulose fibres [70-73]. However, there can be compatibility/adhesion issues when using a cellulosic fibre with a traditional polymeric matrix.

For this reason, in our research group we have devolved the idea of manufacturing ‘all-cellulose’ composites from a single cellulosic source. The idea is to create the ‘matrix’ of all cellulose composite by selectively dissolving the surface of each fibre or filament, which on coagulation forms the matrix. Being also cellulose, this should give excellent compatibility/adhesion between the phases. To date we have studied the dissolution process (exclusively in the ionic liquid 1-ethyl-3-methyl- imidazolium acetate) in natural cellulose fibres, such as flax, hemp and cotton [74-78]. In this work we want to build on that work with, for the first time, a fundamental study of the dissolution kinetics of cellulose II regenerated fibres.

To effectively control the properties of potential future all cellulose (II) composites, it is crucial to have a comprehensive understanding of the dissolution process for these regenerated cellulose fibres. There are some key aspects to consider in understanding the dissolution procedure. The solvent selection such as which solvents can effectively dissolve cellulose without causing damage or degradation is essential. In terms of a final ‘all-cellulose

composite' the fraction of initial fibres and generated matrix will lead to different properties, such as strength or stiffness. Dissolution temperature and time will undoubtedly be important in terms of controlling these parameters and can allow for fine-tuning the dissolution procedure and ultimately the fibre/matrix fraction. This is because higher temperatures can accelerate the dissolution, but they may also affect the properties of the resulting cellulose solution [79-83].

The processes of dissolution mechanism can vary depending on the factors as mentioned above.

In this thesis, the aim was to study for the first time, the dissolution of two different cellulose II regenerated fibres (in terms of multifilament bundles), namely Cordenka (untwisted) and Lyocell (twisted). These had different molecular weight and also larger scale architectural geometry differences (untwisted and twisted) because of the different production processes. The aim was to study the dissolution with time and temperature, using a variety of techniques such as wide-angle x-ray diffraction, optical microscopy, and mechanical measurements. It will be seen that the speed of dissolution was found to depend on the macroscopic bundle geometry. Most importantly, the dissolution was found to depend on both time and temperature, and that for all measurements, dissolution master curves could be formed using time-temperature superposition (TTS). This allowed, for the first time, a dissolution activation energy (Ea) to be determined for these two regenerated cellulose II fibres.

Chapter 2 Background and Experimental Methods.

2.1 Material and processing.

2.1.1 Material and sample preparation of composite multifilament.

In this thesis we have studied two commercial regenerated fibres, whose tradenames are Cordenka® filaments 0506 provided by Bristol University and Tencel Lyocell™ woven fabric purchased from Atelier de Production et de Création fabric (A.B.C.). All the dissolution experiments used the ionic liquid 1-ethyl-3-methyl- imidazolium acetate $[C_2mim]^+$ $[OAc]^-$ with purity 95% which was purchased from Sigma Aldrich. It is worth noting that the purity of the IL (95% in our case) could also affect the dissolution due to additional side reactions or derivatizing reactions. [48] caution that additional side reactions with cellulose can occur if the IL contains significant impurities. Furthermore, [49] describe how acetylation reactions can occur with cellulose for aged ILs (they studied 1,3-dialkylimidazolium acetate) with resultant impurities. They propose that pure ILs do not show this reaction.

The unprocessed Cordenka multifilament bundle (which were untwisted) as shown in Figure 2.1a and the unprocessed Lyocell multifilament (which were twisted), which extracted firstly from woven clothes as shown in Figure 2.1b.

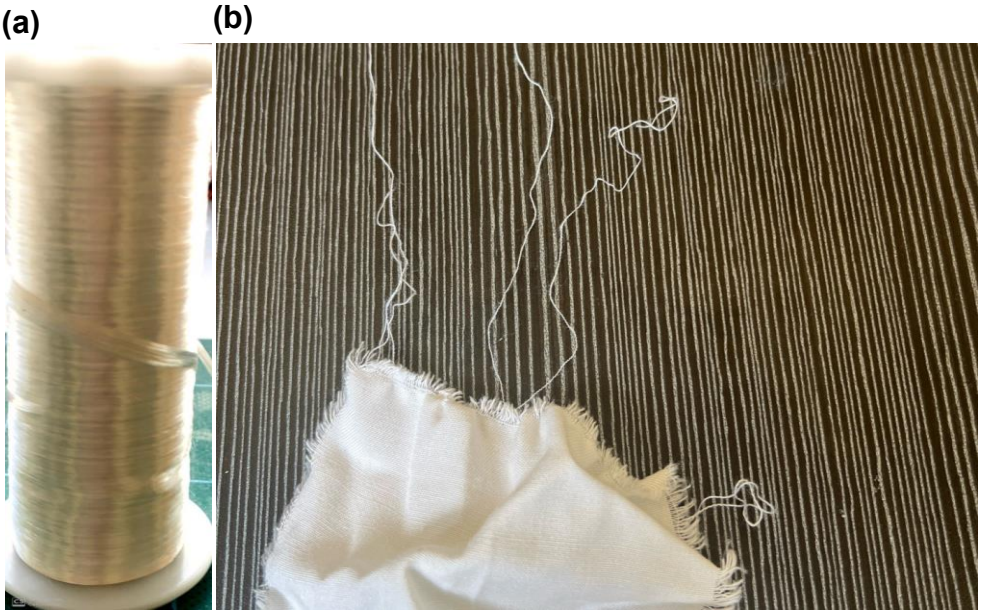

Figure 2.1: a) The unprocessed Cordenka multifilament bundle (which were untwisted). b) the unprocessed Lyocell multifilament, which were (twisted).

The Cordenka and Lyocell multifilament bundle underwent the same dissolution experiment, as shown schematically in Figure 2.2. For the Cordenka, six multifilament bundle samples were fixed at both ends in an 8 cm x 8 cm poly(tetrafluoroethylene) (Teflon) frame, three for the x-ray diffraction and optical microscopy experiments and three samples for mechanical measurements. Alternatively, for Lyocell, fourteen multifilament bundle samples were fixed at both ends in an 8 cm x 8 cm poly(tetrafluoroethylene) (Teflon) frame, eight for the x-ray diffraction, three for optical microscopy experiments and three samples for mechanical measurements. A PTFE dish containing the IL $[C2mim]^+[OAc]^-$ was preheated in a vacuum oven at 1hr for each processing temperature (30, 35, 40, and 45 ℃). After this preheating step the frames were put into the dish of IL $[C_2mim]^+$ $[OAc]^-$ and then left in the vacuum oven at the same temperature for

a range of chosen set times. The last step was to wash (and coagulate) the processed partially dissolved composite filaments while still on the frames to remove all the ionic liquid by soaking in water for 24 hrs, followed by a final drying process on a hot plate at 120℃ for 1hr.

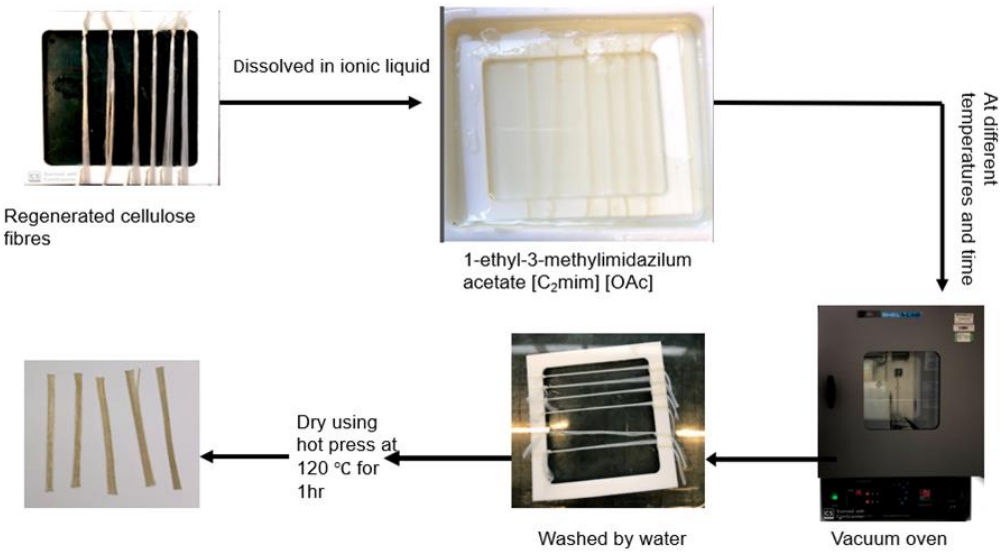

Figure 2.2: Dissolution procedure for Cordenka filaments.

The Cordenka multifilament bundle samples were partially dissolved in the IL $[C_2mim]^+$ $[OAc]^-$ at various temperatures and for different times as follows: at 30℃, for 1,2,3 and 5 hrs, at 35℃ for 30 mins,1,2,3 and 5 hrs, and at 40℃ for 1,2 and 3hrs. Finally, 45℃ for 30mins, 1 and 1.30 hrs. For the Lyocell multifilament bundle, were partially dissolved in the same IL of $[C_2mim]^+$ $[OAc]^-$ at 30℃, for 1,2,3,5 and 8 hrs, at 35℃ for 30 mins,1,2,3,4 and 5 hrs, and at 37℃ for 1,2 and 3hrs, and at 40℃ for 30 min,1, 1.5 and 2hrs. Finally, 45℃ for 30mins, 45min and 1hrs.

2.1.2 Preparation of Film Sample.

For preparing a fully dissolved sample (which is proposed as representative of the matrix phase of the partially dissolved filaments), the Cordenka multifilament bundles were cut into small pieces and then submerged into $[C_2mim]^+$ $[OAc]^-$ with a magnetic stirrer at a speed of 90 rpm, for 48 hrs at 90℃ on a hot plate, as shown in figure 2.3a. The solution had a total concentration of 19:1 IL $[C_2mim]^+[OAc]^-$ to cellulose filaments. The IL/cellulose solution was then spread evenly into a 5 cm x 5 cm polystyrene petri dish and left for 30 mins in a vacuum oven at 90℃, to remove any bubbles from the film. This petri dish with solution was put on an upside-down beaker, and then put it in a larger beaker filled with water and sealed, heated at 90℃ using a hot plate, for 24 hrs as shown in Figure 2.3b. The water was evaporated slowly inside the beaker to slowly condense and so coagulate the film. The resultant film was then washed with water for 24 h, to remove any residual ionic liquid. We are making the assumption that after washing the residual IL is at a significantly low enough fraction to not affect mechanical properties, giving a resultant film with a light-yellow colour as shown in Figure 2.3c and finally this film was dried at 120℃ for one hour, using a hot press machine under a minimal contact pressure. This film is considered to be similar to the matrix phase within the composite Cordenka multifilament.

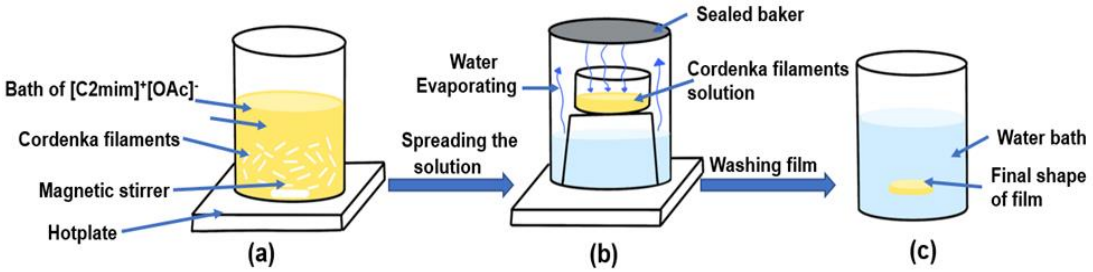

Figure 2.3: The preparation of Cordenka film.

2.2 X-ray Diffraction.

The principle of the X-ray diffraction technique is based on the constructive interference of an incident X-ray beam, which are reflected from different crystal layers and scatter at specific angles from single crystal planes of a material. This causes high intensity peaks in the spectrum. For an amorphous material, which has less order than crystalline regions, a broad peak is observed [84]. Braggs law [85, 86] describes this diffraction as:

$$2d \sin\theta = n\lambda \tag{2.1}$$

where *d* is a distance between planes, θ is the angle of the diffracted beam, n is an number to indicate the order of reflection, and λ is the wavelength of X-ray [85, 86]. The measurement of X-ray diffraction can give accurate information of the crystalline structure of a cellulose-based material [1, 87].

The main mechanism of X-ray diffraction interactions between a material and the X-rays are coherent scattering, Compton effect, absorption, and the photoelectric effect. Theoretically, in the coherent scattering, the X-ray photons interact with the whole atoms of the material. This excitation causes the atom to release an X-ray photon with the same wavelength but, does not necessarily

travel in a different direction. However, the wavelengths of photons are equal and there is no change in the energy level.

Compton effects refer to the interaction of X-ray photons with inner-shell electrons. The photon causes an atom to lose an electron, which is leaving it in an ionized state and X-ray scattering in a different direction with less energy. During the interaction of Compton scattering, the ejection electrons may have enough energy left, which causes more ionization reactions before losing more energy. In Compton scattering, the X-ray photons can be scattered in any direction, and when they scatter back in the same direction as the original photons, this is called back scatter. In the photoelectric effect, when the photons interact with the inner shell of electrons and causing the electrons to be ionized, then electrons released with enough energy from atom, known as photoelectrons. This interaction may refer to the photoelectric absorption since photon is completely absorbed[88].

2.2.1 X-ray Diffraction Techniques.

2.2.1.1 Deconvolution (curve fitting) method.

The commonly used techniques to determine the cellulose crystallinity, include peak height and deconvolution (curve fitting) procedures. Deconvolution (curve fitting) procedures are techniques used to determine the cellulose crystallinity. The deconvolution process is considered more accurate than the peak height method as it can distinguish between cellulose I and II fractions as well as the amorphous fraction of cellulose-based materials. This method

works by Voigt functions, which are based on the convolution of Gaussian-Lorentzian distribution [89].

The chain and crystallographic planes for native cellulose are shown in Figure 2.4a. There are $1-10, 100 \text{ and } 020$ planes, which indicate to the different lattice spacing between these planes of cellulose [90]. Figure 2.4b shows intensity profile of an X-ray 2θ scan [91] corresponding crystal planes $(1\bar{1}0, 100 \text{ and } 200)$ of the cellulose I unit cell. Following deconvolution, three Bragg peaks are shown of cellulose I located at 14.8° and 16.5° and 22.2° assigned to the $1\bar{1}0, 110 \text{ and } 200$ planes respectively. The reflection at 18° is assigned to the amorphous phase [92, 93]. It is possible to determine the crystallinity degree from the sum of the fitted crystalline peaks of cellulose to the total area of crystallinity and amorphous under the diffractogram, through the deconvolution (curve fitting) equation:

$$C = 100 * \frac{I_{1\bar{1}0}+I_{110}+I_{200}}{I_{1\bar{1}0}+I_{110}+I_{200}+I_{amorphous}} \ [\%] \qquad (2.2)$$

Where $I_{1\bar{1}0}$ is the area for the first crystallinity peak of the sample with reflection plane $1\bar{1}0$ from Miller index, I_{110} and I_{200} are the area for crystallinity peaks with reflection plane 110 and 020 from Miller index and $\mathrm{I}_{\mathrm{amorphous}}$ is the area of amorphous peak [1].

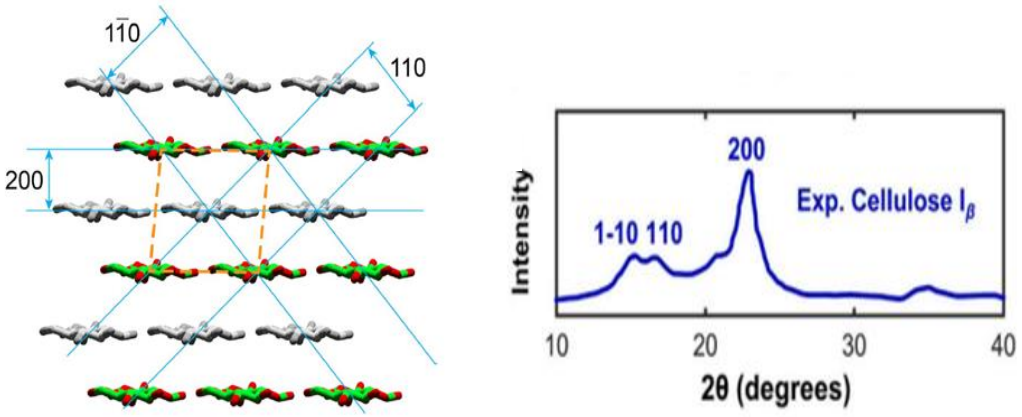

Figure 2.4: a) the lattices spacing planes of cellulose I unit cell taken from ref [94]. b) Diffraction pattern of cellulose I shows peak deconvolution. The diffraction pattern has three major reflections at $1\bar{1}0$, 110, and 200 for the crystalline phase taken from ref [91].

2.2.1.2 Peak height method.

The peak height method proposes that the crystalline fraction can be determined by the ratio of the height of the main cellulose I crystal peak to the height of the amorphous background. Peak height method applied to calculate the ratio of crystallinity, C, by this equation:

$$C = 100 * \frac{I_{200} - I_{amorphous}}{I_{200}} \ [\%] \qquad (2.3)$$

The parameter I_{200} indicates the highest cellulose I peak height at the 200 reflection (2θ = 22.2°) and $I_{amorphous}$ is the diffraction peak height of the non-crystalline material [1] usually chosen as the position between the main crystalline peaks, so a 2θ angle of 18°. Figure 2.5 shows typical positions of these two peaks.

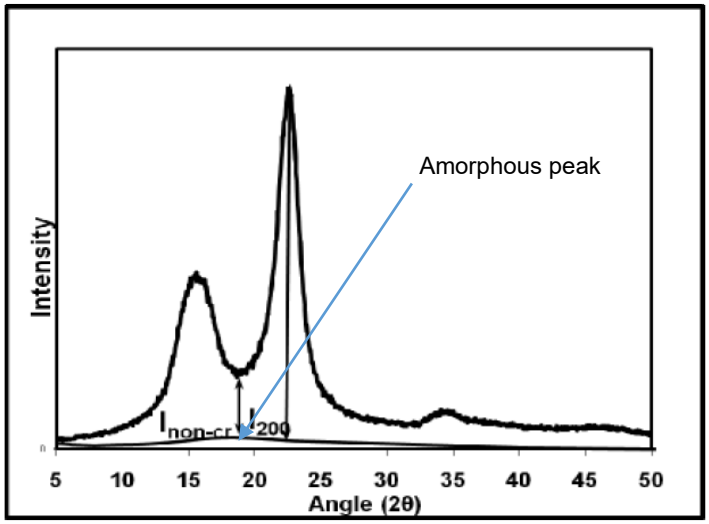

Figure 2.5: The position of crystallinity and non-crystallinity peaks taken from ref [1].

Figure 2.6 shows the difference between the position peaks of cellulose I and II. The three main crystalline peaks of Cellulose I are shifted due to the change in crystal structure during dissolving process to cellulose II. In the change from cellulose I to cellulose II, the $1\bar{1}0$reflection moves down to 12.4° and the 110 reflection moves up to 20. The main 200 peak also moves down slightly from 22.2° to 21.8° [2, 95]. For cellulose II and regenerated cellulose, the 110 and 200 Bragg peak often form a single broad peak centred around 21°.

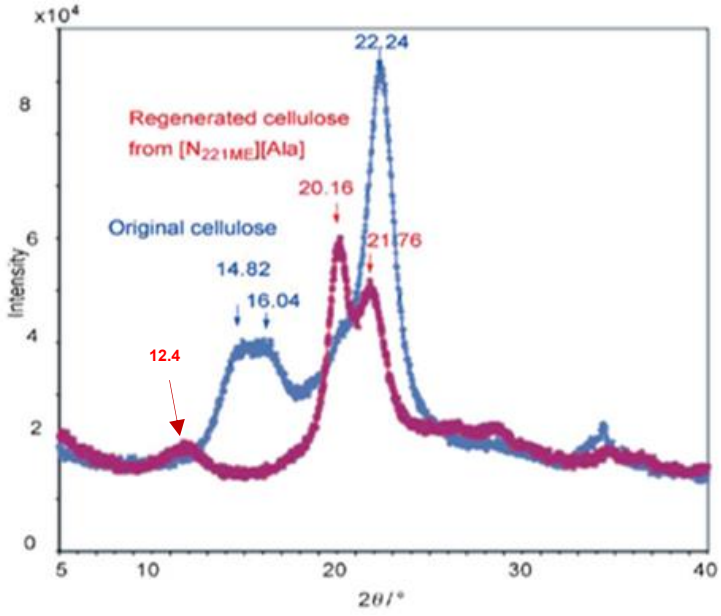

Figure 2.6: The positions of crystallinity peaks of original cellulose I and regenerated cellulose II taken from ref [2].

2.2.2 Molecular Orientation.

The orientation distribution proposed by Herman [56] can allow the molecular level (i.e crystalline) orientation to be determined using the orientation function P_2. The orientation function is defined as the second order coefficient of a series of Legendre polynomials. The order parameter or orientation function P_2 used to evaluate the orientation in polymer material like film and fibres is calculated using equation 2.4 [96],

$$f = <P_2(\cos\alpha)> = (3 < cos^2\alpha > -1)/2 \qquad (2.4)$$

where (f) is Herman's orientation factor function of the crystalline orientation of molecules. α is the angle between the crystal axis and reference direction and $<\cos\alpha>$ indicates the all average orientation in the sample [56]. When

f =1 this indicates that the crystallites have perfect alignment, and when f = 0.25 the crystallites are completely randomly oriented in a 2D plane, and in the case of f = -0.5 crystallites are oriented perpendicular to the axis of the sample [97]. An azimuthal intensity distribution $I(\alpha)$ (at a fixed value of 2θ often chosen as the highest peak in a 2θ scan such as shown in Figure 2.6) allows the P_2 coefficient to be calculated. In this work this is often at a 2θ value of 21.4°. The relationship between the P_2 coefficient and the angular position of orientation distribution $I(\alpha)$ is that measured using x-ray, the degree of orientation can be determined using experimental equation 2.5.

$$< cos^2\alpha >= \sum_{-90}^{+90} \left(\frac{I(\alpha)\, cos^2\, \alpha\, d\theta}{I(\alpha)\, d\theta} \right) \quad (2.5)$$

2.2.3 Experimental method of Wide-Angle X-ray Diffraction.

The degree of orientation and the crystal structure of the unprocessed multifilament bundle, the completely dissolved film, and the composite samples of Cordenka and Lyocell were determined using Wide-Angle X-ray Diffraction (WAXD) with Cu Kα radiation (λ = 1.54 Å) at 40 kV and 30 mA (DRONEK 4-AXES, Huber Diffractions Technik GmbH & Co. KG, Germany). The 2θ scan from Bruker D8 Diffractometer with monochromate Cu Kα radiation, were scan run in Gonio (Bragg-Brentano) mode to get diffraction pattern with high resolution of Lyocell multifilament bundle.

2.2.3.1 X-Ray Diffraction (Analogue).

Qualitative measurements of the change in crystalline structure and orientation were obtained by capturing a 2D image of each sample. This was done by passing x-rays through the sample and capturing the resulting 2D pattern on an x-ray sensitive film placed 5 cm away. The exposure time was 3 hours for Cordenka multifilament bundle and 4 hours for Lyocell multifilament bundle.

2.2.3.2 X-Ray Diffraction (Digital).

Quantitative measurements of crystal structure and orientation were carried out using a Huber goniometer and x-ray detector. The 2θ equatorial scans were carried out from 5° to 40° using a counting time of 40 seconds per step (0.1°) with the partially dissolved composite multifilament bundle located in the vertical direction as shown in Figure 2.7. The 2θ curves were obtained by subtraction of a background scan carried out with no sample loaded. This allowed the crystalline structure to be confirmed and then enabled the choice of the most appropriate Bragg peak for the circumferential scans. The orientation degree of the crystals was then determined by setting the 2θ angle at 20.3° and 2θ was then kept fixed, which is the position with the maximum count rate and so has the best signal/noise ratio. This was not at the position of a particular Bragg peak, but as described above, was the maximum signal due to the overlap of the 110 and 200 Bragg peaks which are close together for cellulose II. Circumferential α scans were carried out at increments of 5° with a counting time of 30 seconds per step, with azimuthal angles α from -90°

to +90° as shown in Figure 2.8. In this work, no background subtracted for α scans were 2θ kept fixed.

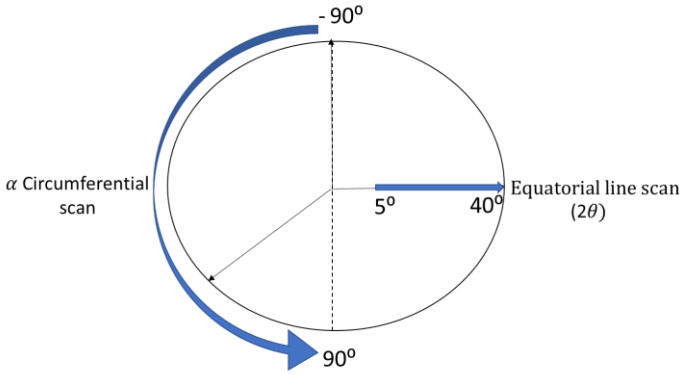

Figure 2.7: A schematic diagram to show the WAXD for 2θ and α scans, blue lines indicate the respective paths.

For the circumferential α scan, a number of processed composite multifilament bundle were placed vertically side by side in the WAXS sample holder to increase the signal to noise ratio. The crystal structure of the Cordenka multifilament bundles is changed due to the dissolving process, transforming from an aligned crystalline structure in the original unprocessed multifilament bundle to randomly oriented crystals in the dissolved and coagulated phase. Experimentally, the Azimuthal α scan is used to measure the combined average orientation of the crystal structure of the processed composite multifilament bundle. Once the intensity distribution is measured, we can determine an average orientation of the crystals (coming from the unprocessed multifilament bundle and the dissolved matrix phase) $(cos^2\alpha)$ by using equation 2.5. The average orientation of the processed Cordenka composite multifilament bundle can then be further quantified using the second-order coefficient of Legendre polynomial P_2 (cos α) using equation

2.4. This procedure was done on all samples which are the Cordenka and Lyocell composite multifilament bundles.

The changes in the average crystalline orientation (P_2) with processing time and temperature will be shown in later sections to be an excellent indication of the degree of dissolution and so to allow the activation energy of dissolution to be determined via time-temperature superposition. Additionally, the change in the values of (P_2) can also be used as an alternative method to determine the dissolved fraction of the fibres (v_m equation 2.7) with time and temperature by assuming a rule of mixtures again. We assume that the orientation of the multifilament bundle (P_{2c}) is a sum of the orientation of the original multifilaments (P_{2f}) and a completely dissolved sample (P_{2m} = 0.25 for a random 2D orientation) weigthed by their volume fractions, v_f and v_m as follwo

$$P_{2c} = P_{2f}v_f + P_{2m}v_m \tag{2.6}$$

where P_{2c} indicates the P_2 value of the processed composite multifilament bundle, P_{2f} is the P_2 value of the original unprocessed multifilament bundle (measured as = 0.57) and P_{2m} is the P_2 value of the completely dissolved matrix film with 0.25 (randomly oriented crystals). and assuming $v_m + v_f = 1$, gives

$$v_m = \frac{P_{2c} - P_{2m}}{P_{2f} - P_{2m}} \tag{2.7}$$

2.3 Mechanical Measurements.

2.3.1 Tensile test.

The mechanical performance of a polymer material is usually investigated by stress-strain measurements. The tensile test is a common technique used to measure the mechanical properties of a polymer. The mechanical test investigates the mechanical properties of materials through the correlation between stress and strain. A typical stress- strain curve is as shown in Figure 2.8. This technique is based on clamping the ends of a sample in a loading frame and then applying a constant displacement rate to the sample and measuring the resulting force [84]. Stress and strain are defined using the following equations:

$$\sigma = \frac{p}{A}. \tag{2.8}$$

$$\varepsilon = \Delta l / l_0 \tag{2.9}$$

where σ indicates the stress, from the measured force (p) applied to a finite area *A*, which is the area of cross-section of the sample. A particular value of the stress is the nominal stress at fracture (σTS) which is derived from the measured force to break the sample and the original cross section area. From equation 2.9, ε the strain, is given by the l_0 the original length of the sample and Δl is the increase in length after the force is applied. Again, the strain at break is given by the extension to break the sample divided by the original length. The load extension data was converted into stress-strain curves. The results were gotten after repeating the measurements three times to reduce random errors.

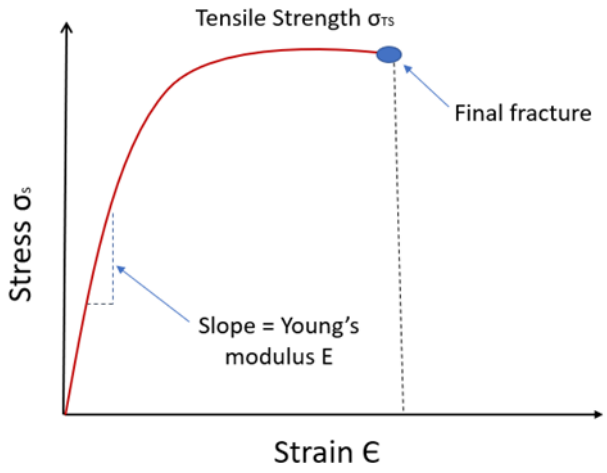

Figure 2.8: The typical curve of stress and strain of mechanical test.

The initial linear stress-strain region indicates an elastic region. The slope of this initial stress and strain gives a Young's modulus E as given by [84].

$$E = \sigma/\varepsilon \tag{2.10}$$

2.3.1.1 Experimental method of Tensile test.

The Young's modulus E and ultimate stress (σ) were measured using an electromechanical tensile machine Instron 5564 with the Bluehill™ version software employed. The load cell was 2000 N and a crosshead speed of 10 mm/min was used. The cross-section area (A m^2) of each composite filament was determined using a gravimetric technique measured by equation (2.11).

$$A = \frac{m}{l\,\rho} \tag{2.11}$$

where l is the length of fibre and ρ is the density of cellulose, which has been recorded as 1400 kg/m^3 [98, 99], *m* is the mass of filaments. Figure 2.9 shows a Cordenka multifilament bundle as an example of the experimental set up. End tabs, to give good load transfer, were formed using paper and superglue as shown in Figure 2.9a. The sample to be tested was then fixed between two clamps with sandpaper, after measuring the gauge length as presented in Figure 2.9b. Young's modulus and ultimate stress measurements were repeated three times for each set of processing time and temperature to reduce human error and sample to sample variability. This procedure was done on all samples, i.e. the Cordenka and Lyocell processed composite multifilament bundles.

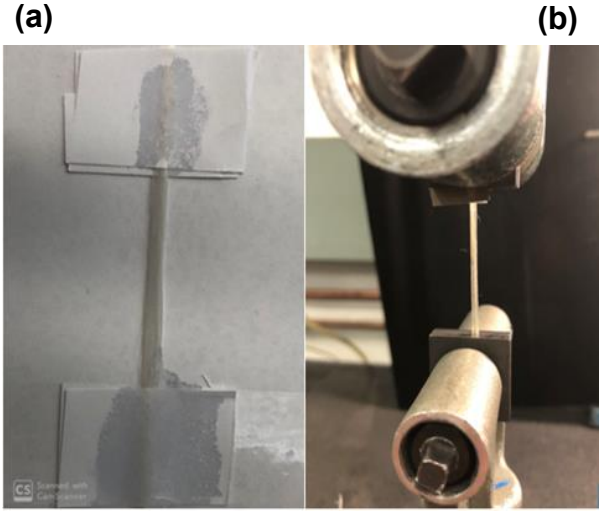

Figure 2.9: a) the sample of Cordenka multifilament bundle using glue and b) the sample between two clamps in electromechanical tensile machine Instron 5564.

2.3.2 Three-point Bending Test.

Three-point bending flexural tests were applied to only a coagulated Cordenka film sample. Then, ultimate tensile strength and Young's modulus of film sample were determined. The load extension data was converted into stress-strain curves. To calculate the Young's modulus, the stress and strain were calculated using these equations:

$$\sigma = 3PL/2bh^2 \tag{2.12}$$

$$\varepsilon_f = 6Dh/L^2 \tag{2.13}$$

where σ is the stress and ε_f maximum strain at the outer surface at mid span, P is applied force, L is support span, D is mid-span deflection b is width of film and h is thickness of film sample. With substitution between equations 2.12 into 2.13 gives equation 2.14 with slope of the force deflection curve, m, to calculate the flexural modulus as:

$$E_f = mL^3/4bh^3 \tag{2.14}$$

2.3.2.1 Experimental method of Three-Point Bending Test.

An electromechanical tensile machine Instron 5564 with the Bluehill™ version software in a compression mode with a 10 KN calibrated load cell. This method was used instead of a tensile test due to the film sample being too brittle to be gripped. The three-point bending flexural tests performed with a crosshead speed at 2 mm/min and a bending span of 20 mm. The thickness and width of

the film sample were measured first by using micrometre then the measuring started. The setting of this experiment is shown in Figer 2.10.

The three-point bending flexural modulus was calculated, after the load extension data was converted into stress-strain curves. The results obtained after repeated the measurements three to reduce random errors. The flexural stress and the flexural strain were calculated at the outer surface of the test specimen at mid-span by using Equations 2.12 and 2.13, subsequently. The three-point bending flexural modulus of the sample can be calculated using Equation 2.14. All errors were calculated from the standard deviation σ as σ/ $\sqrt{n}$, where n is number of measurements.

Figure 2.10: The setting of carrying out three-point bending test.

2.3.3 Rule Of Mixtures.

The rule of mixtures is often used to predict the overall modulus of a composite consisting of two phases (fibre and matrix) based on their individual properties and their respective volume fractions. The upper-bound is known as the Voigt prediction, which is also called the parallel rule of mixtures, while the lower-bound is termed the Reuss (series) prediction. The upper bound and lower bound can be useful for estimating the effective stiffness of two phases of fibre and matrix composites. The Voigt series assumes that the two composite phases have the same strain, while the Reuss series assumes the two phases of composite have the same stress [100, 101]. The upper-bound and lower-bound are calculated by the following equations respectively:

$$E_{VOIGT} = E_m v_m + E_f(1 - v_m) \quad (2.15)$$

$$E_{REUSS} = \frac{1}{(1-v_m)/E_f + {v_m}/{E_m}} \quad (2.16)$$

In this work we have evaluated how the partially dissolved filaments compare to the prediction from the Voigt model. For the multifilament fibre bundles investigated in this work, the fibres are all in the same direction (either untwisted or twisted). Therefore, if the partially dissolved cellulose forms an effective matrix between these fibres, then we would expect the Young's modulus of the 'composite' to follow the parallel rule of mixtures.

In fact, we sometimes go further and assume that the partially dissolved fibres do follow the parallel rule of mixtures and hence use equation 2.17 to predict the fraction of dissolved fibres.

Therefore, in equation 2.15 E_{VOIGT} indicates the Young's modulus of the partially dissolved composites in the fibre direction, E_f is the Young's modulus of the original 100% unprocessed filament bundle and E_m of a completely dissolved 'matrix' film. Assuming $v_m + v_f = 1$, where v_m is term the matrix fraction for processed filament and V_f is unprocessed filament fraction then the volume fraction $v_m$of a processed filament can be calculated by employing the experimental data of Young's modulus E, through the parallel rule of mixture equation (2.17) [102] given as:

$$v_m = \frac{E_C - E_f}{E_m - E_f} \tag{2.17}$$

2.4 Optical Microscopy and Experimental Method.

The cross-section area of all the processed composite multifilament bundle at different times and temperatures and unprocessed multifilament bundle samples (Cordenka 0506, Lyocell) were measured, using an Olympus BH2 microscope in conjunction with a CCD (Charge-coupled device) camera. The multifilament bundle was embedded vertically in a mould, which was then filled with epoxy resin after mixing the resin and the harder (EpoxiCure, BUEHLER) in a ratio of 4:1, and left until fully cured. This was then ground and polished to allow the cross section of the various samples to be examined in reflective light is shown in Figure 2.11.

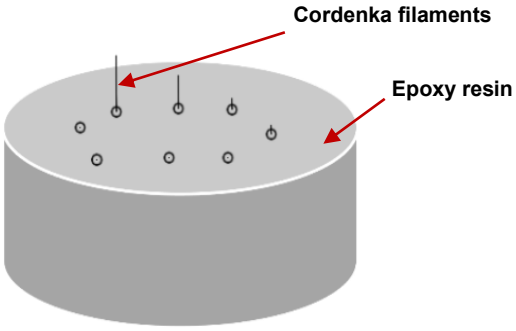

Figure 2.11: Schematic of unprocessed and processed multifilament bundle with Epoxy Resin.

For this partially dissolved Cordenka multifilament bundle sample, it can be seen that there's no external dissolved and coagulated layer in the optical micrograph (Figure 2.12a). While in the partially dissolved Lyocell multifilament bundle sample, it can be seen that there are two different regions in the optical micrograph (Figure 2.12b). These are the inner core of multifilament bundle (whose boundary is shown by the yellow line) and an outer, clear, layer surrounding (whose boundary is shown by the green line) shown in Figure 2.12b. The outer layer is proposed as the dissolved and coagulated fraction During the dissolution process, the twisted Lyocell multifilament bundle acts more as a single element, as previously seen with work in our research group on flax and cotton fibres [76, 103].

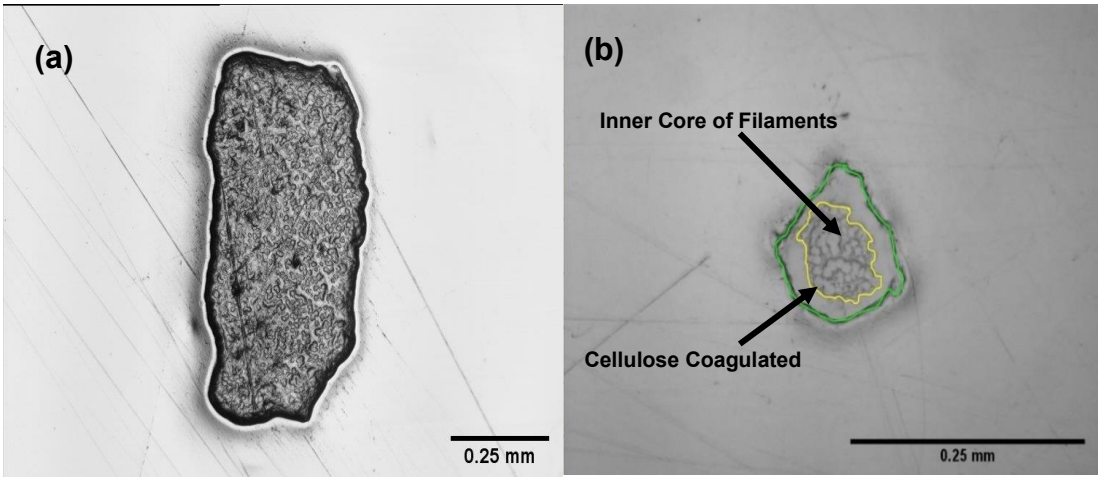

Figure 2.12: a) A typical optical micrograph for partially dissolved of Cordenka multifilament bundle showing no boundaries around the coagulated layer of cellulose and b) a typical optical micrograph for processed composite multifilament bundle of Lyocell showing boundaries around the coagulated layer of cellulose (green line) and inner core of filaments (yellow line). Multifilament shown were dissolved at 40 °C for 2 hours for Cordenka and Filaments shown were dissolved at 37 °C for 3 hours for lyocell.

The area of these two regions in the Lyocell material, that is the inner core, and the outer perimeter of the coagulated filaments were measured using ImageJ software. The ratio between the coagulated outer layer and inner core of filaments gives the coagulation fraction ($C.F$) and is calculated using equation 2.18.

$$C.F. = \left(\frac{A_T - A_C}{A_T}\right) \tag{2.18}$$

Where $C.F.$ is the coagulation fraction, A_T is total area of the cross section and A_C is the area of the filaments comprised of coagulated cellulose. The optical microscopy technique could not be used for the Cordenka multifilament bundles as no construct between the matrix and fibre. This mean no external

dissolved and coagulated layer in the optical micrograph and there are not different regions in the optical micrograph. Therefore, we cannot use the Image J to measure the Coagulation fraction.

2.5 Activation energy analysis by Arrhenius Law.

Molecules move with thermal energy, which can be used to bend, stretch, and ultimately break bonds, which leads to chemical reactions. The breaking bonds can occur when the molecules are moving fast, this means the molecules have enough kinetic energy to collide with proper orientation such that a chemical reaction occurs to form new product. An extra energy is a minimum amount of energy required to activate molecules, known as the activation energy, E_a [104]. The activation energy and the chemical reaction can understand by enthalpy change reaction system, ΔH, where H, is eventually lowered by the overcoming of an energy barrier as shown in Figure 2.13. When the products have a lower enthalpy than the reactants, the react called exothermic. The enthalpy change (ΔH) is negative, indicating that energy is released into the surroundings. In this reaction, the energy required to break the bonds in the reactants and the energy released when new bonds form in the products.

In the endothermic reaction, the products have higher enthalpy than the reactants. The enthalpy change (ΔH) is positive, indicating that energy is absorbed into the surroundings. In this reaction, the energy required to break the bonds in the reactants and the energy absorbed when new bonds form in the products. The activation energy is still the minimum amount of energy required for the reaction to take place, but in this case, it is the energy required

to get the reactants to the transition state, where the old bonds are half-broken, and the new bonds are half-made [105].

The activation energy is related to viscous flow and interaction between molecules. In liquid and polymer systems, molecules undergo rotational and translational motion. In this transition the molecules move from current lattice position (non-equilibrium state) before flowing to neighbouring position (equilibrium state) in vacancy or hole to overcome the energy barrier [106, 107].

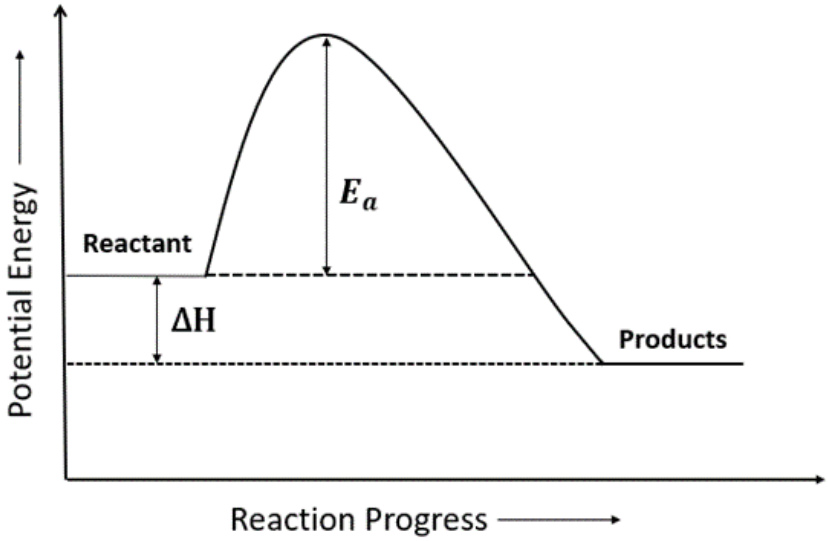

Figure 2.13: The energy diagram for system following the Arrhenius law.

Mathematically, the Arrhenius law can be applied to calculate the activation energy. The Arrhenius equation is frequently used for analysing the reaction rate of chemicals based on the change of temperature by calculating the activation energy, though:

$$k = Ae^{\frac{-E_a}{RT}} \tag{2.19}$$

where Ea is the activation energy, k is the rate constant, A the pre-exponential factor (a reaction-based constant), R the gas constant and T the temperature in Kelvin. Throughout this work, the logarithm of the Arrhenius equation was used by plotting ln(k) vs T^{-1} resulting in a straight line of a gradient -E_a/R and intercept ln(A), as given by equation (2.20) [108, 109].

$$Lnk = \left(\frac{-E_a}{R}\right)\left(\frac{1}{T}\right) + LnA \tag{2.20}$$

2.6 Measurement of weight-average molecular weight and molecular weight distribution

As we did not have the appropriate equipment, the molecular weight measurements of our two samples were done by Prof. Antje Potthast, University of Natural Resources and Life Science, Vienna, Austria. They described the technique they used as follows:

The molecular weight (M_w) and number-average molecular weight (M_n) of the unprocessed Cordenka 0506 and unprocessed Lyocell multifilament bundles were measured with the technique of multi-angle laser light scattering (MALLS) [110, 111]. The solution used for injection was prepared as follows First, the unprocessed Cordenka multifilament sample was soaked in water before the solvent was exchanged from water to dimethylacetamide, DMAc to activate the pulp samples. The sample was kept for 20 hours in the dimethyl sulfoxide, DMSO and then fully dissolved in a 9% solution of DMAc/ LiCl. Prior to injecting the sample was diluted with DMAc. This method was also applied for unprocessed Lyocell multifilament bundle, and each sample was measured twice.

Chapter 3 Dissolution of Cordenka multifilament bundle in the Ionic liquid of 1- ethyl-3-methyl- imidazolium acetate.

The work in this chapter has been published as follows: Alanazi, M., Ries, M. E., & Hine, P. J. (2023). Dissolution of viscose rayon multifilament yarn in the ionic liquid 1-ethyl-3-methylimidazolium acetate studied using time–temperature superposition. *Cellulose*, *30*(14), 8739-8751.

3.1 Introduction.

Cordenka® 056 is a commercial regenerated cellulose man-made fibre (of the termed rayon), usually in the form of a multifilament bundle comprised of many individual fibres. Cordenka fibre is considered to be an eco-environmental material. Commercial Cordenka multifilament bundle was first produced by Glanzstoffweke in 1938. Cordenka multifilament bundle have excellent mechanical properties, which include high temperature resistance and the ability to take high stresses. Therefore, commercial Cordenka multifilament bundles have been used in a variety of commercial applications including car tyres, automotive brake hoses and rubber goods [60].

This chapter will study the dissolution of a Cordenka multifilament bundle in the Ionic liquid of 1- ethyl-3-methyl- imidazolium acetate [C2mim]+ [OAc]-. Three technical methods were utilised: optical microscopy, wide angle X-ray diffraction and mechanical measurements. During the dissolution process, the oriented crystals in the multifilament bundle are transformed into randomly

oriented cellulose crystals after dissolution and coagulation. Wide angle x-ray diffraction was used to determine the change in the average crystalline orientation (specified by the Herman's Orientation factor P_2) which then allowed the rate of dissolution to be measured with time and temperature. This follows the change in the average crystal orientation using an azimuthal (α) X-ray scan by measuring the 2nd Legendre polynomial function (P_2). Similarly, the change in the Young's modulus and ultimate strength of the partially dissolved and regenerated 'composites' with time and temperature were also measured. The reduction in both parameters (Young's modulus and (P_2)) with time and temperature were found to follow time-temperature superposition [112], allowing the activation energy of dissolution to be calculated independently by these two methods. In addition, the two measurements were combined to show that the modulus of the partially dissolved regenerated 'composite' filaments followed closely to the rule of mixtures. The ultimate aim of the research will be to manufacture all cellulose composites from regenerated cellulose fibres, although this is not reported in this current work, where the focus is to understanding the physics of the dissolution process and how to use this in the future, to control and tailor composites properties.

3.2 Results and discussion.

3.2.1 Optical Microscopy.

The results of the Cross-sectional optical microscopy are shown in Figure 3.1. It can be noted that, unprocessed Cordenka multifilament bundle consists of a few hundred individual multifilament bundle which appears as a loose

microstructure with significant inner spaces. The Cordenka multifilament bundle was not twisted and so when incorporated into epoxy resin, the multifilament bundle was found to move apart due to the ingress of the resin as seen in Figure 3.1. This ‘untwisted’ geometry is important as it also controls the dissolution as the IL can easily penetrate the multifilament bindles and access each individual multifilament.

Experimentally, the overall cross-sectional size of the processed multifilament bundle stays roughly constant with dissolution time and temperature an associated increase of matrix proportion during the dissolution process. In unprocessed multifilament bundle, the multifilament is not connected and untwisted with significant inner space as shown in Figure 3.1a. Even at 30℃ for 1 hour there is enough dissolved matrix to stick the fibres together and stop them from separating when placed into epoxy as shown for unprocessed Cordenka multifilament bundle. It can be seen that the images for 1 ,2 and 3hrs are similar but by 5 hrs, there is a significantly higher fraction of the dissolved and coagulation matrix.

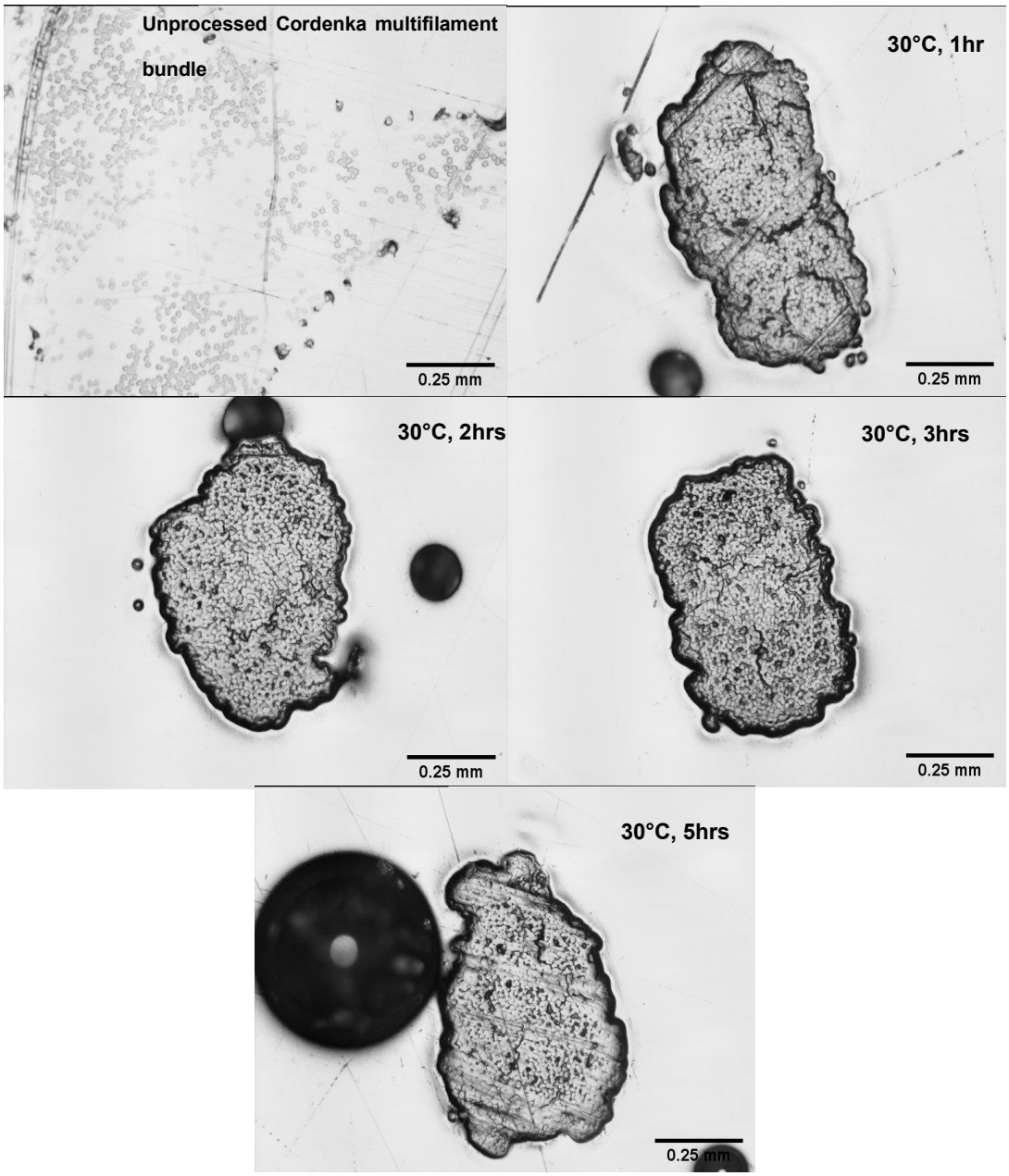

Figure 3.1: Microscopy cross-sectional images of Cordenka multifilament bundle at 30℃ for different times.

The dissolution rate decreases with time and temperature at 35℃, 40℃ and at 45℃ as the inner space between the individual multifilament bundle is filled with a dissolved cellulose/[C_2mim] [OAc] gel at 35℃ 40℃ and 45℃, we propose that this forms a barrier to the ionic liquid and therefore the dissolution proceeds more slowly by dissolving the multifilament bundle from the outside

of the fibre bundles and so proceeds at a lower rate as shown in Figure 3.2 at 45℃. It can be noticed that at 0.5 hr, the internal spaces are all filled but no external ring of matrix exists and at 1-hour nice ring of dissolved matrix and at 1.5 hrs fibres almost all dissolved. These three relate to a dissolved fraction of 30%, 60% and 75% respectively from the P_2measurements.

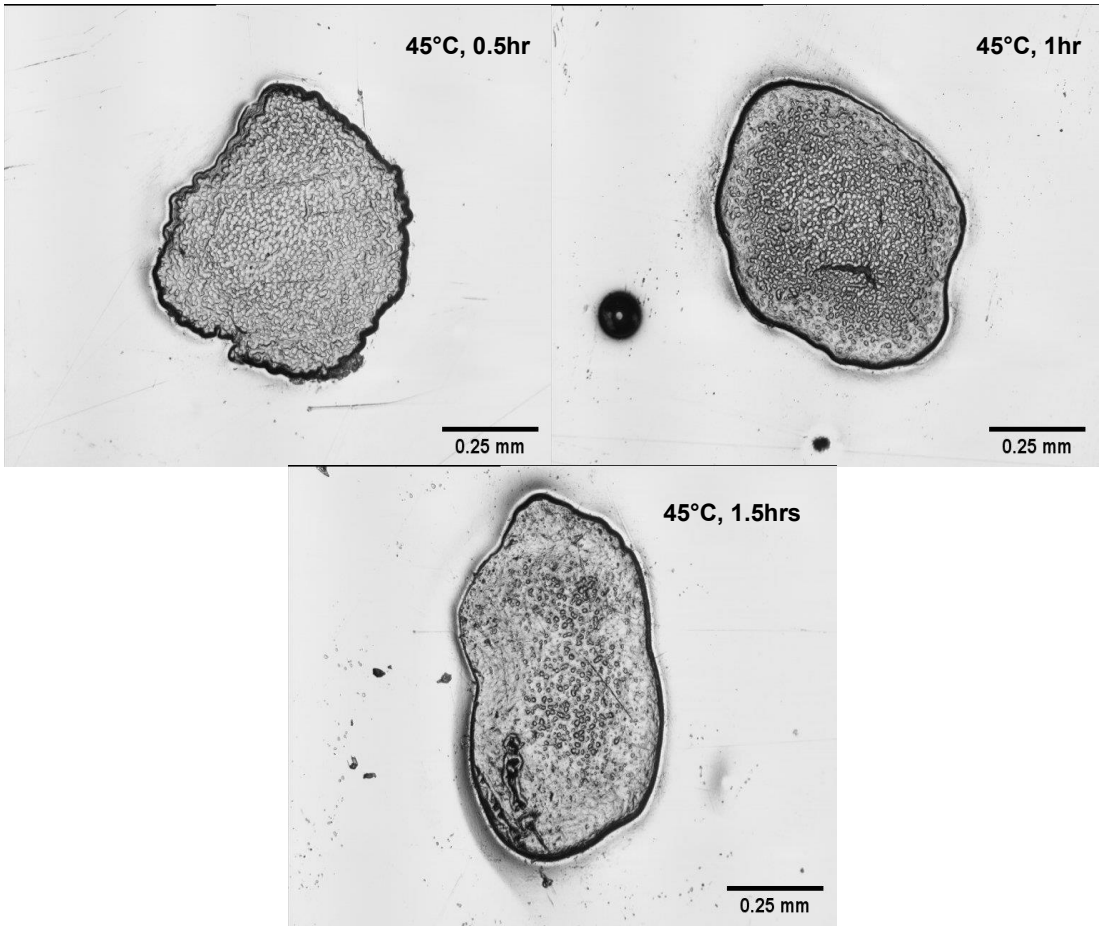

Figure 3.2: Microscopy cross-sectional images of Cordenka multifilament bundle at 45℃ for different times.

From these pictures one can conclude that this optical method is unsuitable to provide accurate information for the volume fraction of dissolved matrix, this is because the core matrix boundary could not be drawn in Image J to find

contrast between the original filaments and the matrix even at 45℃ for 1.5hrs. Therefore, it was not possible to calculate this percentage of dissolved material by this image. This is in contrast to previous work in this group [76, 103] on flax and cotton fibres which are comprised of a single fibre element and so dissolution can only proceed from the outside of the multifilament bundle and hence an optical technique can be used to follow the dissolution. For this multifilament bundle a new technique had to be developed to determine the activation energy of dissolution.

3.2.2 Wide Angle of X-ray Diffraction.

3.2.2.1 Two-dimension of X-ray Diffraction Pattern.

The results of a 2D X-ray image showing the positions and reflection peaks are shown in Figure 3.3, where the bright arcs (black lines) correspond to Bragg peaks. There were peaks with reflections $1\bar{1}0$, 110, 200 which are positioned at 12.4°, 20.2°, 21.8° of 2θ angles respectively for cellulose II. The peak reflection of 110 and 200 are combined. The faints peaks with reflections at location 14.8° and at 16.5° of 2θ angles are associated with cellulose I ($1\bar{1}0$, 110) Bragg plane respectively, which indicates that the Cordenka multifilament bundle are a mixture of predominantly cellulose II and surprisingly, a small amount of cellulose I. There is another reflection peak which appears in cellulose, which is due to the 012 planes, and can be seen in the 2D X-ray scattering at a circumferential angle of ~+/-60° (see also Figure 3.12) and a 2θ value of 20.3° as described by Nam et al[113] . As this 012-reflection plane has a very similar value of 2θ to the chosen equatorial position with maximum

signal intensity (20.3°), then this reflection will appear in a circumferential α scan (as shown schematically in Fig 3.12). We have proposed to include both these reflections in the determination of P_2 from a numerical integration between -90° and +90°. Our hypothesis is that following the change of any appropriate parameter with time and temperature, allows us to investigate time-temperature superposition and determine an activation energy for dissolution.

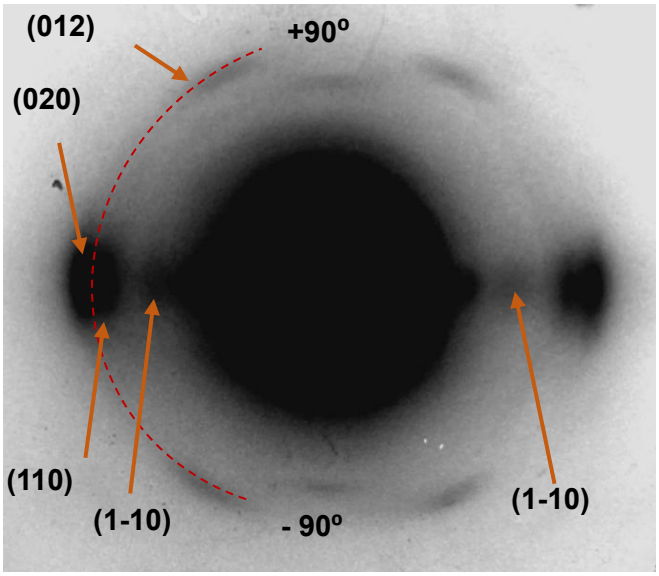

Figure 3.3 2D x-ray scattering pattern from unprocessed Cordenka multifilament bundle showing the α Circumferential scan setting in two dimensions (2D) from -90° to 90° (red dashed line) at 2θ = 20.3° and how this includes the 012 reflection.

3.2.2.2 2θ Scan of Cordenka Multifilament Bundle.

The 2θ scan was used to study the crystal structure of Cordenka multifilament bundle during the dissolution process. Results from a 2θ scan of the unprocessed Cordenka multifilament bundle is shown in Figure 3.4.

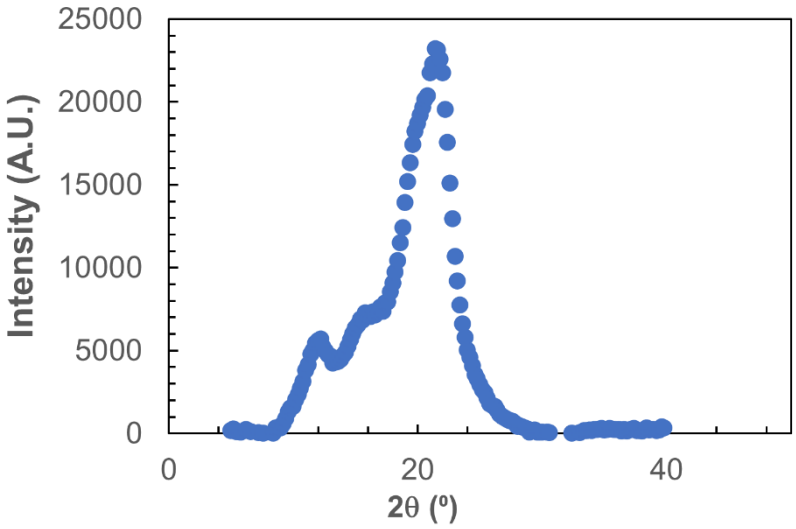

Figure 3.4: 2θ scan of unprocessed Cordenka multifilament bundle.

The deconvolution (curve fitting) method was applied to this data by using software (spreadsheet) taken from ref [114] to analyse the amount of cellulose I and cellulose II and amorphous fraction. An example of this fitting technique can be seen in Figer 3.5, which shows the data fitted by the combination of the peaks of cellulous 1 and 2 and amorphous. The original Bragg peak locations in 2θ scan were used as guide to identify cellulose I and cellulose II of unprocessed Cordenka multifilament bundle.

This fitting method was then tasked with fitting the raw data using a combination of amorphous, cellulose I and cellulose II peaks in superposition.

The results of deconvolution method with fitting data of unprocessed Cordenka multifilament bundle are shown in Figure 3.5.

Peaks of Cellulose I are shown in blue, orange and brown, while the cellulose II peaks were dark blue, green, and grey, all were allowed to move ± 2° either side of their expected positions as given in the literature [2, 115-118]. The amorphous peak is the red fitted peak was around 18° in 2θ scan [95, 119] and was fitted with a single peak to unprocessed Cordenka multifilament bundle data. It is of interest to see that there is still some remaining Cellulose I in these regenerated cellulose fibres, presumably from the original cellulose pulp source used to make the fibres.

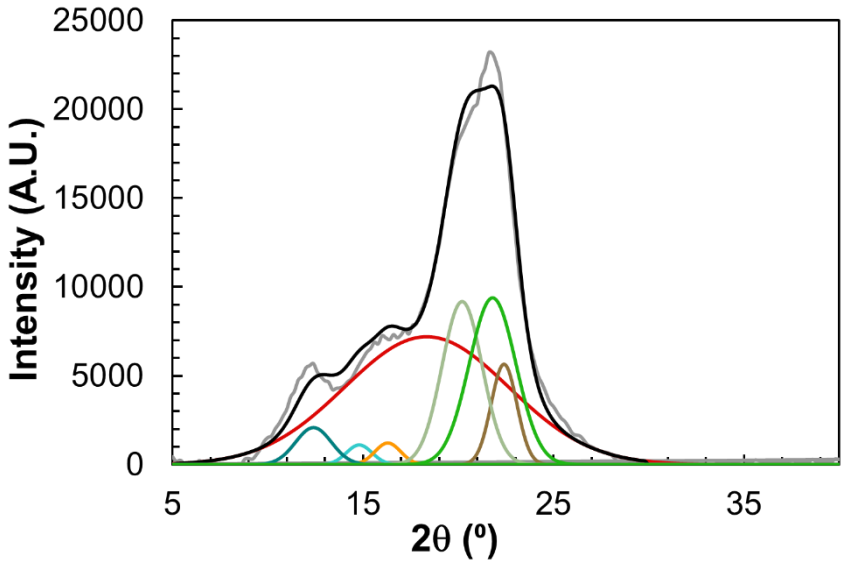

Figure 3.5: The fitting data of unpressed Cordenka multifilament bundle after combination of cellulose I, cellulose II and Amorphous.

Once the peaks were deconvoluted, the fraction of each component (cellulose I, cellulose II or amorphous) could be determined from the ratio of the sum of

the appropriate peaks to the total area. Also as described earlier, equation 2.2 could be used to determine the percentage crystallinity of the sample (sum of cellulose I and II peaks) to the total area under the peak (crystalline plus amorphous).

After deconvolution, the sum of the fitted crystalline peaks of cellulose to the total area of crystallinity and amorphous under the diffractogram calculated, through the deconvolution equation 2.2. The cellulose I and II relative peak widths and heights were determined from Table 3.1 with respect to110 peak. The widths of these peaks were broadened due to instrumental effects such as diffraction and air scattering. A least squares approach was used to determine the optimum fitting of the CI, amorphous and CII peaks. The area for each peak for different crystal forms was obtained via integration and the fraction of area summation, by using Gaussian distribution functions as explained in chapter 2. Resulting from measurement of 2θ° scan shows that unprocessed Cordenka multifilament bundle is a mixture of cellulose II (42%), cellulose I (10%) and amorphous (48%).

For clarification, Figure 3.6 shows the experimental peaks of cellulose I' and cellulose II individually. These peaks were found to exist at 14.8°, 16.7° and 22.7° for cellulose I and 12.4° , 20.2° and 21.8° for cellulose II in 2θ, as shown in Figure 3.6 (a, b). These angles correspond to Bragg reflections of the (110), $(1\bar{1}0)$ and (2,0,0) planes respectively [120, 121].

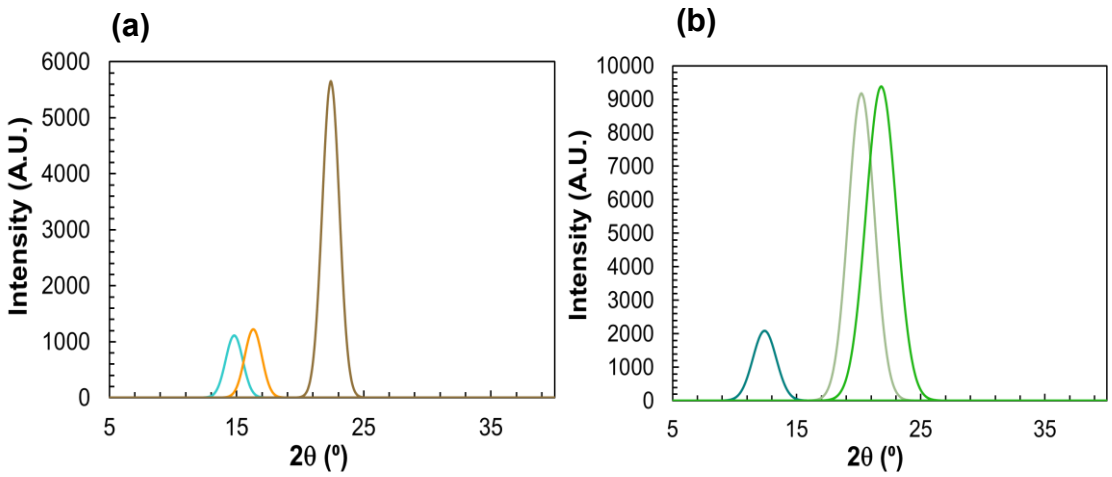

Figure 3.6: (a) is the experimental cellulose I peaks after isolated and (b) is the experimental cellulose II peaks after isolated using curve fitting method.

Table 3.1 presents the peak heights, peak positions and peak widths for pure cellulose I and cellulose II and amorphous, that was used for fitting data. The reflection peak (110) is set to a height of 1 and width of 1, and the other two peaks are normalised to them. Then when doing the least square minimising only four parameters need to be minimised, along with these values for the amorphous phase.

Peaks	**Cellulose I**			**Peaks**		**Cellulose II (Pure matrix)**		**Amorphous of CI and CII**
	High ratio	Width ratio	Positions		High ratio	Width ratio	Positions	Positions
110 (light blue)	1	1	14.8°	110 (dark blue)	1	1	12.4°	18°
$1\bar{1}0$ (orange)	1.1	0.8	16.7 °	$1\bar{1}0$ (green)	4.4	1.1	20.2°	-
200 (brown)	5.1	0.9	22.7°	200 (grey)	4.5	1.3	21.8°	-

Table 3-1: The values of highest peaks and position peaks of cellulose I and cellulose II.

Figure 3.7 shows (normalised) 2θ line scans for an unprocessed multifilament bundle, a partially processed multifilament bundle, and a fully dissolved sample. Experimentally, it was found that the 2θ line scan for the three materials (original filaments, processed multifilament, and completely dissolved film sample) did not change significantly enough between these three materials to accurately follow dissolution.

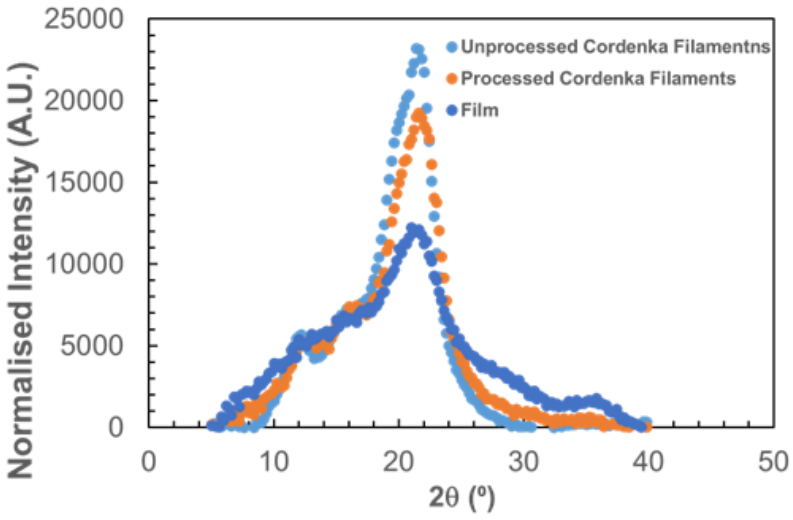

Figure 3.7: 2θ scan measurements of Cordenka multifilament bundle for three samples of original filaments, processed multifilament bundle and a completely dissolved multifilament bundle.

Therefore, a 2θ scan could not be used to follow change in crystal structure during the dissolution process (and hence determine the dissolution activation energy), as it has done before in previously published work in our research group on the dissolution of cotton multifilament bundle [103], which is predominantly cellulose I. The reason behind this is that the Cordenka

multifilament bundle have only a small amount of cellulose I and are predominantly cellulose II, which is a similar crystalline structure to the dissolved and coagulated matrix phase being a matrix of cellulose II and amorphous material. Therefore, an alternative method is proposed to calculate the volume fraction of dissolving regenerated cellulose filaments, which was to use the azimuthal α scan to follow the change of crystal orientation with time and temperature. This technique has worked successfully for silk fibres, as has been demonstrated in a previous publication from our research group [122].

3.2.2.3 Azimuthal α Scan of Cordenka Multifilament.

The X-ray technique for the azimuthal α scan allowed measuring the degree of molecular orientation in the various samples, where it carried out from -90° to 90° at a fixed angle 2θ of 20.3°. This 2θ angle was chosen based on the equatorial peak reflection (α=0°) (which is actually a combination of the 110 and 200 Bragg peaks). The result of the azimuthal α scan measurement found that Cordenka filament has two small peaks, as presented in Figure 3.8, associated with the 012 reflections as shown from the 2D photo. To investigate whether these peaks should be excluded, the two α scans were carried out for 2θ set at 18° and 23° separately, either side of the main peak at 2θ =20.3. It found that the height peak of a combination of the 110 and 200 Bragg peaks was too small with significant noise and the outer peaks with 012 reflections found real as described above in Fig 3.2, and as seen in Fig 3.12. Therefore, it was found that a value of 2θ = 20.3◦ is the best angle to get a strong signal.

These peaks with 012 reflections were also found in regenerated cellulose as mentioned in this ref [113].

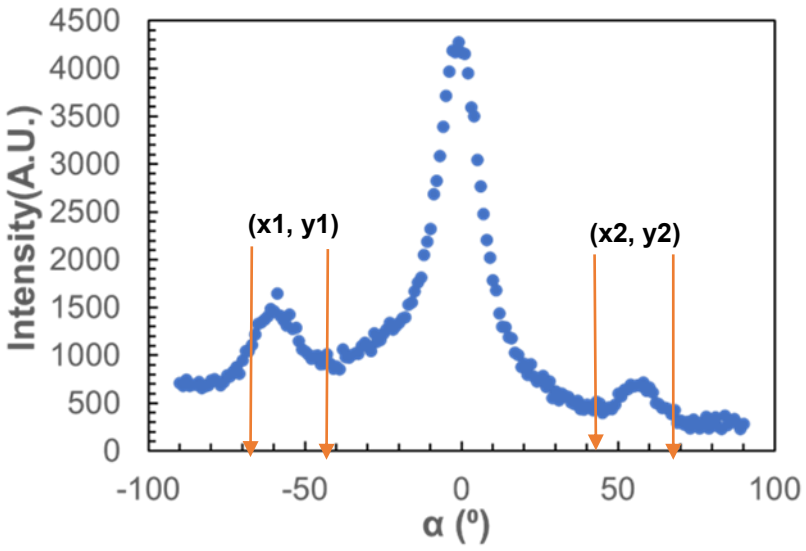

Figure 3.8: The azimuthal α scan with peaks at 012 position for unprocessed Cordenka multifilament bundle where x1and x2 indicated to the start and end points from x- x-axis (α°) and y1 and y2 indicated to the start and end points from y-axis (intensity) .

To explore the effect of including (or not these outer 012 peaks) a theoretical method was applied for further investigation, where first the data of the α scan was integrated with the outer peaks included, by using Herman's equation 2.4 to determine P_2 value. After that, a linear equation was used to remove outer peaks and then to recalculate the P_2 value and investigate whether it influenced the overall prediction of the dissolved fraction.

Mathematically, from the data of α° scan of x-axis took start point x_1 and end point x_2, while intensity values used in y-axis took y_1 and y_2 as start and end

points of outer peaks, as shown in Figure 3.8. By calculating the average values of start and end points of outer peaks, the slope, M found by $= \frac{\Delta y}{\Delta x}$ and constant c, obtained from the linear equation by $c = (y - M) * x$. The linear equation applied on α° data (original) of outer peaks 012 by $y = Mx + c$ to obtain α data without outer peaks. The result α° scan without 012 peaks shown in Figure 3.9. Herman's values P_2 of unprocessed filament found for without 012 peak is 0.62 and with 012 peak is 0.57, which indicated an insignificant difference than between these two different analysis regimes. We therefore considered the P_2 value with the 012 peaks included as more reflective of the crystal orientation of the unprocessed individual Cordenka multifilament bundle and this will be discussed further in Chapter 5 in comparison with the Lyocell multifilament bundle.

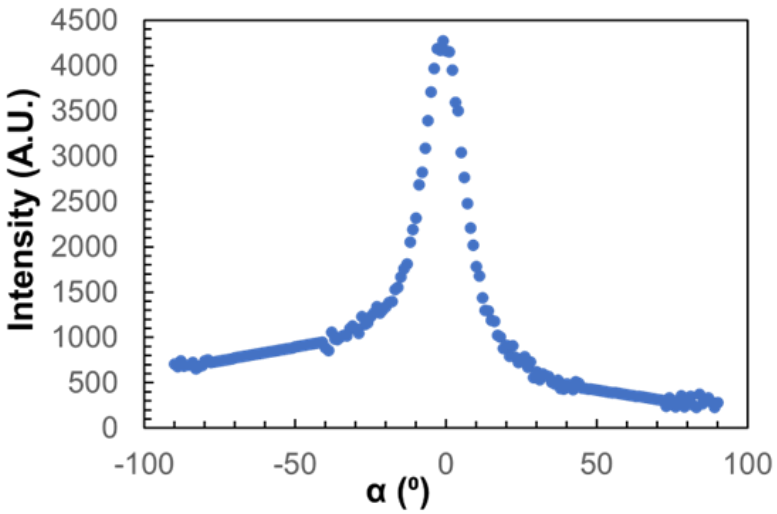

Figure 3.9: The azimuthal α scan without peaks at 012 position for unprocessed Cordenka multifilament bundle.

To evaluate the effect of either including (or not) the outer 012 reflections, the volume fraction, v_m of composite fibre with 012 peaks and without 012 peaks are calculated by applying equation 2.7 using the measured P_2 values and assuming a rule of mixture. It was found that the dissolved volume fraction of the partially dissolved composite fibre increased with time and temperature as shown in Figure 3.10 and Table 3.2 but was very similar for the two methods (with or without the outer 012 reflections) even though the P_2 of the original filaments is different.

Temperatures	Time	v_m % with 012	v_m % without 012
0	0	0	0
30	1	18.2	22.5
30	2	18.2	22.5
30	3	24.2	30
30	5	27.3	32.5
35	0.5	18.2	22.5
35	1	21.2	25
35	2	27.3	32.5
35	3	36.4	40
35	5	42.4	52.5
40	1	30.3	35
40	2	45.5	50
40	3	66.7	70
45	0.5	33.3	40
45	1	60.6	65
45	1.5	72.7	77.5

Table 3-2: The percentage difference of volume fraction v_m with and without 012 peaks.

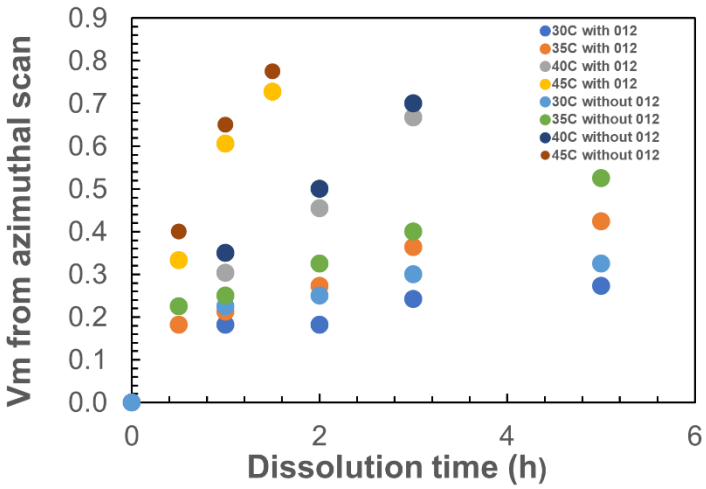

Figure 3.10: The volume fraction of composite fibre calculated by either including or excluded the outer 012 peak.

Figure 3.11 shown the comparison between the calculated volume fractions from P_2 including the 012 reflections (e.g Figure 3.8) and without the 012 peaks (e.g., Figure 3.9). This confirms our hypothesis that we can use the data with and without 012 peaks to measure the dissolution rate with time and temperature.

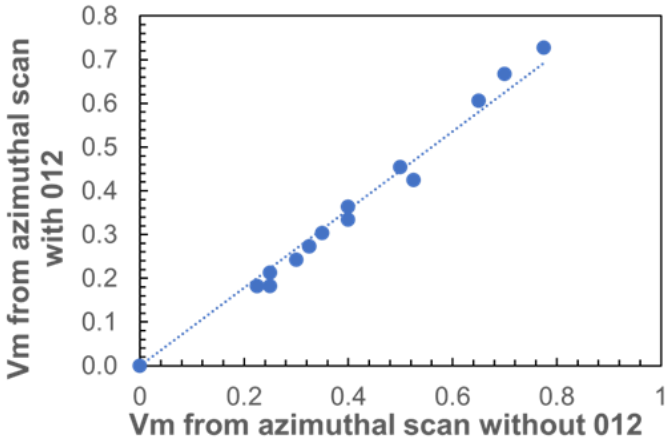

Figure 3.11: The relation between the volume fraction with 012 and without 012 crystallinity peaks.

The data with 012 peaks was therefore used throughout to calculate the volume fraction of the dissolved fraction. Figure 3.12 shows a comparison between a typical α scan for unprocessed multifilament bundle, a partially dissolved composite multifilament bundle and a fully dissolved film. In contrast to the 2θ scans, there is a measurable change and so P_2 can therefore be used to follow dissolution with time and temperature. As the oriented crystals (associated with the unprocessed multifilament bundle) dissolved they reformed as random crystals, leading to an increase of the background level and a reduction in the central oriented crystal peak. For a completely dissolved and coagulated film sample, which is considered to be similar to the matrix phase within the composite Cordenka multifilament bundle, a constant intensity was seen at all angles indicating random orientation of the crystal structure as expected.

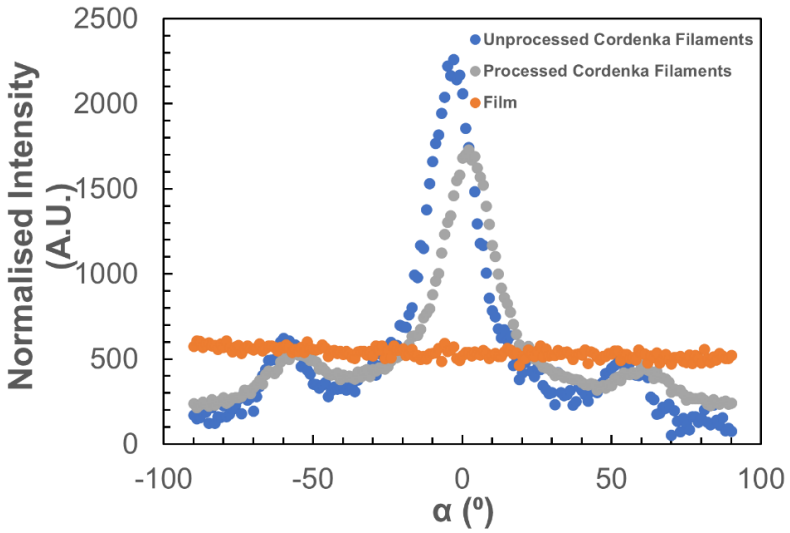

Figure 3.12: The azimuthal α scan to measure the change in orientation.

The overall average of P_2 for all the processed composite multifilament bundle, from processing at different times and temperatures, was calculated by using

equation 2.4. The results of the change in the average value of P_2 with temperature and time are shown Figure 3.13. The reduction in the average P_2 value for processed a composite multifilament bundle is due to the increase in the random molecular orientation component due to the dissolved and coagulated matrix fraction. From Figure 3.13, It can be seen that the P_2 of the processed composite multifilament bundle reduces with increasing time and temperature. The reduction of the average value of P_2 of the processed composite multifilament bundle (from three measurements on different composite multifilament bundle) at various times and temperatures appears broadly linear, although with an increasing slope as the processing temperature increases. This indicates increased effectiveness of $[C_2mim]^+$ $[OAc]^-$ to dissolve the Cordenka multifilament bundle with increasing time and temperature.

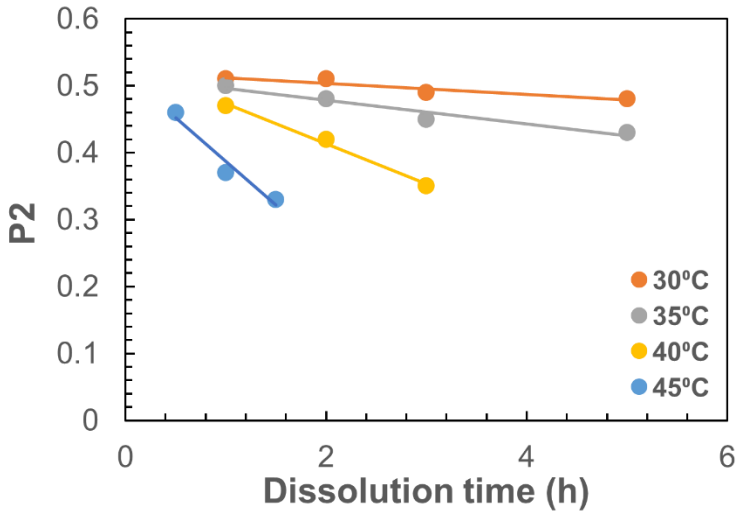

Figure 3.13: The Correlation between the average calculated P_2 and different dissolution times and temperatures for processed Cordenka multifilament bundle. error bars within the data points.

The P_2 data can be formed into a master curve using time-temperature superposition. This method was previously reported in the study of the dissolution of cotton and silk fibres in [C2mim] [OAc] by our research group [76, 103, 122]. Based on this previous work the data of P_2 values are first plotted as function of the logarithm of time and the different temperature curves are then superposed in (ln time) using equation 3.1 at a chosen reference temperature.

$$t_R = t_1 a_T$$

$$\ln t_R = \ln t_1 + \ln a_T \tag{3.1}$$

where T_1 is the temperature, T_R is the reference temperature, t_1 is the time value before scaling, t_R is the time value after scaling/shifting and $ln\ a_T$ is the shift factor [122]. Figure 3.14a explains the steps used to find the best shift factors so that all the points overlap on one master curve. Firstly, the orange line at a processing temperature of 35℃ was chosen as the reference temperature (T_R) on the ln time axis (Figure 3.14 a). Then all the other temperature curves were shifted horizontally by an initial shift factor (ln a_T) to the data of the 35℃ curve along the ln time of X axis. Next, a polynomial function was applied as a guide around this preliminary shifted data. Then the individual shift factors were changed to get the best fit between the polynomial function and the shifted points by maximizing the value of R^2, which is equal to 0.98 The final master curve between the average P_2 and the shifted data at a reference temperature of 35℃, is shown in Figure 3.14 b in log time and in linear time in Figure 3.14c.

From the relationship between the shifted average P_2 values (at a reference temperature of 35℃) with linear dissolution time, as shown in Figure 3.14 c, it can be estimated that complete dissolution of the Cordenka multifilament bundle would be achieved after 14h dissolution time at 35℃, as the P_2 value of completely dissolved filaments extrapolates to 0.25. Table 3.3 shows the complete dissolution of the Cordenka multifilament bundle at 30℃, at 40℃ and at 45℃.

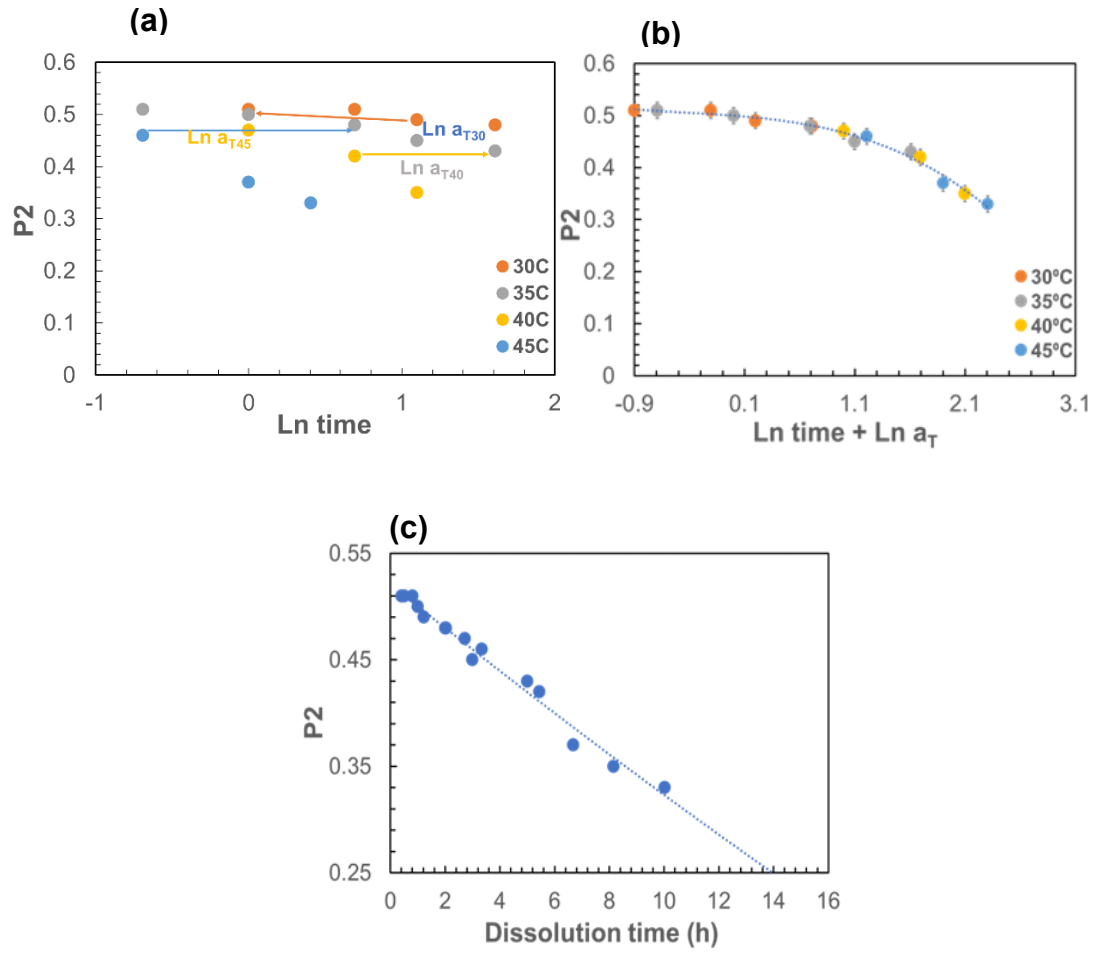

Figure 3.14: a) logarithm of time (ln aT) with P_2, all data of time and temperature shifted at reference 35℃. b) the master curve of relation between P_2 and shifting time at various temperatures of Cordenka multifilament bundle. c) the resultant master curve between P_2 and dissolution time.

Reference temperature ℃	Complete dissolution of Cordenka/hrs
30	32
35	14.5
40	5
45	2

Table 3-3: the complete dissolution of the Cordenka multifilament bundle at 30℃, at 40℃ and at 45℃.

Figure 3.15 shows that plotting the ln of the shift factors versus the inverse temperature gives a linear relationship, indicating that the dissolution of the Cordenka multifilament bundle follows an Arrhenius behaviour. We can therefore use equation 3.2 to calculate an activation energy for this dissolution through the Arrhenius equation as follows:

$$\ln a_T = \ln A - \frac{E_a}{RT} \tag{3.2}$$

where a_T is the simple multiplicative factor, A is the pre-exponential factor, E_a is the activation energy, R is the universal gas constant and T is temperature (K) [123, 124]. Figure 3.15 shows the best fit line to this data (using the LINEST function in Excel) resulting in an activation energy value of 151 ± 3 kJ/mol.

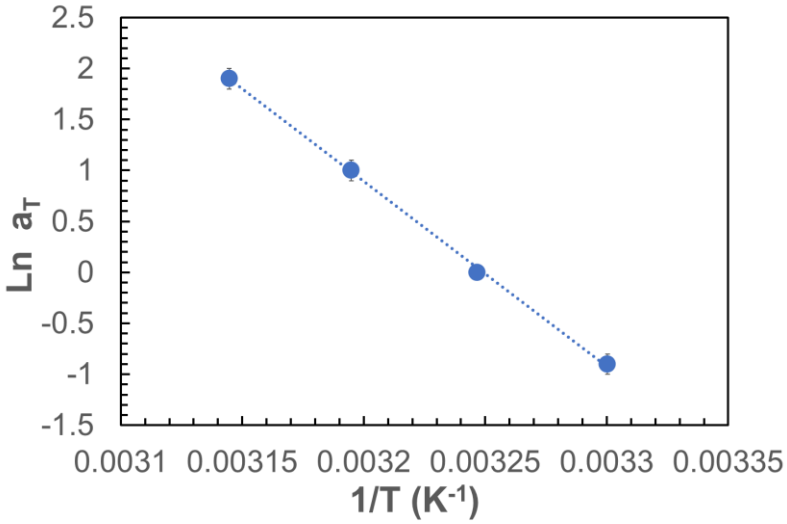

Fig 3.15: $ln\, a_T$ plotted against the inverse of temperature, dotted line is Arrhenius equation.

The time temperature superposition method was separately applied also using 30℃, 40℃ and 45℃ as reference temperatures to calculate the activation energy, the P_2 data was shifted at each of these temperatures, to get a master curve as it has been done at 35℃. Figure 3.16 shows the final master curve of data at 30℃. The same master curve at 40℃ and 45℃, is shown in Figures 3.16 b and c.

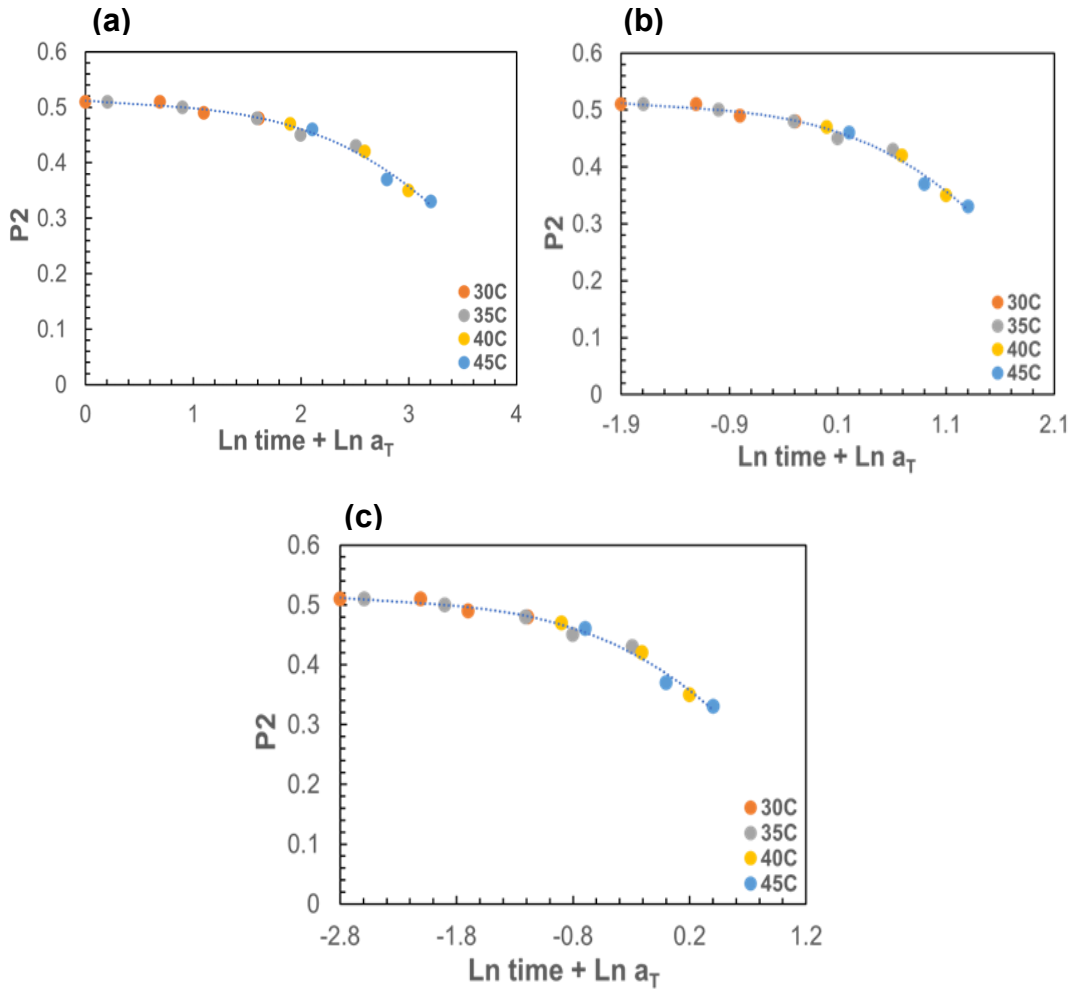

Figure 3.16: (a) is the final master curve of data at 30°C, (b) the final master curve of data at 40℃ and (c) the final master curve of data at 45℃

3.2.2.3.1 Shift Factor, Intercept Arrhenius dependence.

The “intercept method” is based on the relationship between the shift factors and inverse temperature through the Arrhenius equation 3.2, which was used earlier to calculate the dissolution activation energy. All data was shifted to 30℃ to create a master curve at this temperature, then the whole process repeated again for 35℃, 40℃ and 45℃. The shift factors were plotted as a function of inverse temperature to give an activation energy and intercept, as for 35℃, see Figure 3.16. The intercept values from these Arrhenius plots were

itself then plotted against the inverse reference temperature, see Figure 3.17, where it can be seen that the intercepts themselves follow an Arrhenius type behaviour. Starting with the Arrhenius equation (equation 3.2) and setting a_T as $a_{T_{ref}}$, gives equations 3.3-3.5.

$$T = T_{ref} \tag{3.3}$$

$$\ln a_{T_{ref}} = \ln A - \frac{E_a}{RT_{ref}} \tag{3.4}$$

The shift factor at the reference temperature must equal one, hence $\ln(a_{T_{ref}})$= 0, since no shifting is needed for the data already at the reference temperature, therefore

$$ln\ \mathrm{A}_0 = \frac{E_a}{RT_{ref}} \tag{3.5}$$

The important result is that intercept $\ln \mathrm{A}_0$ in each of these graphs is itself temperature dependent $\ln \mathrm{A}_{30}$, $\ln \mathrm{A}_{40}$, $\ln \mathrm{A}_{45}$ and $\ln \mathrm{A}_{35}$ are 59.75, 57.85, 56.95 and 58.85 for temperatures 30℃ Figure 3.17(a), ,40℃ Figure 3.17 (b), 45℃ and Figure 3.17 (c), respectively and 35℃ Figure 3.16.

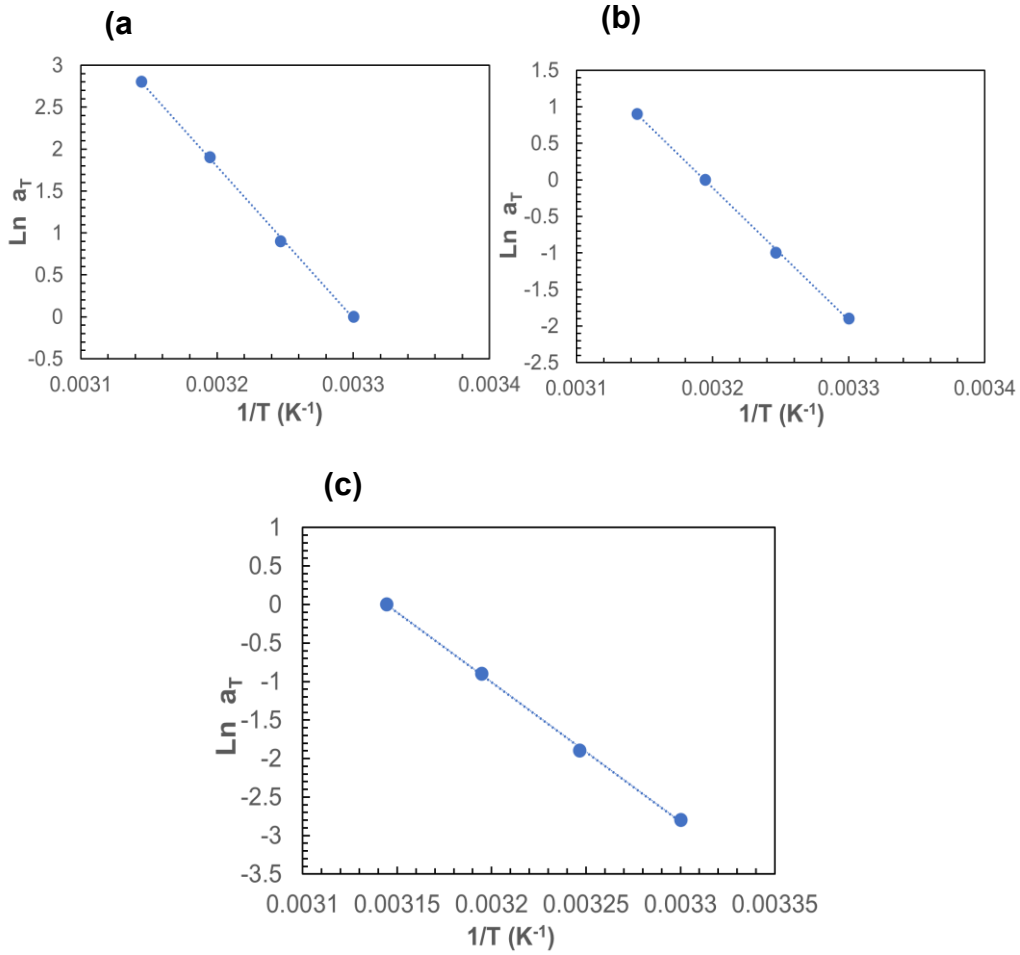

Figure 3.17: (a) $ln\, a_T$ plotted against the inverse of temperature at 30℃ as reference temperature, (b) $ln\, a_T$ plotted against the inverse of temperature at 40℃ as

The correlation between $ln\ \mathrm{A}_0$ and $^1/_{T_{ref}}$ gives the gradient $\frac{E_a}{R}$ to give a further way to calculate E_a, as shown in Figure 3.18. This plotted graph gave a similar E_a as previously calculated for the four different temperatures (at 30℃, 35℃, 40℃ and 45℃) equal to $151\ \pm 3$ kJ/mol. This is approximately the same value of activation energy was calculated from time-temperature superposition method. It has been found that the “intercept method” is very sensitive to any non-Arrhenius dependence and is a useful validation of the approach taken in this work.

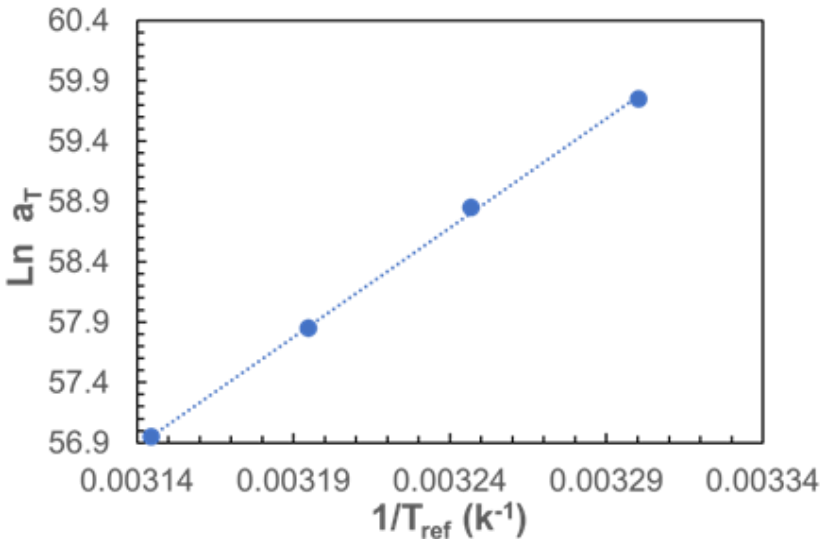

Figure 3.18: $ln\, a_T$ plotted against the inverse of reference temperature at 30℃, 35℃,40℃ and 45℃.

3.2.3 Dissolved and Coagulated Matrix Fraction v_m from the Wide Angle of X-ray Diffraction.

By applying a rule of mixtures to the experimental data of P_2, from the azimuthal α scan measurements, the volume fraction v_m of the dissolving fraction of the original composite multifilament bundle could then be calculated. This dissolved and coagulated fraction (v_m) now indicates the amount of 'matrix' phase resulting in the processed composite multifilament bundle combined with the original undissolved multifilament. This procedure was done by calculating the points between the orientation of the unprocessed Cordenka multifilament bundle with (v_m) = 0% dissolved and the completely dissolved matrix with (v_m) = 100%, by assuming a linear mixing rule.

$$v_m = \frac{P_{2c} - P_{2f}}{P_{2m} - P_{2f}} \quad (3.6)$$

Assuming $v_m + v_f = 1$. Here P_{2c} indicates the P_2 value of the processed composite multifilament bundle, P_{2f} is the P_2 value of the original unprocessed multifilament bundle (measured as = 0.57) and P_{2m} is the P_2 value of the completely dissolved matrix film with 0.25 (randomly oriented crystals). Figure 3.19 presented the relationship between the calculated v_m value and the dissolution time and temperature. The volume fraction of dissolved Cordenka multifilament bundle increases with increasing time and temperature.

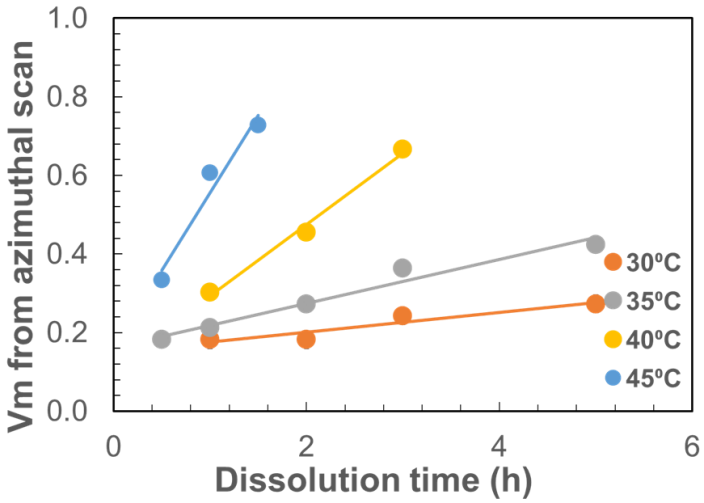

Fig 3.19 The relationship between V_m and dissolution time.

3.2.4 Mechanical Measurements.

The fall in the mechanical Young's modulus and strength have played an important role in our analysis, as following these two properties provides two further independent methods to follow dissolution and determine the activation energy. As with the measurement of the average crystalline orientation of the partially dissolved composite multifilament, we are assuming that these two measures of the properties of the partially dissolved multifilament bundle are some combination of the unprocessed multifilament bundle and the dissolved matrix fraction.

The tensile modulus of a composite is dependent on the ratio between the original fibres and the dissolved matrix. Similarly, the Young's modulus of the composite samples can provide information on how much unprocessed multifilament bundle (raw material) has been converted into processed Cordenka multifilament bundle (coagulated cellulose). The mechanical strength provides the amount of multifilament bundle core by giving a variety of the strengths, which indicates to the amount of dissolved fraction in the sample.

3.2.4.1 Young's Modulus.

The initial linear stress-strain region indicates an elastic region as shown in Figure 3.20 (green line). The slope of this initial stress and strain gives a Young's modulus E, which calculated from equation 2.10.

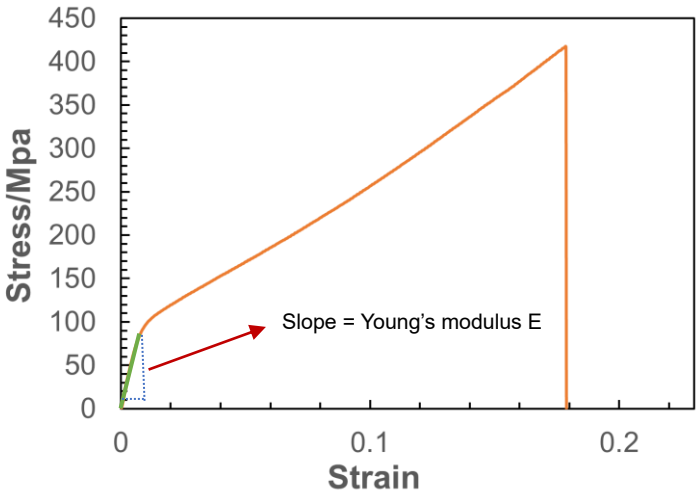

Figure 3.20: Typical stress-strain curve of one viscose rayon samples processed at $35℃$ for 1hr.

The measured Young's modulus of the partially dissolved composite multifilament bundle as a function of time at various temperatures is shown in Figure 3.21 a. It can be seen that the pattern of the decrease of the measured Young's modulus values, with time and temperature, is very similar to that shown on Figure 3.13 for the measured average P_2 values, as both are a measure of the remaining fraction of the unprocessed multifilament bundle. The data of the measured Young's modulus is shifted with time and temperature, using the temperature of $35℃$ as the reference temperature using the same procedure as explained above. Figure 3.21 b shows the result of the final master curve after shifting the data, plotted against Ln (time).

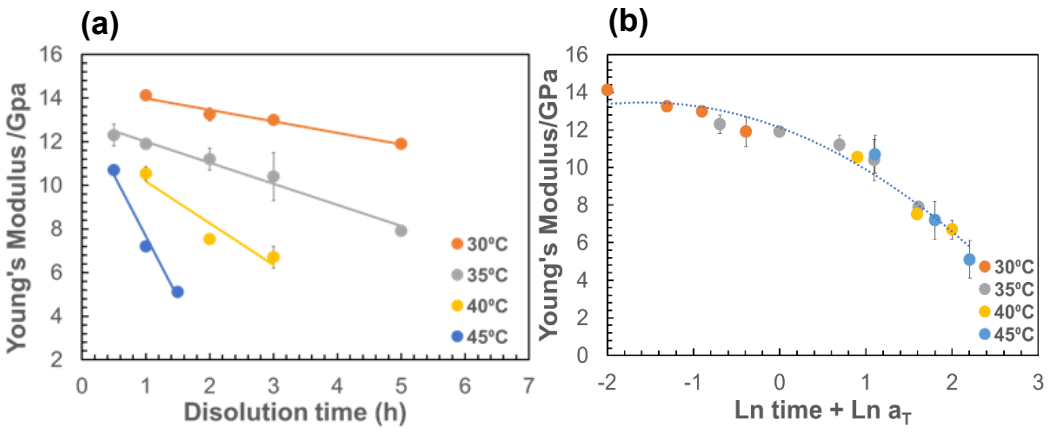

Figure 3.21: a) The measurements of Young's modulus at various temperature and time. b) the master curve between Young's modulus and dissolution time.

The relationship between the shifting factors and the inverse temperature was again used to calculate an activation energy (as they showed a linear dependence) using the Arrhenius equation 3.2, see Figure 3.22. This gave an activation energy value of 198 ± 29 kJ/mol.

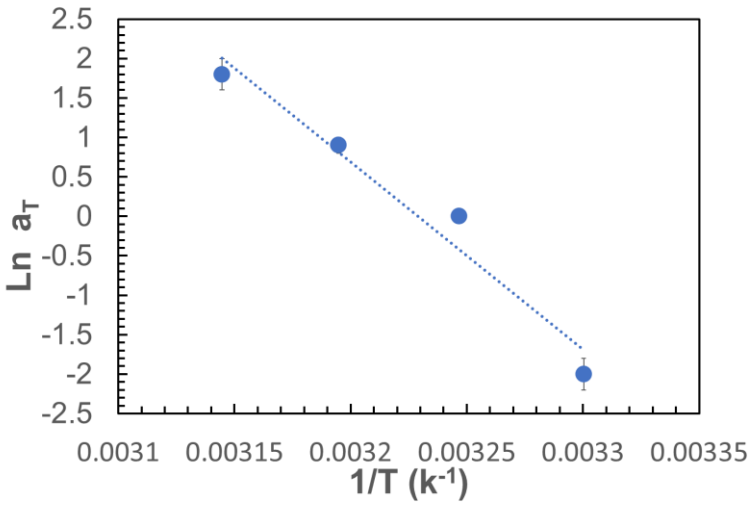

Figure 3.22: Activation energy determined from TTS.

The time temperature superposition method was separately applied on 30℃, 40℃ and 45℃ as reference temperatures to calculate activation energy, the Young's modulus data was shifting at each of these temperatures, to get master curves. As it has been done at 35℃. Figure 3.23 shows the final master curve of data at 30℃. The same master curve was obtained at 40℃ and 45℃, as shown in Figure 3.23 b and c.

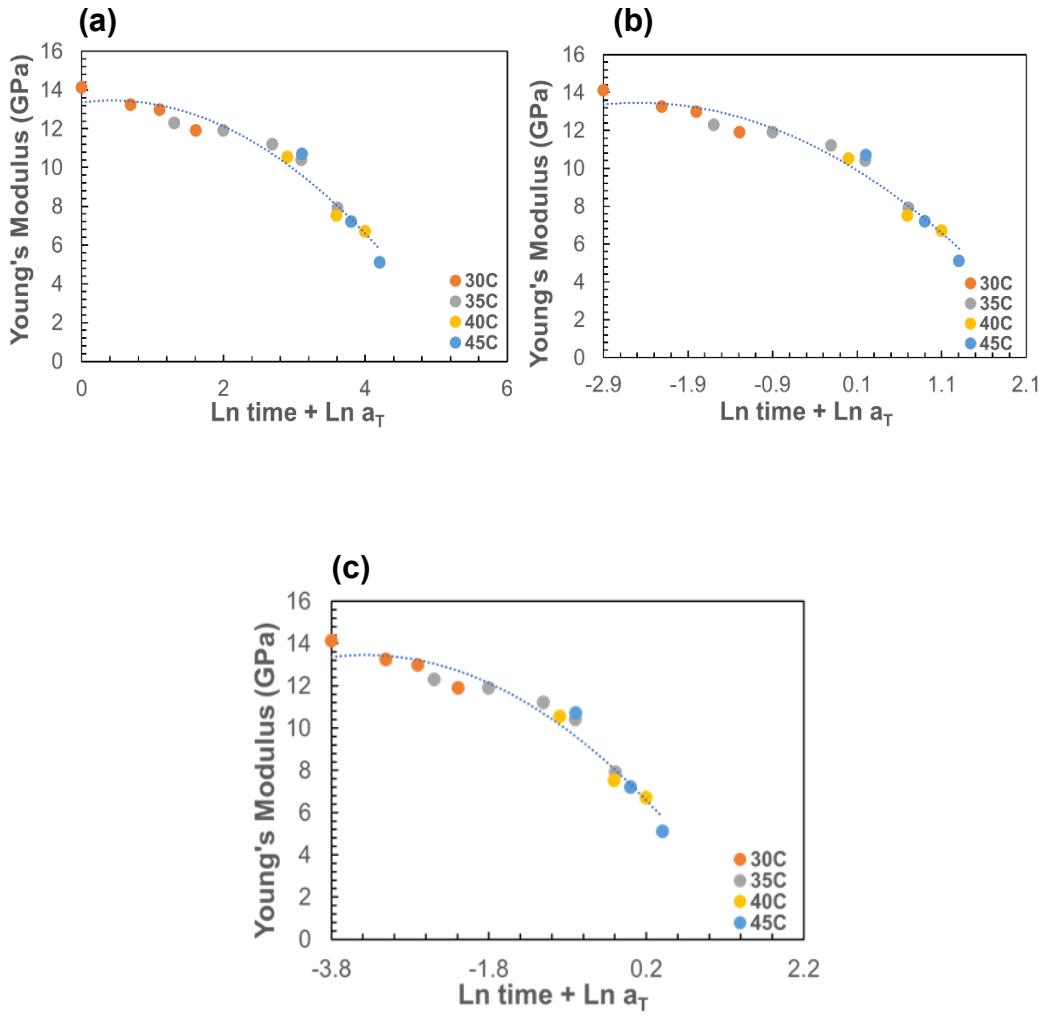

Figure 3.23: (a) The final master curve of data at 30℃ as reference temperature (b) the final master curve of data at 40℃ as reference temperature and (c) the final master curve of data at 45℃ as reference temperature.

The Arrhenius equation was plotted between $ln\, a_T$ of the shift factors of individual temperature (30℃, 40℃ and 45℃) and an inverse of temperature, as shown in Figure 3.24 (a-c). This indicates that the dissolution of the Cordenka multifilament bundle follows Arrhenius behaviour. This relation was used to calculate the activation energy, E_a for Cordenka multifilament bundle at 30℃, 40℃ and 45℃ separately E_a from these three different temperatures and was found to have the same value of 198 ± 29 kJ/mol. The same value

of E_a has been found using 35℃ as the reference temperature. The average value of E_a from the four different temperatures (at 30℃, 35℃, 40℃ and 45℃) is equal to 198 ± 29 kJ/mol.

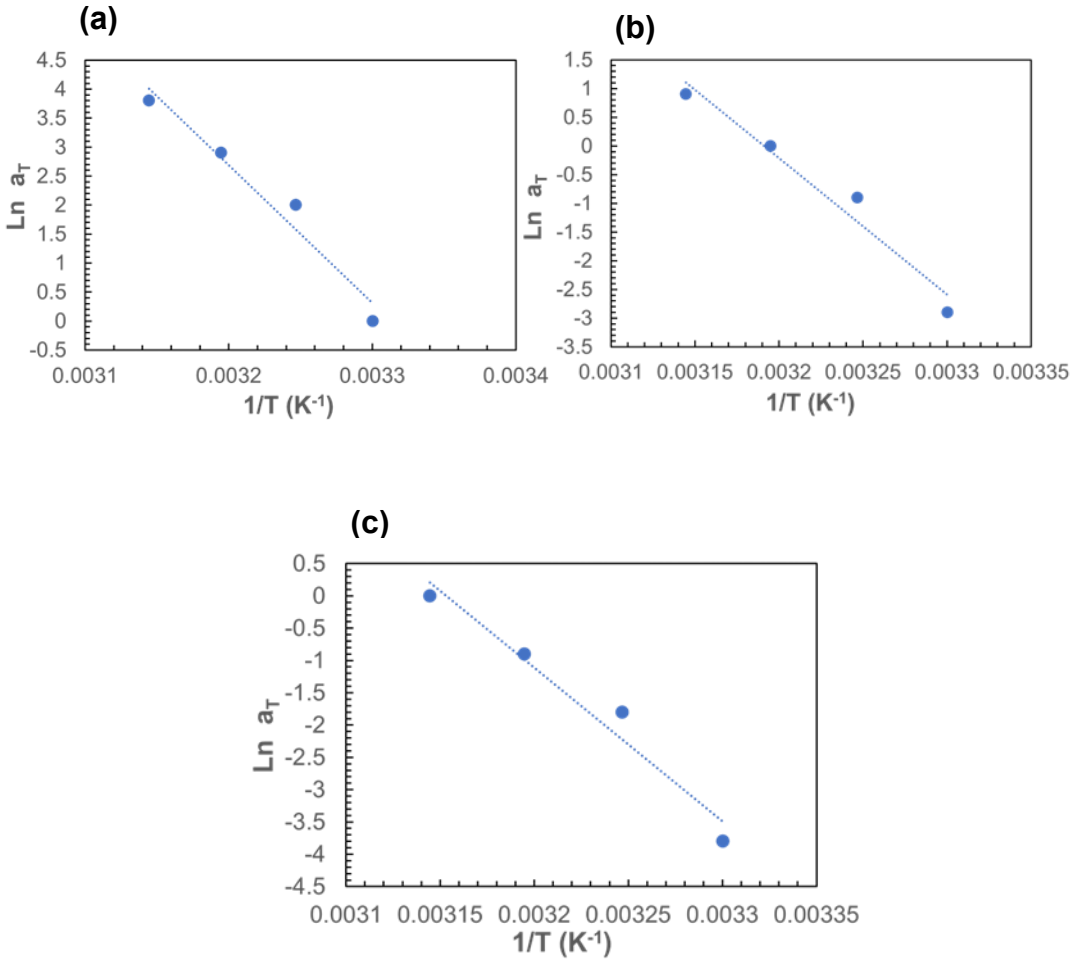

Figure 3.24: (a) $ln\, a_T$ plotted against the inverse of temperature at 30℃ as reference temperature, (b) $ln\, a_T$ plotted against the inverse of temperature at 40℃ as reference temperature and (c)) $ln\, a_T$ plotted against the inverse of temperature at 45℃ as reference temperature.

The relation between the Young's modulus with linear dissolution time in the Ionic liquid [C_2mim] [OAc], is presented in Figure 3.25. At short times, the Young's modulus is seen to first fall rapidly, and then, the Young's modulus decreases at a slower, but linear, rate with time. We propose that this is because at early dissolution times, when the individual Cordenka multifilament bundle is not connected (being untwisted). As explained the ionic liquid can penetrate easily between each individual multifilament bundle, resulting that the surrounding outer layer of each multifilament bundle can be dissolved to form the matrix. Once the inner space between the individual multifilament bundle is filled with a dissolved cellulose/[C_2mim] [OAc] gel, this forms a barrier to the ionic liquid and therefore dissolution proceeds more slowly by dissolving the multifilament bundle on the outside of the fibre bundles and so proceeds at a lower rate. The same result described in the optical microscopy result section, which emphasises the behaviour of the dissolution of Cordenka multifilament bundle during an increase of time and temperature.

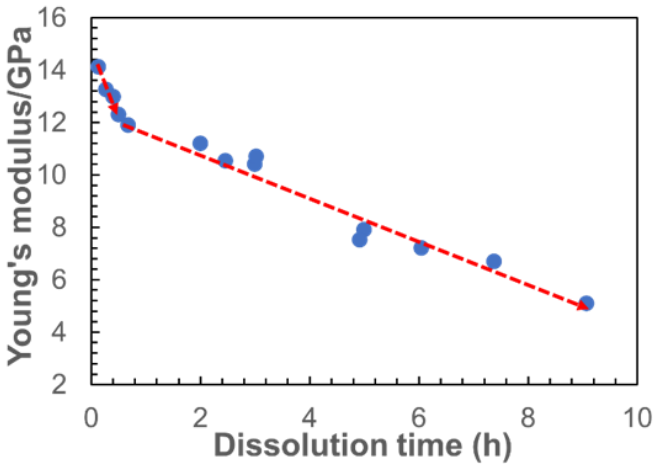

Figure 3.25: Master curve between Young's modulus and dissolution time using 35℃.

To obtain a value of the modulus of the unprocessed" Cordenka multifilament bundle the data for the early times (the first four points shown in more detail in Figure 3.26 is used to extrapolate the modulus to zero time. This a better method, as measuring the modulus of a bundle of untwisted, and so unbonded, multifilaments was found to give erroneously low values of Young's Modulus as the fibres are not connected together and the bundles are untwisted. From the correlation between the Young's modulus data and the linear dissolution time at 30℃, and using a second order polynomial function, the best fit gave a value of 14.8 GPa for the original multifilament bundle, as shown in Figure 3.26.

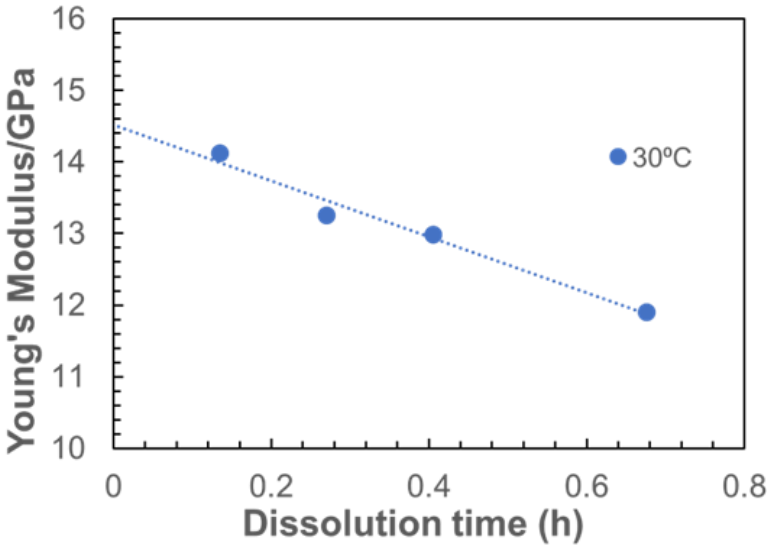

Fig 3.26: The extrapolate method to determine the modulus for unprocessed Cordenka multifilament bundle from real master curve at 30℃.

Experimentally, the azimuthal α scan technique has been used to calculate the volume fraction of composite filaments of the partially dissolved Cordenka multifilament bundle. The measured Young's modulus data could then be plotted against these calculated volume fraction values from the azimuthal α scan measurements to evaluate the possibility of applying rule of mixtures (Voigt or Reuss models equations 2.15 and 2.16) to our processed composite multifilament bundle and to specify the effect of changing the volume fraction on the behaviour of the Young's modulus results.

The result of plotting the measured Young's modulus and the calculated volume fraction (from the α scan) with the two mixing rules is shown in Figure 3.27. Based on the extrapolated fibre value of E_f =14.8 GPa with using $V_m =$ 0% dissolved and the completely dissolved matrix $V_m =$ 100%, with value of

E_m =1.5 GPa (from measuring the dissolved and coagulated completely dissolved film, calculated using equation 2.17), the upper-bound and lower-bounds are calculated by following equations (2.15, 2.16) respectively. The data points of Young's modulus versus V_m have shown a tendency to follow the upper- bound (Voigt series), confirming excellent adhesion between the original fibres and the dissolved and coagulated matrix fraction. This is an important finding for future work on all cellulose composites made from regenerated cellulose fibres.

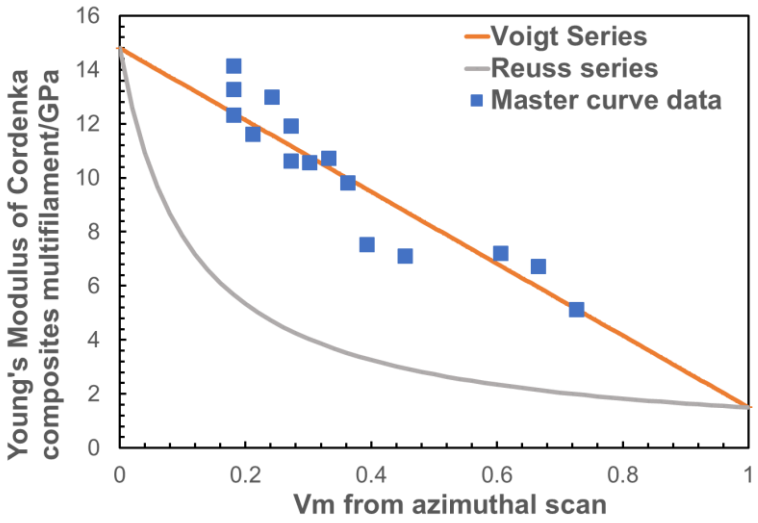

Fig 3.27: Relation between volume fraction V_m and young modulus from α scan with prediction of rule of mixtures, Voigt and Reuss series.

3.2.4.2 Strength Measurement.

The correlation between the variation of the ultimate composite breaking tensile strength σ_{UTS} with dissolution time at various temperatures is shown in Figure 3.28a. The decrease of the strength values with an increase of time and temperature indicates the dissolution of Cordenka multifilament bundle. The

same result has been previously seen from measuring P_2 and Young's modulus at 30℃, 35℃ and 40℃ and 45℃ for 30 min,1, 1.30, 2,3 and 5 hours as shown in Figure 3.13 and 3.21 a.

The measured data of the strength values are shifted with time and temperature, using the temperature of 35℃ as the reference temperature using the same procedure as explained above. Figure 3.28 b, shows the result of the final master curve after shifting the data, plotted against Ln (time).

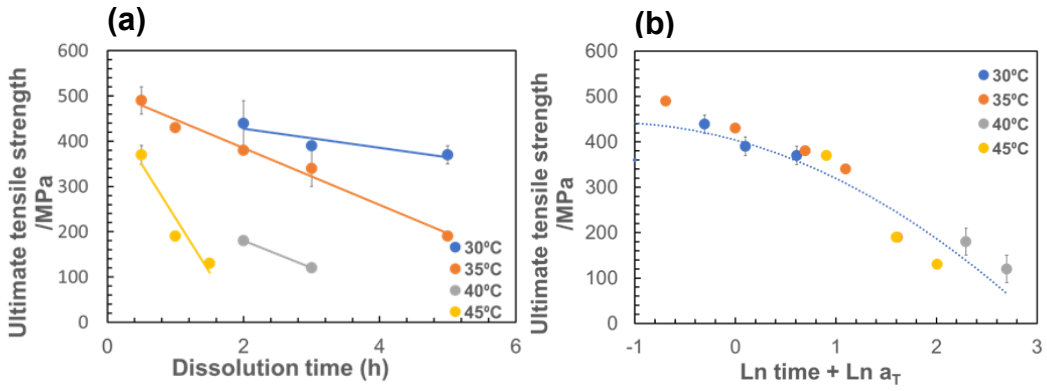

Figure 3.28: a) The measurements of tensile strength σ_{UTS}, at various temperature and time. b) the master curve between σ and dissolution time.

The dissolution rate slows when all the interior spaces in the Cordenka multifilament bundle are filled, resulting that the strength values also falls, as in Figure 3.29. The value of the strength of the unprocessed" Cordenka multifilament bundle was extrapolated to Zero time by utilising the correlation between the strength data and the linear dissolution time. The data for all times and temperatures of 30℃, 35℃, 40℃ and 45℃ used by applying a second order polynomial function. The best fitting gave a strength value for an

unprocessed multifilament bundle of 497 MPa. This extrapolation value of strength was taken for all times and temperatures.

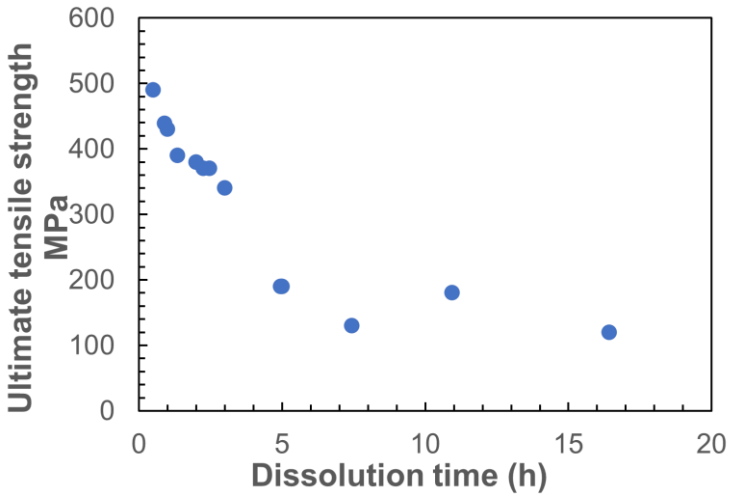

Figure 3.29:The Master curve between strength and dissolution time using TTs at 35℃ as reference temperature.

This method was used as a further way of measuring the activation energy using time temperature superposition. The relationship between the shifting factors and the inverse temperature was again used (as they showed a linear dependence) using the Arrhenius equation 3.2 as shown in Figure 3.30. This gave an activation energy value of 158 ± 40 kJ/mol.

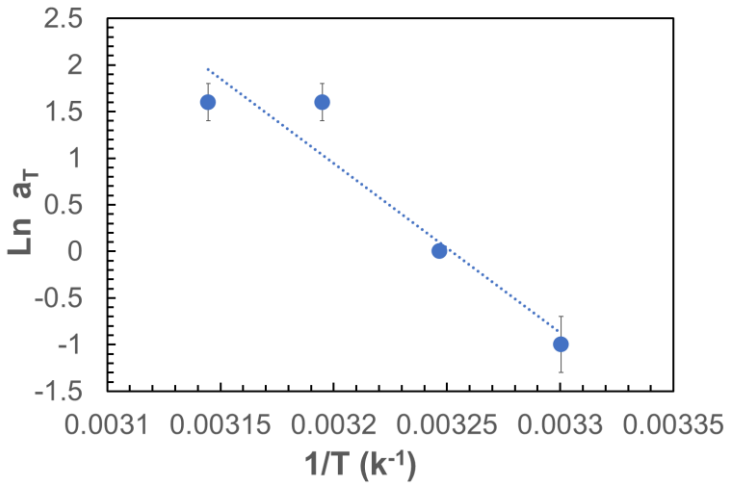

Figure 3.30: $ln\, a_T$ plotted against the inverse of temperature at 35℃ as reference temperature.

The measured strength data could then be plotted with these calculated volume fraction values from the azimuthal α scan measurements to evaluate the possibility of applying the rule of mixtures to our processed composite filaments and to specify the effect of changing the volume fraction on the behaviour of the strength results.

The result of plotting the measured strength and the calculated volume fraction (from the α scan) with the two mixing rules is shown in Figure 3.32. Based on the extrapolated Cordenka multifilament bundle value of σ_f = 483 MPa with using $V_m = 0\%$ dissolved and the completely dissolved matrix $V_m = 100\%$, with value of σ_m = 24 MPa (from measuring the dissolved and coagulated completely dissolved film which calculated using equation 2.17), the upper-bound and lower-bound are calculated by following equations 2.15 and 2.15 respectively. The data tensile strength versus V_m tendency to follow the upper-bound (Voigt series). This again suggest excellent compatibility between fibres and matrix (equal strain between the two components).

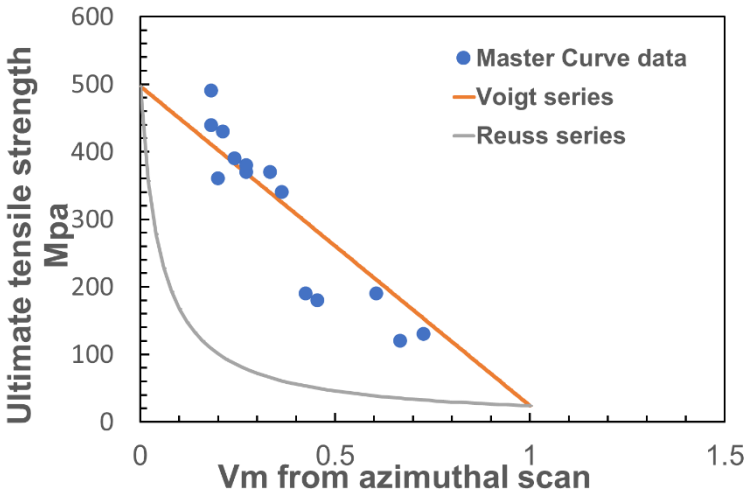

Figure 3.31: Relation between volume fraction V_m from α scan and ultimate tensile strength with prediction of rule of mixtures, Voigt and Reuss series.

By comparing the three methods (Table 3.4), the values of the activation energies of P_2 are the most reliable value and the activation energies of P_2 lower than the activation energy from analysing the measured Young's modulus data. It is seen that there is a much larger uncertainty in the calculation of the activation energy based on the Young's modulus and the ultimate tensile strength measurements, but overall, in close agreement. The two activation energy values within the error of strength measurement and Young's modulus are similar to each other, as shown in Table 3.4.

35 ℃	$\boldsymbol{P_2}$	$\boldsymbol{E}$	$\boldsymbol{\sigma_{UTS}}$
$\boldsymbol{E_a kJ/mol}$	151 ± 3	198 ± 29	158 ± 40

Table 3-4: The comparison between the values of E_{P_2} and E_{V_m} and the E_E and $E_{\sigma UTS}$.

These values quantify the temperature dependence of dissolution, which is a useful parameter in characterising the fraction of matrix formed when creating an all-cellulose composite to obtain the optimum balance of mechanical properties.

3.3 Conclusion.

Wide-angle X-ray diffraction and mechanical test techniques have been used in this research to follow quantitatively the physics of the dissolution, and the resulting mechanical properties of multifilament bundle of a commercial Cordenka multifilament bundle. This was done by dissolving the multifilament bundle in the ionic liquid of 1-ethyl-3-methylimidazilum acetate [C_2mim] [OAc] for different times and temperatures. Optical microscopy and 2θ WAXS was used as the qualitative measurement of the Cordenka multifilament bundle. Optical microscopicy showed that the overall cross-sectional size of the processed multifilament bundle decreased with an increase of matrix proportion during the dissolution process. This method was unsuitable to study the volume fraction of dissolution and could not distinguish between matrix and fibre using ImageJ, therefore, was not used in this research. 2θ WAXS scans and a 2D X-ray image showed that the unprocessed Cordenka multifilament bundle comprised the combination of cellulose II and amorphous, with a small amount of cellulose I.

An azimuthal α scan was employed to determine the dissolution mechanism of the Cordenka multifilament bundle. The azimuthal α scan at an angle 2θ=20.3° (200 reflection) was used to follow the change in the crystal

orientation with time and temperature of dissolution and hence calculate the volume fraction of the dissolved fraction. The P_2 value of the raw fibre was found to be 0.57 while the P_2 value of a fully dissolved film was measured to be 0.25, which is the expected value for perfectly random crystalline orientation in a 2D plane. The measured value of P_2 for the partially dissolved composite multifilament bundle was found to decrease as time and temperature increased, indicating an increase in the random orientated crystal fraction associated with the dissolved and coagulated matrix fraction. The rule of mixtures was applied to the measured P_2 values to calculate the volume fraction v_m of Cordenka multifilament bundle dissolved, using the data from the azimuthal α scan for composite sample.

The Young's modulus values of the partially dissolved regenerated cellulose composite multifilament bundle were also measured for different processing times and temperatures. The time-temperature superposition method was applied to the experimental data of the average P_2 values, Young's modulus and ultimate tensile strength values. Each data set was transformed used time-temperature superposition to form a master curve and then the activation energy was calculated by using an Arrhenius equation (all three measured parameters followed Arrhenius behaviour). The activation energies for the three measures, P_2, Young modulus and ultimate tensile strength were found to be 151± 3 kJ/mol, 198 ± 28 kJ/mol and 158±40 kJ/mol, respectively. The activation energies measured from different methods gave similar values, which indicates they could all be used to follow the dissolution behaviour of the Cordenka multifilament bundle regenerated cellulose fibres. By extrapolating the Young's modulus of the processed Cordenka multifilament

bundle at low temperatures and early times, the modulus of the unprocessed Cordenka multifilament bundle was extrapolated to be E_f =14.8 GPa, which can often be a difficult parameter to measure. Combining this with the modulus of a completely dissolved and coagulated film, allowed the Young's moduli of the processed composite multifilament bundle to be tested against the rules of mixture. The correlation between volume fraction (from the P_2, measurements) and the Young's modulus agreed very well with the predicted parallel rule of mixture. Extrapolating the ultimate tensile strength of the processed Cordenka multifilament bundle at all time and temperatures, the ultimate tensile strength of the unprocessed Cordenka multifilament bundle was extrapolated to be σ_f = 497 MPa, which can often be a difficult parameter to measure. Combining this with the ultimate tensile strength of a completely dissolved and coagulated film, allowed the ultimate tensile strength of the processed composite multifilament bundle to be tested against the rules of mixture. The correlation between volume fraction (from the P_2, measurements) and the ultimate tensile strength shows a tendency to follow the predicted parallel the rule of mixture.

Chapter 4 The dissolution of a Lyocell Multifilament Bundle in the Ionic Liquid of 1- ethyl-3-methyl- imidazolium acetate [C2mim]+ [OAc]-

4.1 Introduction.

Lyocell multifilament is a commercial regenerated cellulose man-made fibre produced by direct dissolution of wood pulp using the Lyocell process (spinning process). The first fibre was produced commercially in 1948 [55]. The Lyocell process is described as eco-friendly, non-hazardous cellulose regeneration process compared with viscose process during manufacturing[36].

Lyocell multifilament bundle is commonly used for technical or industrial applications. The Lyocell multifilament bundle has many excellent physical and chemical properties, and it has a circular cross section. In their paper on regenerated cellulose fibres, Sayyed et al commented on the softness, silky and lustrous nature of the fibres [36] and therefore it has found use for clothing because it has the ability to provide comfortable fabrics. Lyocell multifilament bundle can degrade hydrolytically in mineral acids and importantly are unaffected by most organic solvents and agents.

This chapter will study the dissolution of Lyocell multifilament bundle in the Ionic liquid -1- ethyl-3-methyl- imidazolium acetate [C2mim]+ [OAc]- using both similar and complementary analysis techniques to those described in the previous chapter (Chapter 3) studying Cordenka multifilament bundle. The main technical methods utilised were wide angle X-ray diffraction and

mechanical measurements, as described earlier for Cordenka. Additionally, the geometry of the Lyocell multifilament bundle (twisted rather than untwisted as for Cordenka fibres) allowed an optical technique to be used to directly measure the fraction of dissolution with time. This follows a similar strategy to that previously reported in our group for the study of the dissolution of flax and cotton fibres [76, 77]. The oriented Lyocell multifilament bundle crystals in the fibres were found to transform into randomly oriented cellulose crystals after dissolution and coagulation. Therefore, as reported in the previous chapter, we could analyse the Lyocell multifilament bundle crystalline orientation (specified by the Herman's Orientation factor P_2) and then determine the rate of dissolution with different times and temperatures.

So, the rate of dissolution was determined in three ways, one direct method and three indirect methods. Directly using optical microscopy, indirectly by measuring the average crystal orientation using an azimuthal (α) X-ray scan to measuring the 2nd Legendre polynomial function (P_2), and indirectly from the change in the Young's modulus and also from the change in the ultimate stress of the dissolved and regenerated 'composites' with time and temperature. These four techniques allowed the dissolution behaviour (rate of dissolution) and dissolution activation energy to be measured and compared.

4.2 Results and discussion.

4.2.1 Optical Microscopy.

Optical microscopy was utilised to obtain images of unprocessed and processed Lyocell multifilament bundle composites. Used in conjunction with image analysis software (Image J) the various regions of the processed samples could be determined and then an apparent coagulation fraction could be calculated.

An optical micrograph of the cross- section of an unprocessed Lyocell multifilament bundle can be seen to be composed of a number (a few hundred) of individual fibres, close to each other as shown in Figure 4.1

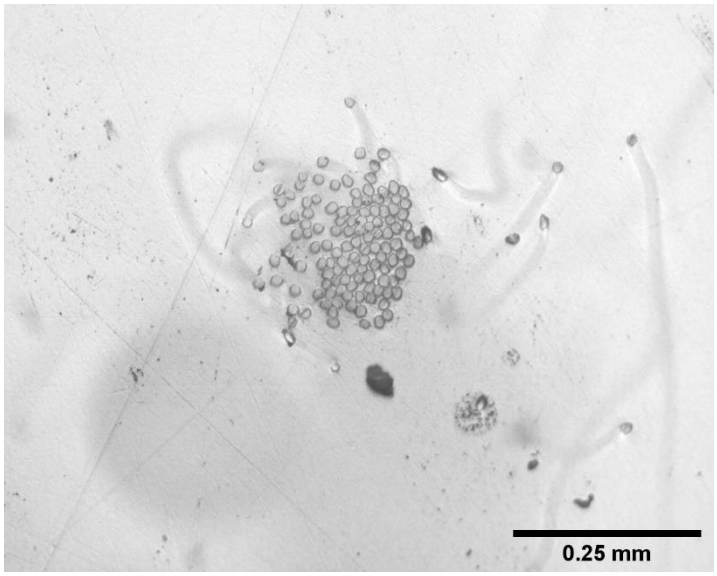

Figure 4.1: Microscopy cross-sectional images of unprocessed Lyocell multifilament at 20 times magnification.

It can be seen that for an unprocessed Lyocell multifilament bundle, the fibres can separate on encapsulation in epoxy, although not significantly (and not as much as for the unprocessed Cordenka untwisted multifilament bundle). The dissolution process started at 30 ℃, and the cross sections of the processed Lyocell multifilament bundle for 1,2, 3 and 5 hrs are shown in Figure 4.2. It can be seen that the individual fibres are bound together with a proposed very thin coagulated Lyocell matrix, and so the multifilament bundle does not separate in the epoxy resin. The fibre encapsulation procedure is shown earlier in section 2.6.1 Figure 2.7. This could be due to the ionic liquid [C2mim]+ [OAc]- not easily penetrating between the twisted Lyocell multifilament bundle. This leads to the outer area of the multifilament bundle to dissolve first creating the matrix around the core as the inner core of undissolved multifilament bundle decreases in size. On average, the average outer area remains the same that transforming dissolved Lyocell multifilament bundle into matrix to provide a close packing fibre microstructure.

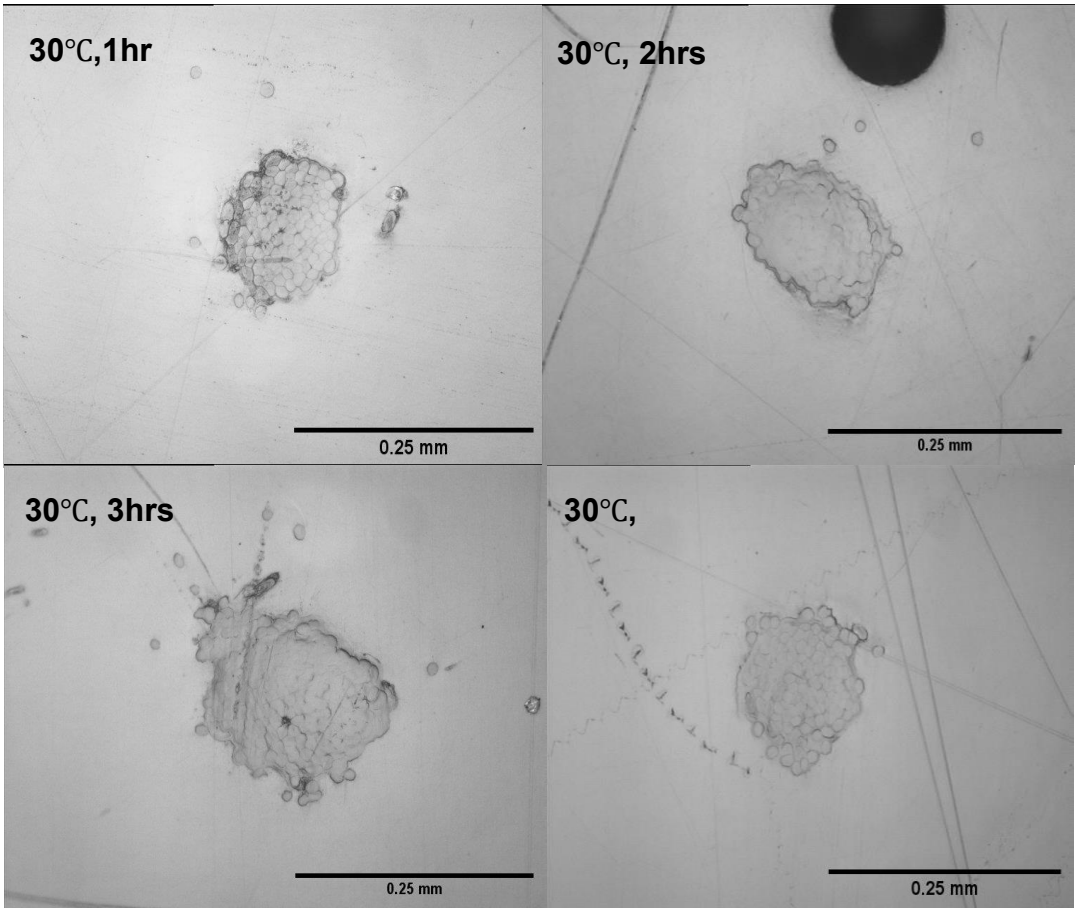

Figure 4.2: Microscopy cross-sectional images of processed Lyocell multifilament bundle fibre at 30℃ for different times at 20 times magnification.

The outer matrix layer started increasing around the inner core of area at a processing temperature of 35℃ and from 2 hours with an increase of time, as shown in Figure 4.3. This dissolved and coagulated matrix fraction continuously increased with higher temperatures (37℃,40℃ and 45℃) and longer processing times. Resulting from that, the final size of inner core area of the Lyocell multifilament bundle composites gradually decreased as shown in Figure 4.4.

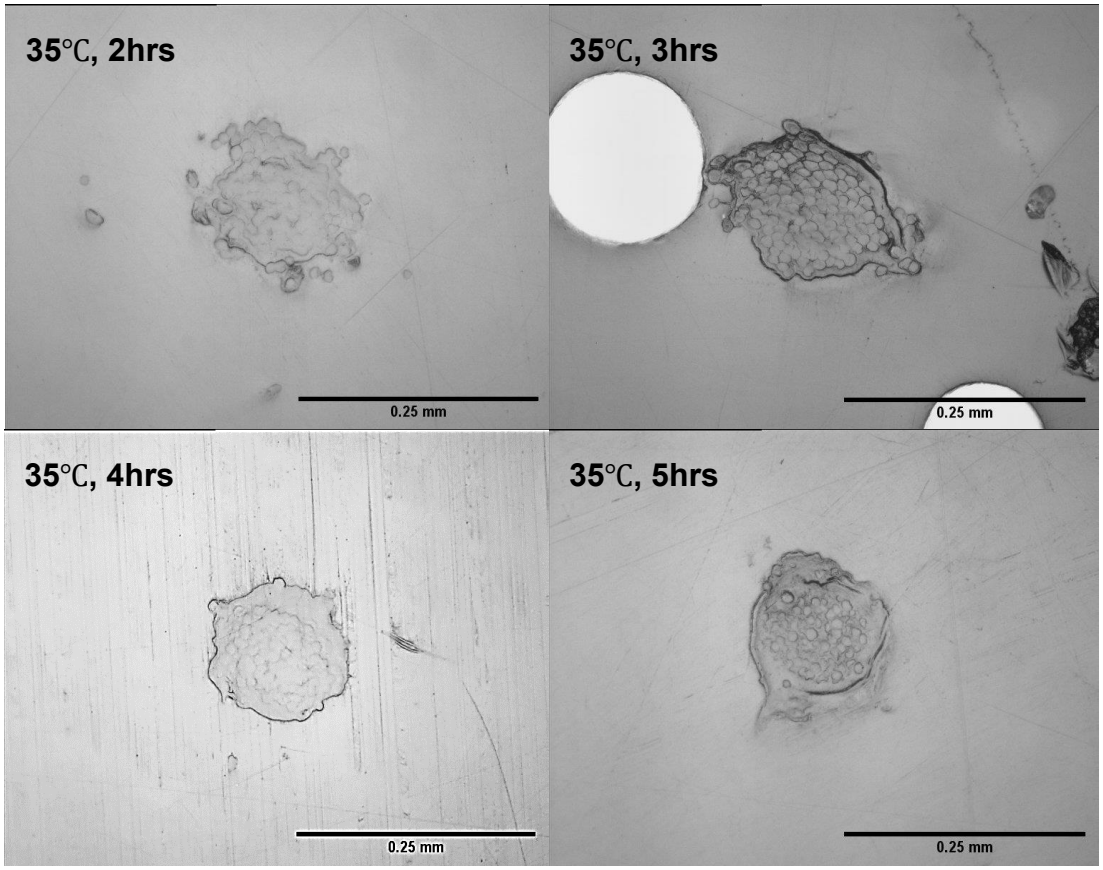

Figure 4.3: Cross sections of processed multifilament bundle fibre at 35°C for 2,3,4 and 5 hours. The coagulated fraction can be seen to grow as a function of time at 20 times magnification.

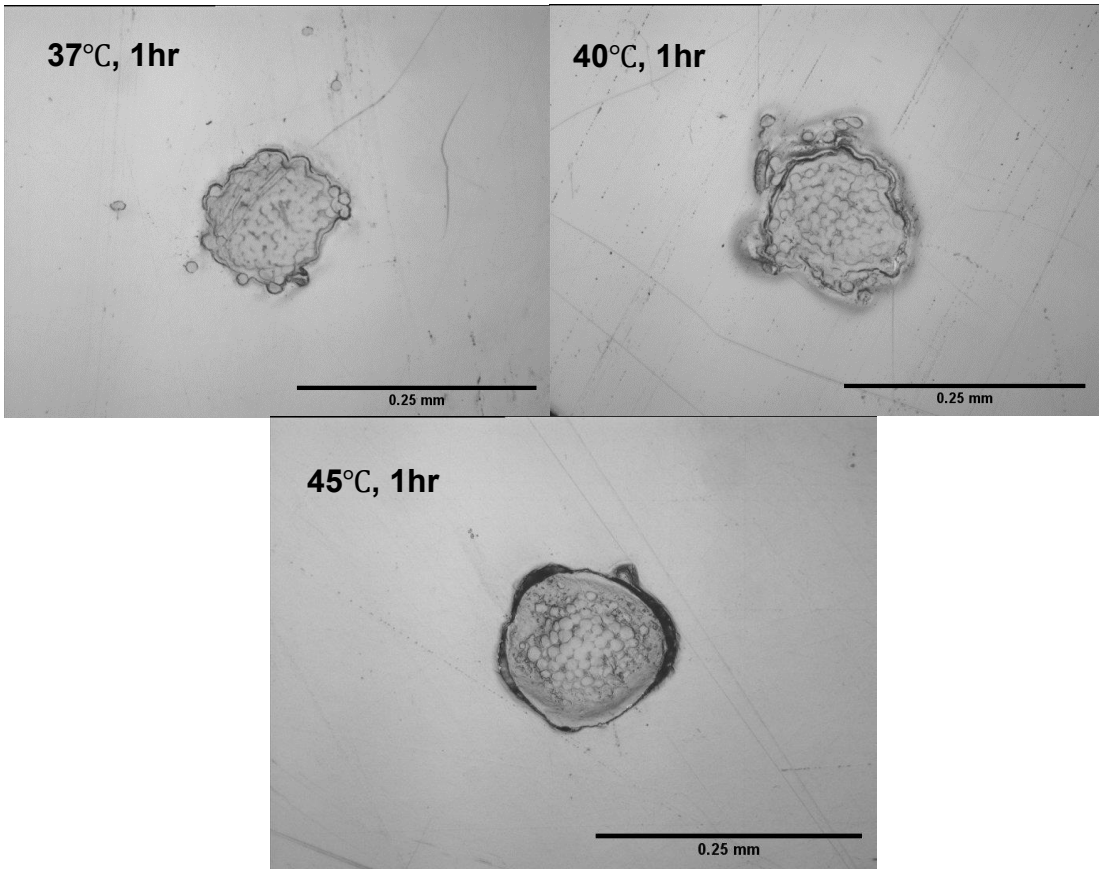

Figure 4.4: Cross sections of multifilament bundle fibre at various temperatures; 37℃, 40℃ and 45℃. The coagulated fraction can be seen to grow as a function of temperature and time at 20 times magnification.

4.2.1.1 The Measurement of The Different Regions of a Partially Dissolved Lyocell Multifilament Bundle.

The calculation of the area of the two distinct regions (dissolved outer region of matrix and inner area of undissolved fibres) was done by sketching with ImageJ and colouring around the inner core (yellow) and the outer perimeter layer (green), as shown in Figure 4.5. The outer layer area (which combines both the undissolved multifilament bundle and the dissolved fraction) was found to be independent of time and temperature as dissolution proceeded, as the original fibres were replaced by dissolved and coagulated material. This results strongly suggests that density of the dissolved and coagulation fraction is very similar to the original fibres. This is not surprising as the original multifilament bundle of regenerated fibres contained no significant internal voids unlike plant fibres. For this reason, this parameter could not be used to determine the dissolution activation energy. However, we could measure both the decrease of the inner core (which always contained the remaining undissolved fibres) and the increase in the area and thickness of the dissolved and coagulated outer ring. These methods were explained in detail in Chapter 2 section 2.4. This optical method is considered as an efficient technique to directly measure the area of dissolved and coagulated Lyocell multifilament bundle samples [125].

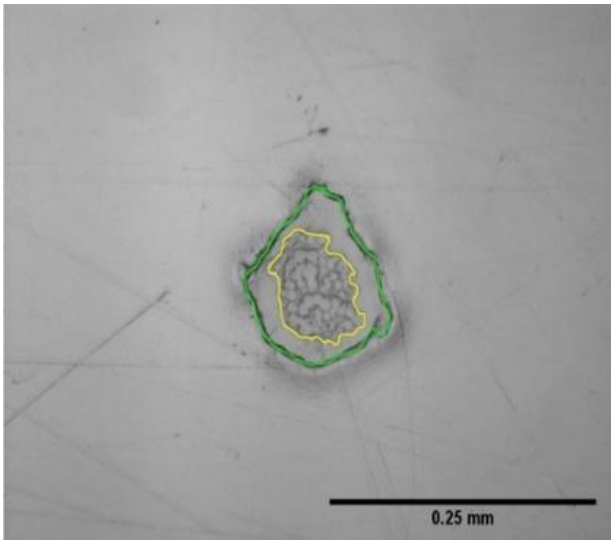

Figure 4.5: the sketching of inner core (yellow) and outer area (green) of Lyocell multifilament.

4.2.1.1.1 The Measurements of The Outer Layer Dissolved and Coagulated Area of Lyocell Multifilament Bundle.

The calculation of the outer layer area of the Lyocell partially dissolved bundle composite samples was the first method tried to calculate an activation energy during the dissolution process by sketching the outer layer using software (image J). The outer perimeter area shown in green in Figure 4.5 (which is also considered as total area) of the processed Lyocell multifilament bundle was determined between the processing temperatures of 35℃ and 45℃ for various dissolution times. The relation between the outer perimeter area and the dissolution time is shown in Figure 4.6. The results show that within the scatter of the measurements that the outer perimeter area was constant during the dissolution process and therefore the data points could not be used to calculate an activation energy. The average value of all the data of the outer perimeter area of the processed Lyocell multifilament bundle was calculated

to be 0.0178 ± 0.001 mm^2 and indicates the outer area was not changed during the dissolution process, with the dissolved and coagulated matrix layer replacing the original Lyocell multifilament bundle. This also suggests that the density of the dissolved and coagulated material is very similar to the original fibres. By drawing lines between these values in Figure 4.6, the outer area of unprocessed is seen to be higher than the processed Lyocell multifilament bundle, which has spread when encapsulated in the epoxy resin as the fibres are not bonded together until immersed in the ionic liquid.

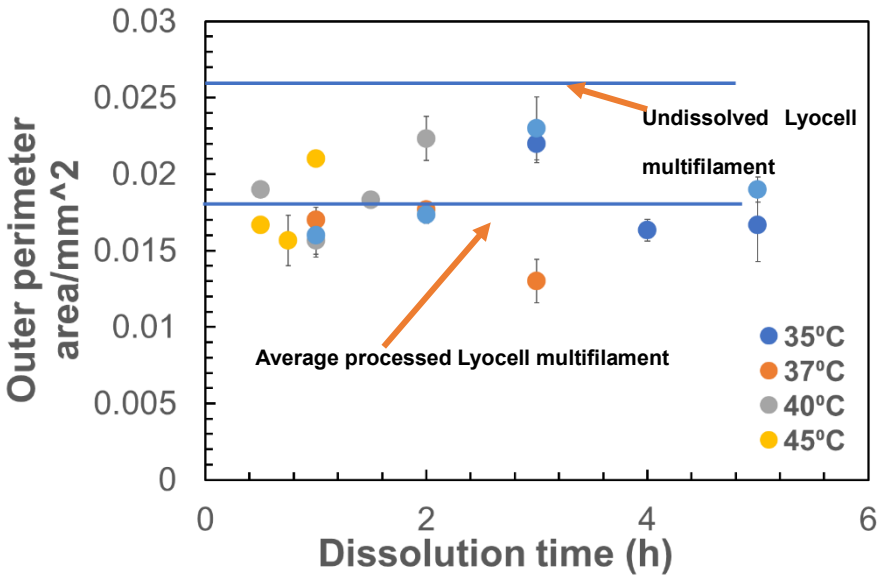

Figure 4.6: The average calculated outer perimeter area at different dissolution times and temperatures between 30℃ and 45℃. for processed Lyocell multifilament.

4.2.1.1.2 The Measurements of Inner Core Area of Lyocell Multifilament Bundle.

The second method to follow the dissolution process was the calculation of the inner core area of the Lyocell multifilament bundle composites, with temperature and time, which is within the yellow region shown in Figure 4.5.

The sketching in Figure 4.5 was drawn by image J, and it was utilised to measure the reduction of the inner core area and then this was used to calculate the activation energy. Due to their only being a very thin matrix layer formed at 30℃ it proved hard to measure the boundary between the two regions, so the measurement of the inner area of the Lyocell multifilament bundle was started at 35℃. The inner core area decreased with time and all temperature regimes: 35℃, 37℃, 40℃ and 45℃, as shown in Figure 4.7.

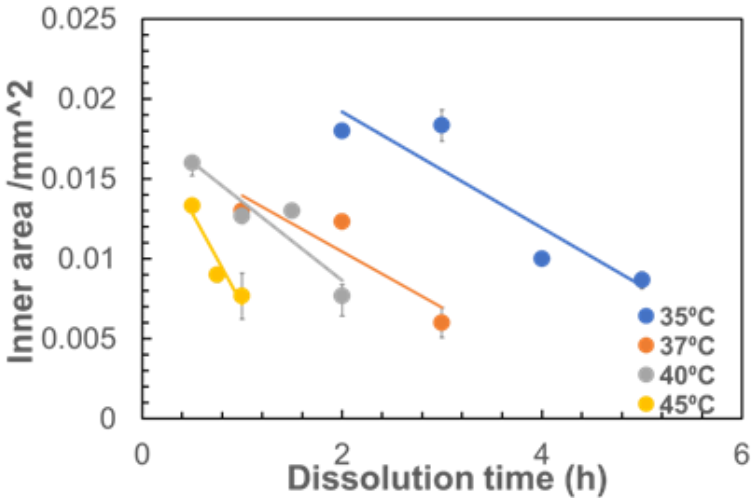

Figure 4.7: The average for three samples calculated inner area at different dissolution times and temperatures for processed Lyocell multifilament bundle. The error bar is too small and within the data point.

The time-temperature superposition method was applied to the data of the inner core area to follow the dissolution behaviour of the Lyocell multifilament bundle. The values of inner core area were shifted with time and temperature, using the temperature of 35℃ as the reference temperature. The data points were then found to collapse into a single master curve. The inner core area as function of time and temperature after superposition is shown in Figure 4.8a (plotted against log time). This then allowed the relation between inner core area with linear dissolution time (at a reference temperature of 35℃) with using the average value of outer perimeter area 0.0178 mm^2 as the intercept, which calculated in above section, to be plotted as shown in Figure 4.8b. The complete dissolution of the Lyocell multifilament bundle would be predicted to be achieved after 2hrs dissolution time. The best final polynomial to fit the data was as shown in Figures 8b and was as follow:

$$\text{Inner area} = -0.0034x^2 + 0.0012x + 0.017 \quad (4.1)$$

Where inner area is in mm^2 and x is the time in hours. Figure 4.8c shows that plotting the log of the shift factors ($\ln a_T$) against the inverse of temperature gave a linear relationship, allowing the activation energy value to be calculated by applying the Arrhenius equation 3.2. The value obtained was 141±15 kJ/mol, where the uncertainty again comes from the LINEST function in Excel.

.

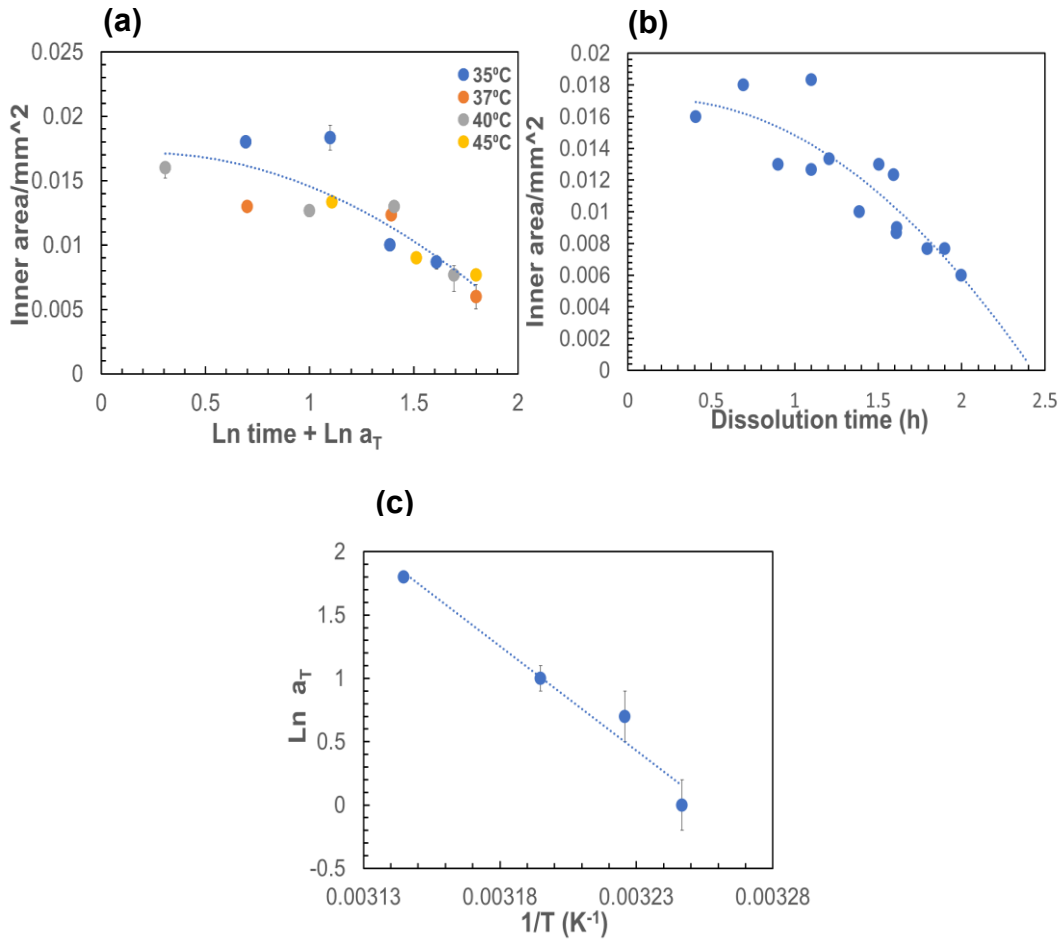

Figure 4.8: a) the master curve of relation between inner area and shifting time at various temperatures of Lyocell multifilament bundle. b) the resultant linear master curve between inner area and dissolution time. d) the $ln\ a_T$ plotted against the inverse of temperature and resulting an activation energy.

The time temperature superposition method was separately applied using 37℃, 40℃ and 45℃ as reference temperatures to calculate the activation energy, where the data was shifted to each of these temperatures in turn. Figure 4.9 shows the final master curve of data at 37℃. The same master curve at 40℃and 45℃, is shown in Figures 4.9 b and c, all plotted against log time.

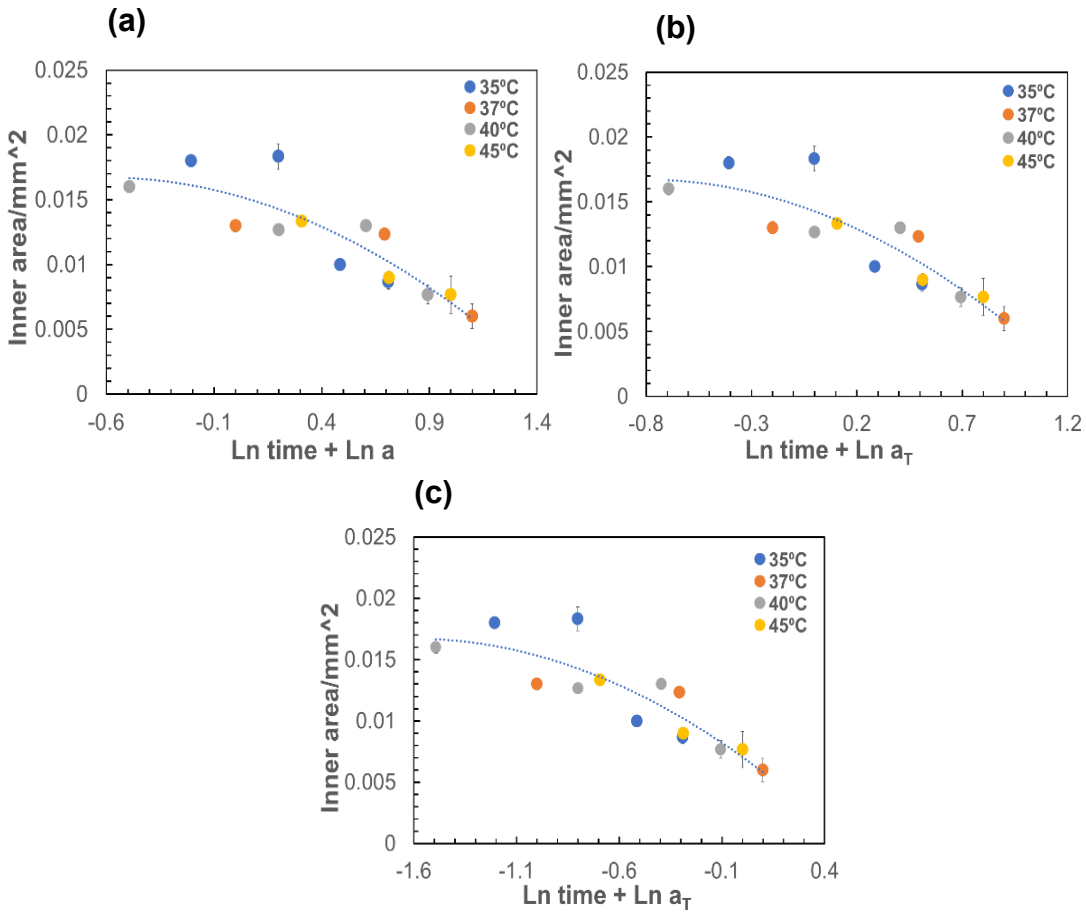

Figure 4.9: (a) is the final master curve of data at 37℃, (b) the final master curve of data at 40℃ and (c) the final master curve of data at 45℃.

Shift Factor, Intercept Arrhenius Dependence.

The “intercept method” is based on the relationship between the shift factors and inverse temperature through the Arrhenius equation 3.2, which was used earlier to calculate the dissolution activation energy. All data was shifted to 35℃ to create a master curve at this temperature, then the whole process was repeated again for 37℃,40 ℃ and 45℃. The shift factors were plotted as a

function of inverse temperature to give an activation energy and intercept, as for 35℃, see Figure 4.10.

The intercept values from these Arrhenius plots were itself then plotted against the inverse reference temperature, see Figure 4.11, where it can be seen that the intercepts themselves follow an Arrhenius type behaviour. Starting with the Arrhenius equation (equation 3.2) and setting a_T as $a_{T_{ref}}$, gives equations 4.2-4.4.

$$T = T_{ref} \tag{4.2}$$

$$\ln a_{T_{ref}} = \ln A - \frac{E_a}{RT_{ref}} \tag{4.3}$$

The shift factor at the reference temperature must equal one, hence $\ln(a_{T_{ref}})$= 0, since no shifting is needed for the data already at the reference temperature, therefore

$$ln\ \mathrm{A}_0 = \frac{E_a}{RT_{ref}} \tag{4.4}$$

The important result is that intercept $\ln \mathrm{A}_0$ in each of these graphs is itself dependence temperature $\ln \mathrm{A}_{37}$, $\ln \mathrm{A}_{40}$ $\ln \mathrm{A}_{45}$, and $\ln \mathrm{A}_{35}$ are 54.71, 54.21, 56.95 and 55.31 for temperatures 37℃ Figuer.4.10(a), ,40℃ Figuer.4.10 (b) and 45℃ Figuer.4.10 (c), respectively and 35℃ Figure 4.9.

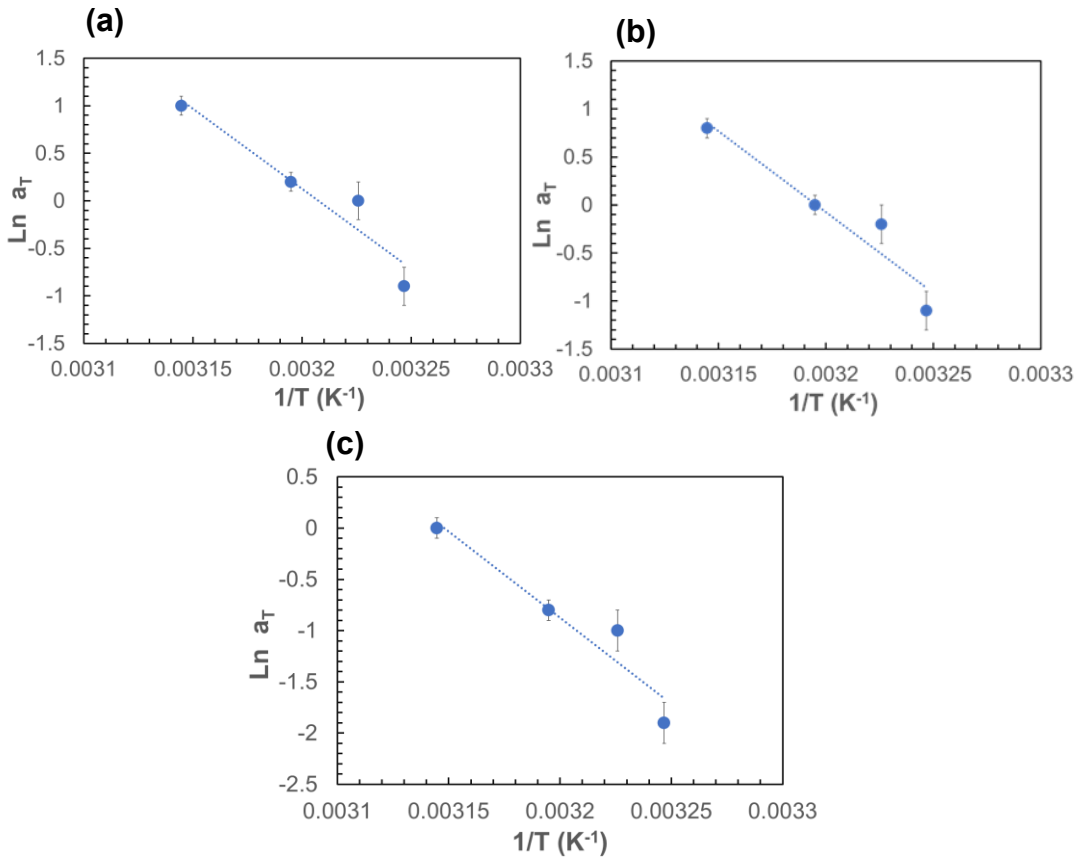

Figure 4.10: (a) $ln\, a_T$ plotted against the inverse of temperature at 37℃ as reference temperature, (b) $ln\, a_T$ plotted against the inverse of temperature at 40℃ as reference temperature and (c)) $ln\, a_T$ plotted against the inverse of temperature at 45℃ as

The correlation between $ln\ \mathrm{A}_0$ and ${}^{1}/_{T_{ref}}$ gives the gradient $\frac{E_a}{R}$ to give a further way to calculate E_a, as shown in Figure 4.11. This plotted graph gave a similar E_a as previously calculated for the four different temperatures (at 30℃, 35℃, 40℃ and 45℃) equal to 141 ± 15 kJ/mol. This is approximately the same value of activation energy that was calculated from the time-temperature superposition method. It has been found that the “intercept method” is very sensitive to any non-Arrhenius dependence and is a useful validation of the approach taken in this work, as seen in the previous chapter studying the Cordenka samples.

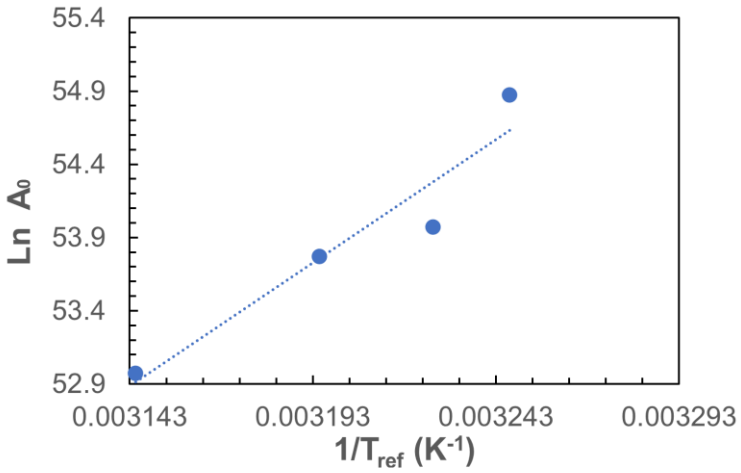

Figure 4.11: The correlation between $ln\ \mathrm{A}_0$ and $^1/_{T_{ref}}$

4.2.1.1.3 Thickness Measurements of Lyocell Multifilament Bundle.

As well as measuring the decrease of the inner core with temperature and time, direct measurements of the dissolved and coagulated layer were also taken as shown in Figure 4.12. In this method, four diameters were measured across the fitted outer perimeter area (green ring) of the whole Lyocell multifilament bundle and the inner area (yellow ring) of the undissolved/central Lyocell multifilament bundle to calculate the change in the thickness or the thickness X of the dissolved and coagulated 'matrix layer' with temperature and time. The changes in the radial length of the outer area ring and inner core area were measured, labelled with a red arrow line and a dark blue arrow line, as shown in Figure 4.12.

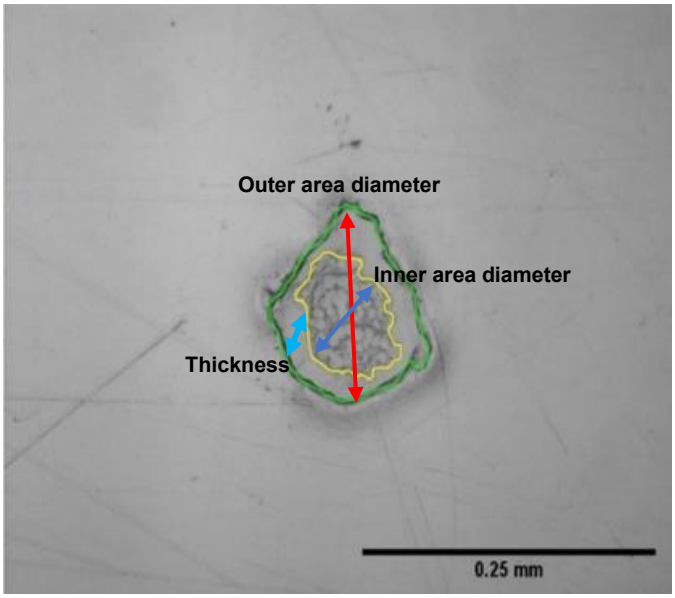

Figure 4.12: the cross section of the processed lyocell multifilament bundle obtained from an optical microscope, in which the undissolved section dark blue arrow, the outer ring dimeter are indicated in red arrow, and thickness in double light blue arrow.

The measurement of the thickness X was based on the difference between the outer area and the area of the inner undissolved region which given by:

$$X = (Outer\ diameter - Innear\ dimeter)/2 \quad (4.5)$$

where X indicates the average thickness of the dissolved and coagulated 'matrix' layer of the partially dissolved Lyocell multifilament bundle. In this measurements, three fibres were used, and 4 sampling points across the composite cross section images leading to a total of 12 measurements for each processing condition. The means thickness and standard errors were calculated, and the standard errors can be seen as the error bars in Figure 4.13. It can be seen that the error bars are small which we consider validation of this method.

The results of this thickness measurement are shown in Figure 4.13, and it is seen that the thickness of the outer dissolved and coagulated layer increases with time and temperature.

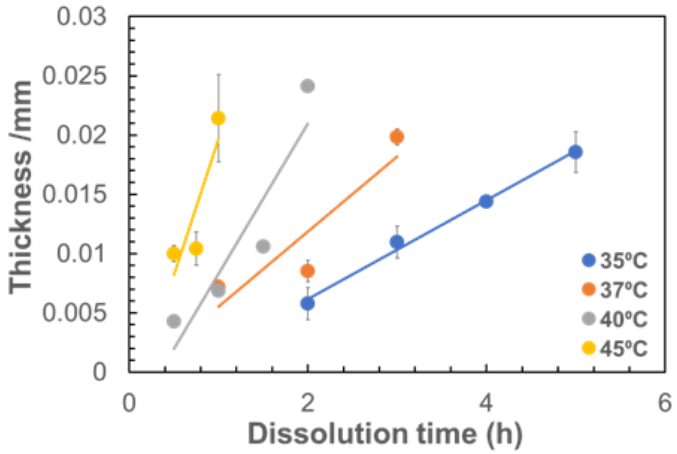

Figure 4.13: the relationship between the thickness values and dissolution time, error bars with data points.

The time-temperature superposition method was then applied to the data of thickness to follow the dissolution behaviour of the Lyocell multifilament bundle as described above for following the associated decrease in the area of the undissolved multifilament bundle. The thickness values were shifted with time and temperature in ln (time) space, using the temperature of 35℃ as the reference temperature. The data points were again found to collapse into a single master curve. The thickness of the dissolved fraction of the Lyocell multifilament bundle composite as function of time and temperature after superposition is shown in Figure 4.14a against ln(time) and with linear dissolution time, as shown in Figure 4.14b. Figure 4.14c shows that plotting $\ln a_T$ against the inverse of all temperatures gave a linear relationship, then

the activation energy, E_a value was calculated by using the Arrhenius equation (equation 3.2). The value of $E_a$obtained was 127±14 kJ/mol.

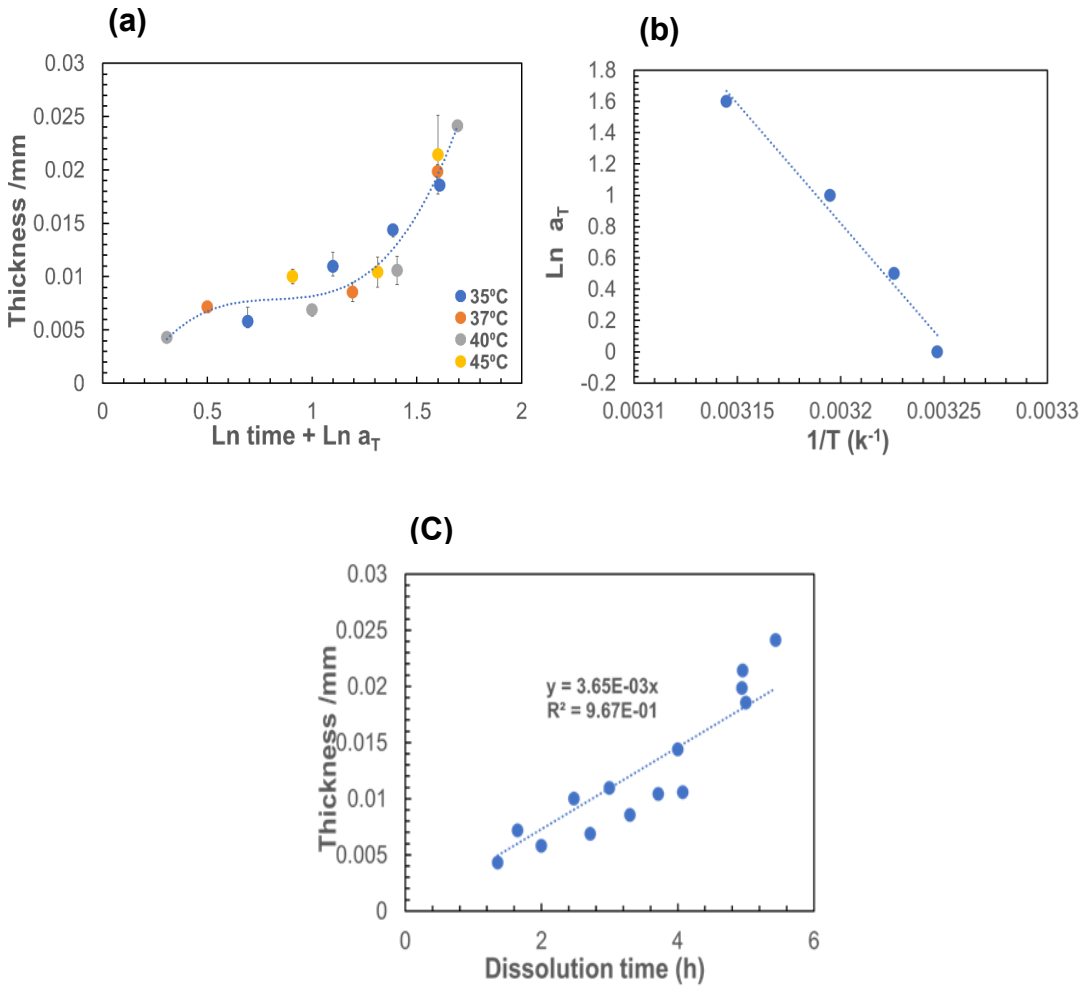

Figure 4.14: a) the master curve of relation between thickness and shifting time at various temperatures of Lyocell multifilament bundle. b) the resultant linear master curve between thickness and dissolution time. d) the $ln\, a_T$ plotted against the inverse of temperature and resulting an activation energy.

The linear relation between the thickness versus the dissolution time using the temperature of 35℃ as the reference temperature, indicated an increase of the matrix of Lyocell multifilament bundle composite. The same result was found for the other three reference temperatures of 37℃,40℃ and 45℃ after

applied the TTS shifting factor as shown in Figures 4.15. The data from Figures 4.15a-d could then be used determine the dissolution speed via using the gradients of these graphs of thickness vs the dissolution time for each reference temperature 35℃, 37℃,40℃ and 45℃. The gradient values indicated to the dissolution speed were 3.65E-03, 6.02E-03, 1.17E-02 and 1.81E-02 in units of mm/hour for 35℃, 37℃,40℃ and 45℃ respectively.

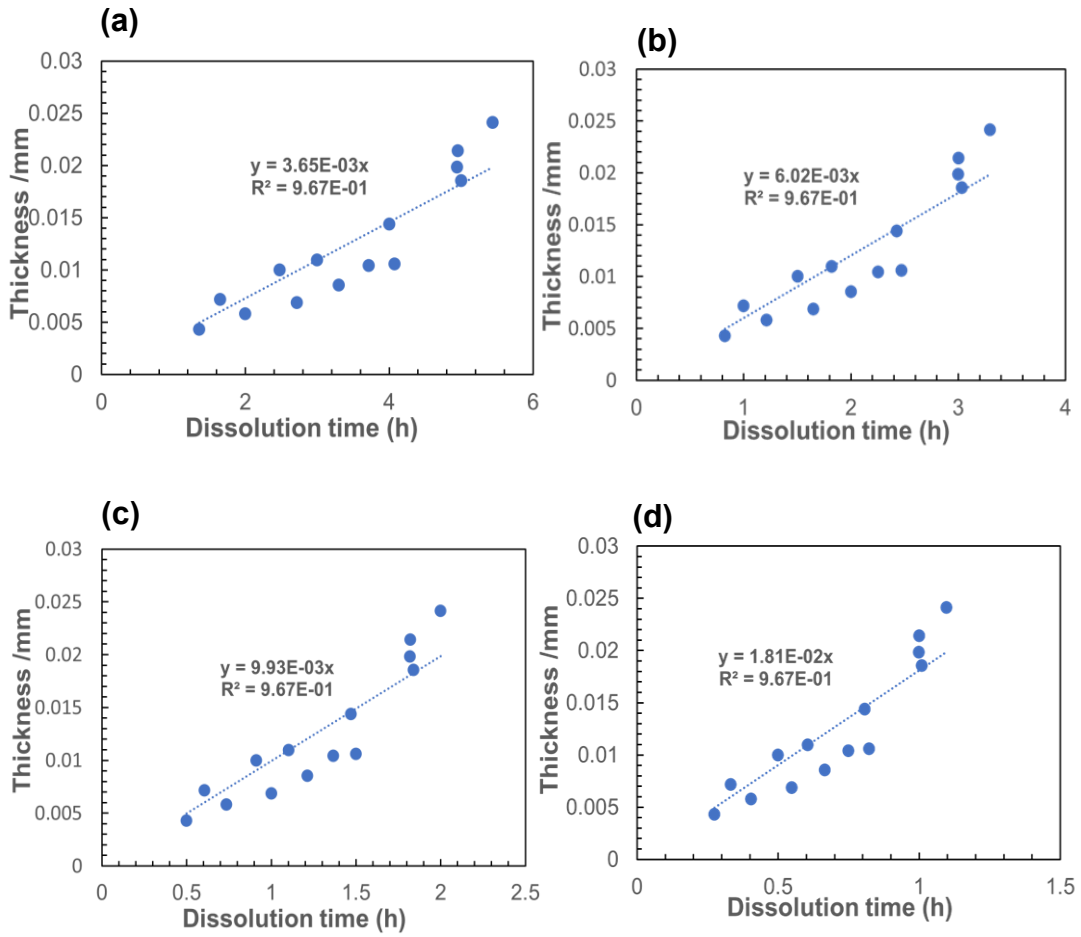

Figure 4.15 : a) The linear dissolution time with thickness at 35°C.b) The linear dissolution time with thickness at 37°C.c) The linear dissolution time with thickness at 40°C and d) The linear dissolution time with thickness at 45°C.

Figure 4.15 above shows that the thickness of the dissolved fraction changes linearly with time for all four temperatures. Other published literature has reported that the thickness can be linear with time or related to the square route of time if the dissolution process is controlled by diffusion, which indicates applicability to the Fick's approach [126, 127]. Fick's approach describes the rate of diffusion. In this diffusion, enormous number of solvent molecules penetrate fibres and make solution. The molecules of solution move randomly and flow smoothly from high concentration area to low concentration area and its concentration becomes equal throughout space [128]. In our case, the thickness increases linear with time. Our hypothesis is therefore that the dissolution is not diffusion controlled (that is dependent on $t^{1/2}$) but proceeds at a constant velocity which increases as the temperature increases. Therefore, we could not use Fick's approach to determine the diffusion from the thickness measurements. As a comparison, the work on Hemp in our group[74] showed that in this material the coagulation layer thickness increased linearly with the square root of dissolution time, and so diffusion controlled. We speculate that for our current work, there is another, as yet undiscovered limiting factor, such as the crystal structure of the Lyocell multifilament bundle which is cellulose II (and also potentially the geometry most likely (twisted fibre). Cellulose II is more stable than cellulose I. Other workers in our group have measured the activation energy of cellulose I fibres and found values of 58 $\pm$ 4 kJ/mol for flax [75] and 78 ±2 kJ/mol for hemp [74] using the same ionic liquid, compared to our overall average value from the different methods of 150 $\pm$ 13 kJ/mol for Lyocell. We could speculate that we

would find the same linear dependence for Cordenka multifilament bundles, but the untwisted nature did not allow a thickness measurement to be made.

The activation energy theoretically calculated from the dissolution speed calculation and compared with the activation energy was obtained experimentally from thickness measurement. Using the Arrhenius equation 3.2 and modelling to dissolution speed.

$$\ln v = \ln v_0 - \frac{E_a}{RT} \tag{4.6}$$

Where v is the dissolution speed, v_0 is the pre-exponential factor. It was plotting $\ln v$ speed against the inverse of temperatures gave a linear relationship, to find the activation energy, E_a value from the gradient, as shown in Figure 4.16. The value of $E_a$obtained was 127 ±13 kJ/mol which is in excellent agreement with the value E_a 127 ±14 obtained from the thickness of the outer dissolved and coagulated layer with time and temperature as expected.

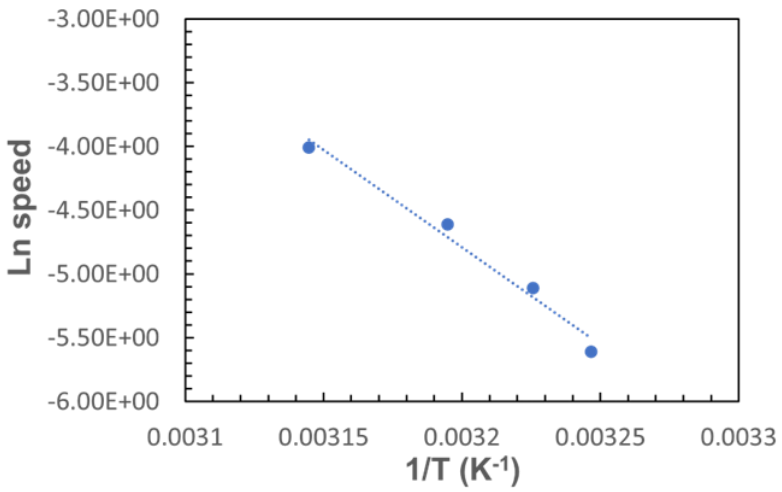

Figure 4.16: The corelation between Ln speed and the inverse of temperatures.

4.2.1.1.4 The Measurements of The Coagulation Fraction of the Lyocell Multifilament Composite.

The values of the inner core area and the outer perimeter area were used to calculate the fraction of the dissolved and coagulated matrix fraction with time and temperature. The equation to calculate the coagulation fraction was as follows:

$$CF = \left(\frac{A_T - A_C}{A_T}\right) \quad (4.7)$$

Where A_T is total area of the filaments cross section the area of the filaments and A_C is the comprised of coagulated cellulose from central fibre.

Due to there being only a very thin matrix formed at 30℃, it proved hard to measure accurately, and so the measurement of the inner area of the Lyocell multifilament bundle composite started at 35℃ as mentioned above. The calculation of the ratio started from 35℃ (2hrs upwards) and was used to measure the coagulation fraction, C_f between the inner core and the coagulation matrix (outer layer) of dissolved Lyocell multifilament bundle using equation 2.15. The coagulation fraction, C_f increased with time at all processing temperatures: 37℃, 40℃ and 45℃, as shown in Figure 4.17. The relative shape of this data mirrors that shown in Figure 4.13 where the thickness of the outer later was measured.

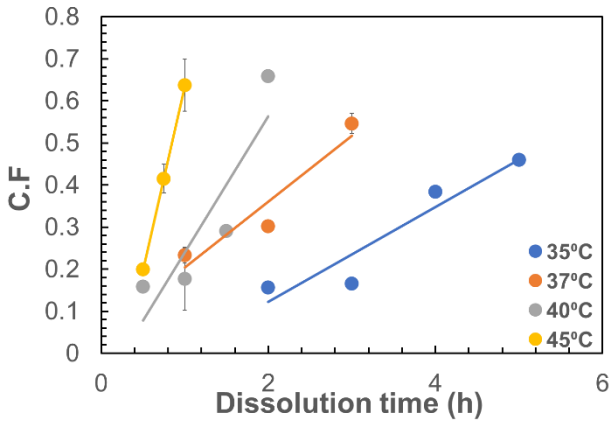

Figure 4.17: the Correlation between the average calculated coagulation fraction, C_f and different dissolution times and temperatures for processed Lyocell multifilament bundle. Error bars with data points.

Figure 4.18 shows a typical C_f curve for a single dissolution temperature 37℃, the data points represented the averageC_f values taken from individual fibre cross sections processed at three times (1hr, 2hrs and 3 hrs).

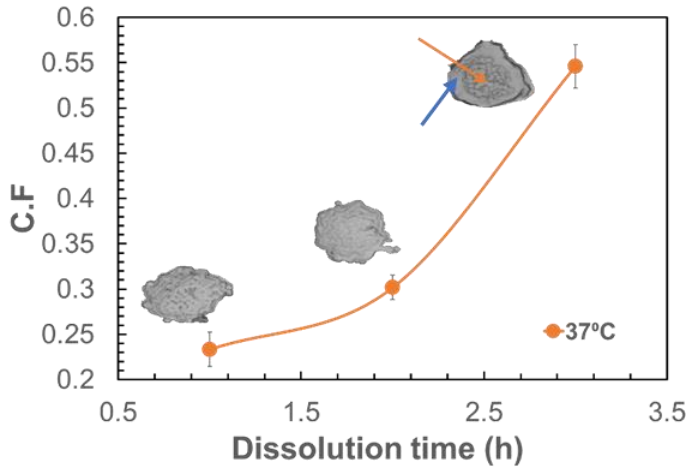

Figure 4.18: the single dissolution temperature of Lyocell multifilament bundle at 37℃, orange arrow indicates to the decrease in the inner core and blue arrow indicates to an increase of coagulation fraction, C_f at 3hrs.

The time-temperature superposition method was once again applied to the data of the coagulation fraction C_f with time and temperature to follow the dissolution behaviour of the Lyocell multifilament bundle. The data of C_f is shifted with time and temperature, using the temperature of 35℃ as the reference temperature. The data collapsed into a single master curve. The coagulation fraction as function of time and temperature after superposition is shown in Figure 4.19a plotted against log time. The relationship between the coagulation fraction C_f and the linear dissolution time, is as shown in Figure 4.19b. The complete dissolution of the Lyocell multifilament bundle would be predicted to be achieved after 8h dissolution time at 35°C, as the coagulation fraction area value of completely dissolved fibers was extrapolated to 1. Figure 4.19c shows that plotting $\ln a_T$ against the inverse of temperature gives a linear relationship and from that the activation energy value was calculated by applying the Arrhenius (equation 3.2). The value obtained was 141 ±16 kJ/mol. The reduction of the inner core area correlated to the decrease of coagulation fraction, therefore the activation energy value from coagulation fraction C_f was in excellent agreed with the activation energy from measuring inner core area method as expected as the data comes from the same source mearing relatives area. It also agreed with measuring the outer layer thickness. These three values are shown below in Table 4.1.

35℃	**C.F**	$\boldsymbol{X}$
$\boldsymbol{E_a kJ/mol}$	141 ± 16	127 ± 14

Table 4-1: The values of E_{Cf} and $E_{T.}$

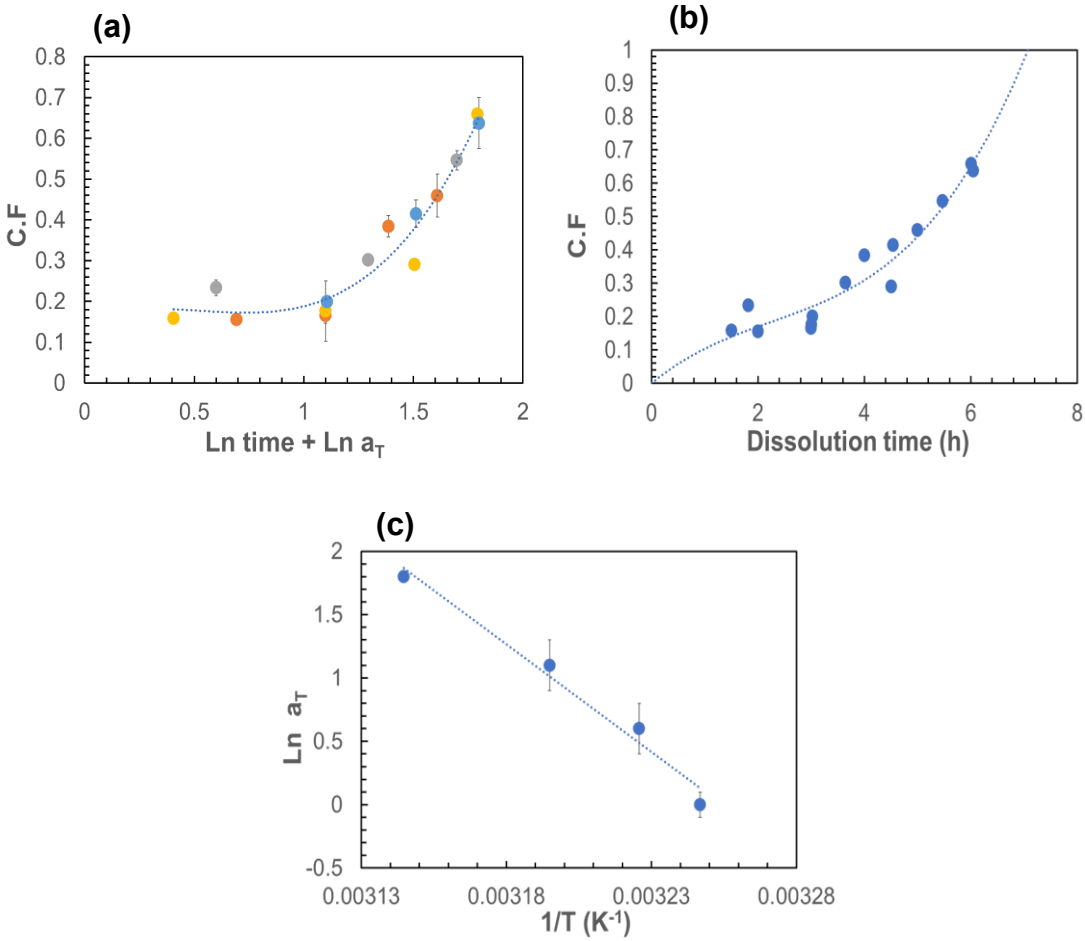

Figure 4.19: a) The master curve of relation between the average calculated coagulation fraction, C_f and shifting time at various temperatures of Lyocell multifilament bundle. b) the resultant linear master curve between inner area and dissolution time. d) the $ln\, a_T$ plotted against the inverse of temperature and resulting an activation energy.

4.2.2 Wide angle of X-ray Diffraction.

4.2.2.1 Two-Dimension of X-ray Diffraction Pattern.

A 2D X-ray image was used to qualitatively examine the crystal structure and Bragg peaks of the Lyocell multifilament bundle. The procedure was applied

to the Lyocell multifilament bundle as mentioned in Chapter 2 section 2.2.3.1 (methodology chapter). Quantitative measurement of the crystal orientation was obtained from an α circumferential scan setting in two dimensions (2D) from -90° to 90° at the same Bragg angle as used for the Cordenka multifilament bundle, which is the angle with the maximum signal (2θ = 20.3°). The results of the 2D X-ray image are shown Figure 4.20, where the dark arcs correspond to Bragg peaks of cellulose II. The peaks with reflections $1\bar{1}0$, 110, 200 were positioned at 12.4°, 20.2°, 21.8° of 2θ angles respectively, these peaks indicated cellulose II of Lyocell multifilament bundle. The peak of cellulose I did not appear in the 2D image; this might be due to the percentage of cellulose I being so low compared to the amount of cellulose II in the sample suggesting that the Lyocell multifilament bundle is predominantly cellulose II with an amorphous fraction. As for the Cordenka multifilament bundle, there were other peaks with reflections 012 in cellulose II not on the equator. These peaks were also present and studied for the Cordenka multifilament bundle. This can be seen in the 2D X-ray scattering at a circumferential angle of ~+/-60° (see also Figure 4.20) and a 2θ value of 20.3° as described in ref [113]. As this 012-reflection plane has a very similar value of 2θ to the chosen equatorial position with maximum signal intensity (20.3°), then this reflection will appear in a circumferential α scan (as shown schematically in Figure 4.23). We have proposed to include both these reflections in the determination of P_2 from a numerical integration between -90 and +90. Our hypothesis is that following the change of any appropriate parameter with time and temperature, allows us to investigate time-temperature superposition and determine an activation energy for dissolution. However as will be seen from Figure 4.23,

these outer peaks are more spread out compared to the Cordenka multifilament bundle.

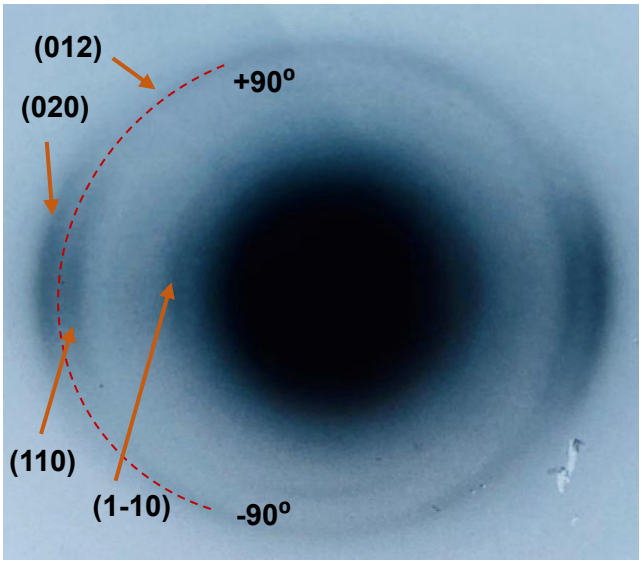

Figure 4.20: 2D X-ray scattering pattern from unprocessed Lyocell multifilament showing the α circumferential scan setting in two dimensions (2D) from -90° to 90° (red dashed line) at 2θ = 20.3° and how this includes the 012 reflection

4.2.2.2 2θ Scan of Lyocell Multifilament Bundle.

The equatorial 2θ scan (α = 0°) was used to study the crystal structure of the Lyocell multifilament bundle and any change during the dissolution process. The experimental raw data of this 2θ scan of unprocessed Lyocell multifilament bundle shown in Figure 4.21.

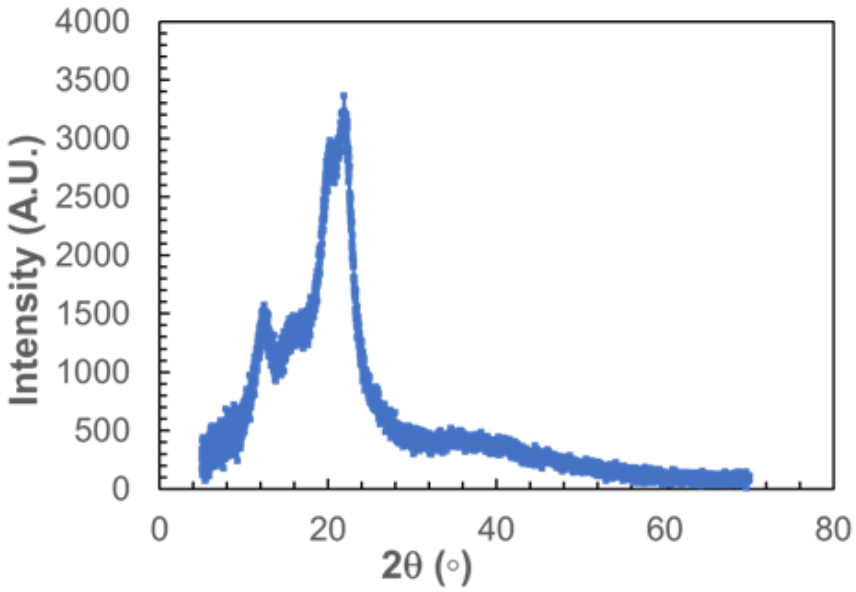

Figure 4.21: 2θ scan of unprocessed Lyocell multifilament.

The deconvolution (curve fitting) method was applied again to the raw data of the Lyocell multifilament by using special software (spreadsheet) taken from ref [114] to analyse the amount of cellulose I and cellulose II and amorphous. An example of this fitting technique can be seen in Figer 3.5, which shows the data fitted by the combination of the peaks of cellulous 1 and 2 and amorphous. The original Bragg peak locations in 2θ scan were used as guide to identify cellulose I and cellulose II of unprocessed Lyocell multifilament bundle.

This fitting method was then tasked with fitting the raw data using a combination of amorphous, cellulose I and cellulose II peaks in superposition. The results of deconvolution method with fitting data of unprocessed Lyocell multifilament bundle are shown in Figure 4.22.

Peaks of Cellulose I show in blue, orange and brown, while cellulose II peaks are dark blue, green, and grey, all were allowed to move ± 2° either side of

their expected positions as given in the literature [2, 115-118]. The amorphous peak was placed around 18° in 2θ scan [95, 119] and was fitted with a single peak to unprocessed Lyocell multifilament bundle data. The deconvolution (Figure 4.22) shows that the cellulose I fraction is very small, as seen with the Cordenka multifilament bundle, and as expected from the 2D x-ray image.

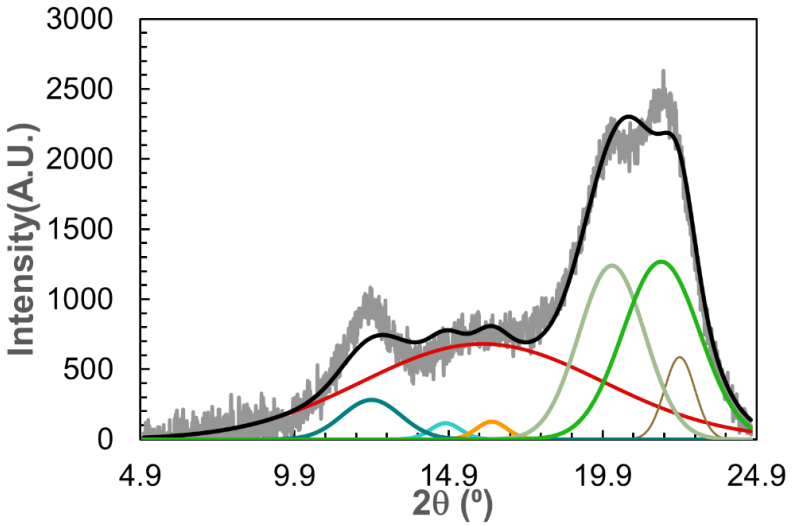

Figure 4.22: The fitting data of unprocessed Lyocell multifilament bundle after combination of cellulose I, cellulose II and Amorphous.

After deconvolution, the sum of the fitted crystalline peaks of cellulose to the total area of crystallinity and amorphous under the diffractogram, through the deconvolution (curve fitting) equation 2.2. The cellulose I and II relative peak widths and heights were determined from Table 3.1 with respect to110 peak. The summation of the least squares approach was used to determine the optimum fitting of amorphous, CI and CII peaks. The area for each peak for different crystal forms was obtained via integration and the fraction of area

summation, by using Gaussian distribution functions as explained in chapter 3 section 3.3.2.2 Resulting from measurement of 2θ° scan shown that unprocessed Lyocell multifilament bundle contents a mixture of cellulose II (50%), cellulose I (7%) and amorphous (43%). The experimental peaks of cellulose I and cellulose II of Lyocell multifilament bundle were positioned at the same position as the Cordenka multifilament bundle peaks as shown in Chapter 3.

This method could not be used to follow dissolution, because it's difficult to follow changes in crystal structure during the dissolution process due to the Lyocell multifilament bundle having only a small amount of cellulose I and being predominantly cellulose II. For more details see the section 3.3.2.2 of the Cordenka chapter. Therefore, an alternative method is proposed to calculate the volume fraction of dissolving Lyocell multifilament (regenerated cellulose), which was to use the azimuthal α scan to follow the change of crystal orientation with time and temperature. This technique has worked successfully in ref [122] and.

4.2.2.3 The Azimuthal α Scan of Lyocell Multifilament.

The measurement of the azimuthal α scan allowed a measurement of the degree of crystalline orientation in the various samples to be determined. The X-ray technique for the azimuthal α scan was carried out from -90° to +90° at a fixed angle 2θ of 20.3°. The circumferential scan at this 2θ angle picks up both the equatorial peak reflection (α=0°) (which is actually a combination of the 110 and 200 Bragg peaks) and then the outer peaks from the 012

reflections, as described above in Figure 4.21 and shown in this ref [113]. It can be seen that the dissolution of the processed composites influenced the intensity of the crystalline reflections. Figure 4.23 shows a comparison between a typical α scan for unprocessed Lyocell multifilament bundle, and a partially dissolved composite multifilament bundle. In contrast to the 2θ scans, there is a measurable change and so the second order Legendre polynomial, P_2 , can be calculated and used to follow dissolution as shown previously for the Cordenka multifilament bundle. As the oriented crystals (associated with the unprocessed fibre) are dissolved, they reformed as randomly oriented crystals, leading to an increase of the background level and a reduction in the central oriented crystal peak.

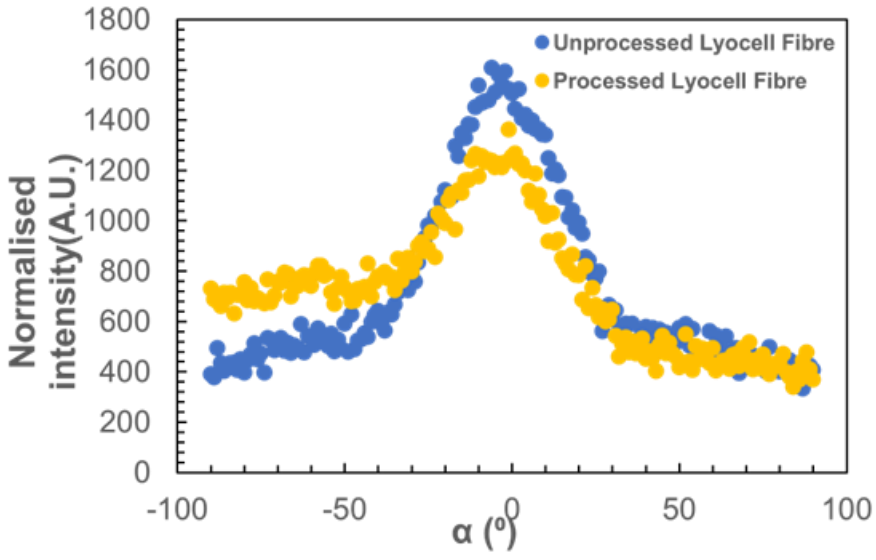

Figure 4.23: The azimuthal α scan to measure the change in orientation.

The data of the azimuthal α scan was used to calculate the overall average of P_2 for all processed multifilament bundle composite, from processing at different times and temperatures, using equation 2.4. The results of the

change in the average value of P_2 with temperature and time are shown Figure 4.24. The calculation of P_2 started from 30℃, not from 35℃ as done to calculate the coagulation fraction. This is because the P_2 can measure the overall orientation of molecules in 2D. The reduction in the average P_2 value for the processed multifilament bundle composite is due to the increase in the random molecular orientation component caused through the dissolved and coagulated matrix fraction. From Figure 4.24, the P_2 value of the processed composite fibres have reduced with an increase of time and temperature. The average values of P_2 of the processed composite fibres at various times and temperatures were gradually decreased, although with an increasing slope as the processing temperature increases. This indicates increased the effectiveness of $[C_2mim]^+$ $[OAc]^-$ to dissolve the Lyocell multifilament bundle with increasing time and temperature.

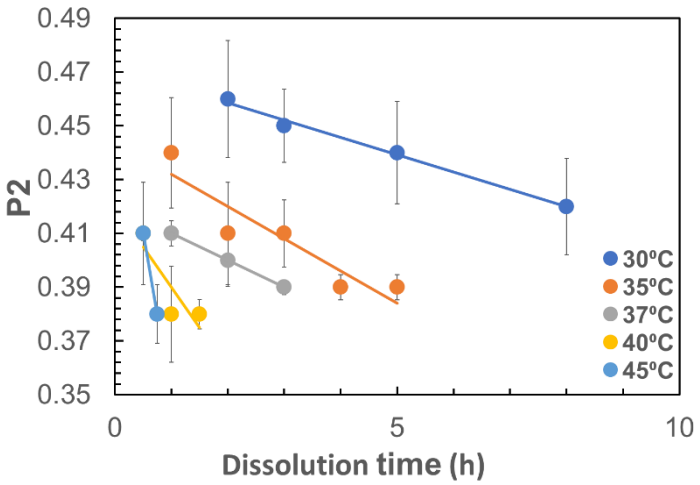

Figure 4.24: The Correlation between the average calculated P_2 and different dissolution times and temperatures for processed Lyocell multifilament bundle.

The P_2 data was formed into a master curve by using the time-temperature superposition, as previously mentioned above. The data of P_2 values plotted as function of the logarithm of time and shift factor and the different temperature curves are then superposed at 35℃ reference temperature, giving a final master curve, as shown in Figure 4.25 a. It can be noticed that the data of P_2 followed the time-temperature superposition trend and therefore, it can be used to calculate the activation energy. From the correlation between the shifted average P_2 values (at a reference temperature of 35℃) with linear dissolution time, as shown in Figure 4.25b. It was difficult to estimate the total dissolution time at P_2 = 0.25 which is the expected value for a perfectly random crystalline orientation in a 2D plane as it started completely dissolving on the PTFE frame after 45℃ at 45 mins.

The activation energy measured by using the linear relationship between the shift factors and the inverse temperature, indicating that the dissolution of the Lyocell multifilament bundle follows an Arrhenius behaviour, as shown in Figure 4.25c. The activation energy value was calculated by equation 3.2 and found equal to 199 ± 34 kJ/mol.

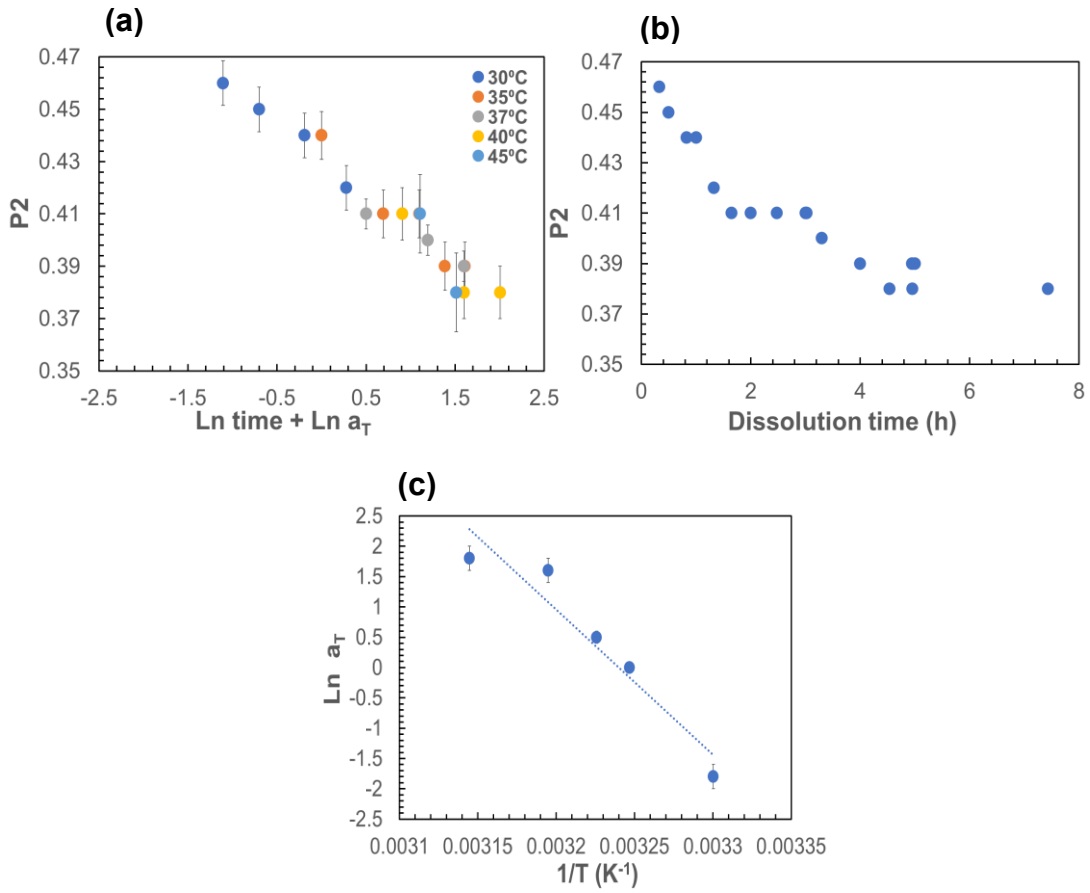

Figure 4.25: a) The final master curve of relation between P_2 and shifting time at various temperatures of Lyocell, where all the data of time and temperature shifted at reference 35℃. b) the resultant master curve between P_2 and dissolution time. c) $ln\, a_T$ plotted against the inverse of temperature, dotted line is Arrhenius equation.

4.2.3 Dissolved and Coagulated Matrix Fraction v_m from the Wide Angle of X-ray Diffraction.

By applying a rule of mixtures to the experimental data of P_2, from the azimuthal α scan measurements, the volume fraction v_m of the dissolving fraction of the original composite Lyocell multifilament bundle could then be calculated. This dissolved and coagulated fraction (v_m) now indicates the

amount of 'matrix' phase resulting in the processed composite Lyocell multifilament bundle combined with the original undissolved Lyocell multifilament bundle. This procedure was done by assuming a linear mixing rule and calculating the points between the orientation of the unprocessed Lyocell multifilament bundle with (v_m) = 0% dissolved and the completely dissolved matrix with (v_m) = 100%. By using equation 2.7, where P_{2f} is the P_2 value of the unprocessed multifilament bundle (measured as = 0.45) and P_{2m} is the P_2 assumed value of the completely dissolved matrix (film) which was measured for Cordenka with 0.25 (randomly oriented crystals).

The relationship between the calculated v_m value and the dissolution time and temperature is shown in Figure 4.26. The volume fraction of dissolved Lyocell multifilament bundle increases with increasing time and temperature.

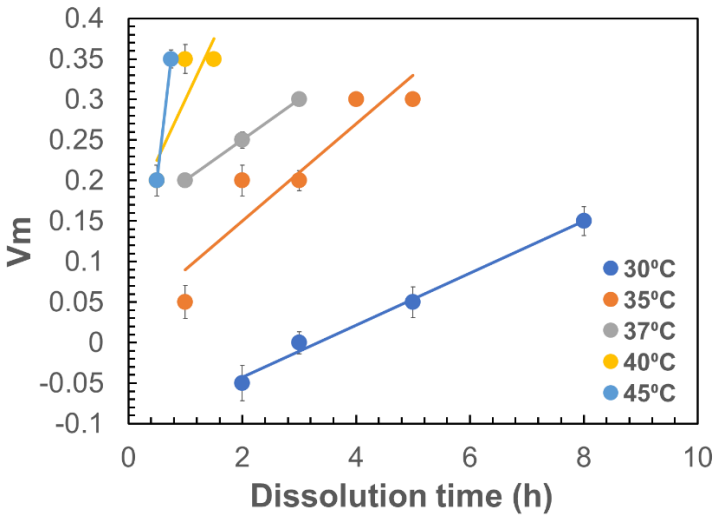

Figure 4.26: The relationship between V_m and dissolution time.

The linear master curve of both volume fraction values of azimuthal α and the C_f values of optical measurements as function of the dissolution time are shown in Figure (4.27a, b). Figure 4.27c shows a comparison of two different methods to determine the growth of the coagulation fraction with time at a reference temperature 35℃. The two techniques were the direct measurements from the optical microscopes and indirectly using P_2 measurements and the rule of mixture using equation 2.7. These two master curves plotted against each other, and it is seen that they agree quite well at early times until 3hrs and then the dissolved fraction with time from the P_2 measurements are lower. This might be due to the twisting of fibre which could affect the P_2 measurement. Or perhaps the orientation of the pure fibre changes at high temperatures and longer times (the fibres are seen to shrink at long times), making the rule of mixtures no longer valid as the optical technique will not be affected by such hypothesised effects and so is maybe more reliable at longer times (although we do not currently have any data to support this). For comparison with Cordenka multifilament bundle (in the next chapter), we will therefore use the calculation of the coagulation fraction from the direct optical micrographs.

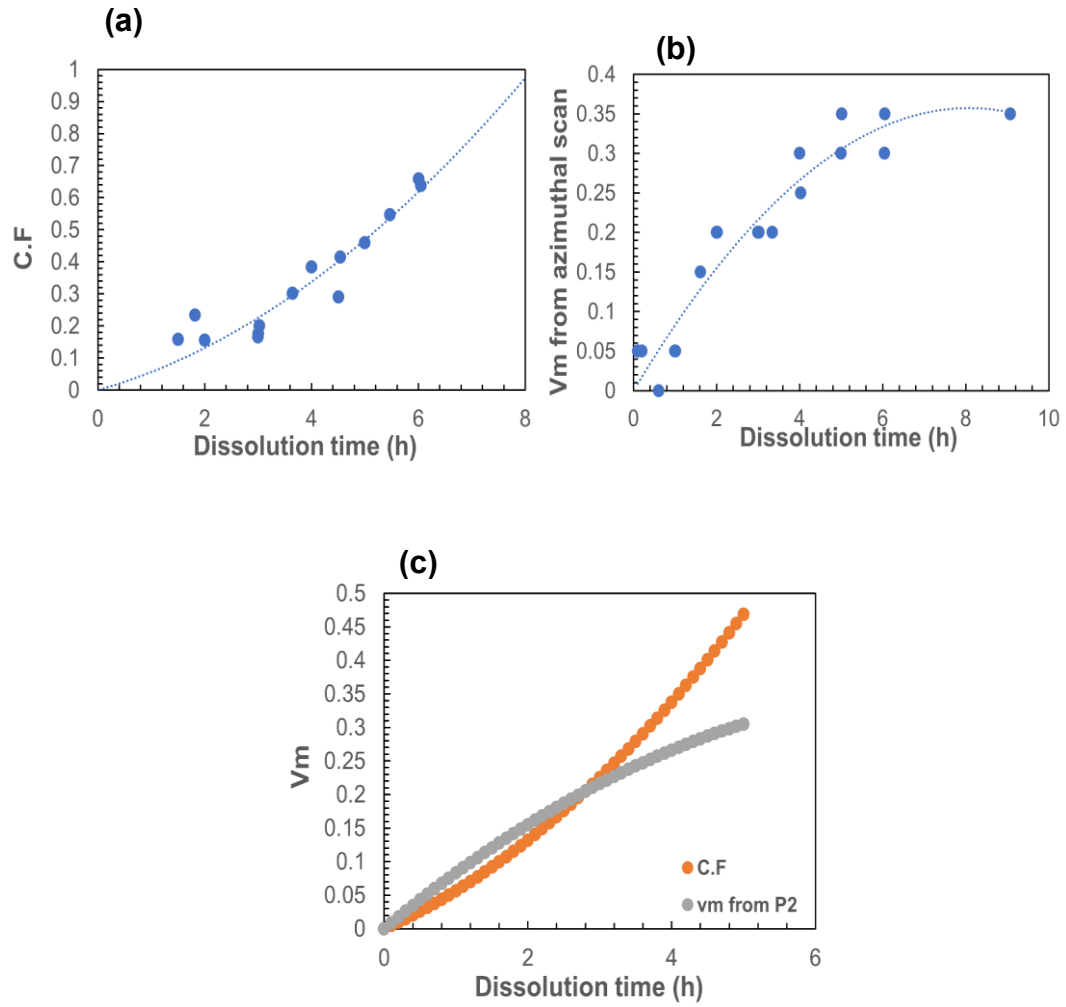

Figure 4.27: the volume fraction values of azimuthal α (a) and the C.F. values of optical measurements (b) as function of the dissolution time. The master curves of Vm of P_2 from azimuthal α scan for Cordenka and the C.F. of optical measurements for Lyocell.

4.2.4 Mechanical Measurements.

The mechanical measurements of Young's modulus and strength were found to be very useful in understanding the results presented in the previous chapter for the study of the Lyocell multifilament bundle and so have played an important role in our analysis. The tensile modulus of a composite is

dependent on the ratio between the two component fractions, that is its inner layer (fibre) and outer layer (matrix) of sample. The Young's modulus can be used to assess how much unprocessed multifilament bundle (raw material) has been converted into processed Lyocell multifilament bundle (coagulated cellulose). The mechanical strength can also potentially evaluate the dissolved fraction in the sample via calculating the amount of original Lyocell multifilament bundle on a simple rule of mixtures.

4.2.4.1 Young's Modulus.

The initial linear stress-strain region (green line) shown in Figure 4.28 indicates an elastic region. The slope of this initial stress and strain gives a Young's modulus E, which calculated from equation 2.10.

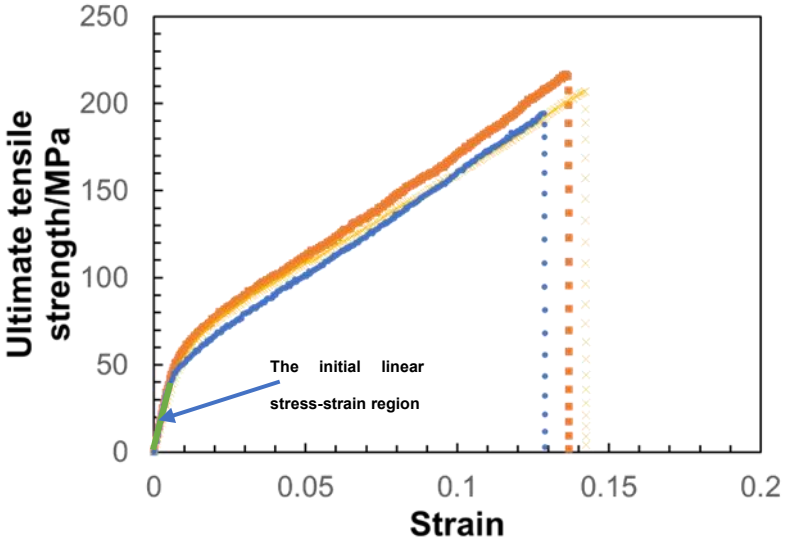

Figure 4.28: relationship between stress-strain curves of three Lyocell multifilament samples at 30℃ for 3hrs.

The measured Young's modulus of the partially dissolved composite Lyocell multifilament bundle as a function of time at various temperatures is shown in Figure 4.29. It can be seen that (as opposed to the previous Cordenka results, Chapter 3 and Figure 3.21a) there is no clear pattern of the measured Young's modulus values during an increase of time and temperatures. Therefore, the time-temperature superposition method could not be applied to this data to calculate an activation energy. It would appear that the variation in the individual measurements is larger than the changes with the increase in the matrix fraction. This variation could be caused by the matrix being brittle (potentially from a lower molecular weight), as the composite Young's modulus is very dependent on the ratio between fibre and matrix and the matrix having a higher failure strain that fibres. Another reason could be that the tightly

packed fibres (due to the twist in the Lyocell multifilament bundle) does not allow significant matrix to be produced in the interior of the multifilament bundle, leading to a variation in the adhesion between the multifilament bundle. While the modulus is very sensitive to fibre-to-fibre adhesion and the properties of the matrix, the ultimate stress (strength) is less so and so this was used as alternative method to calculate the activation energy.

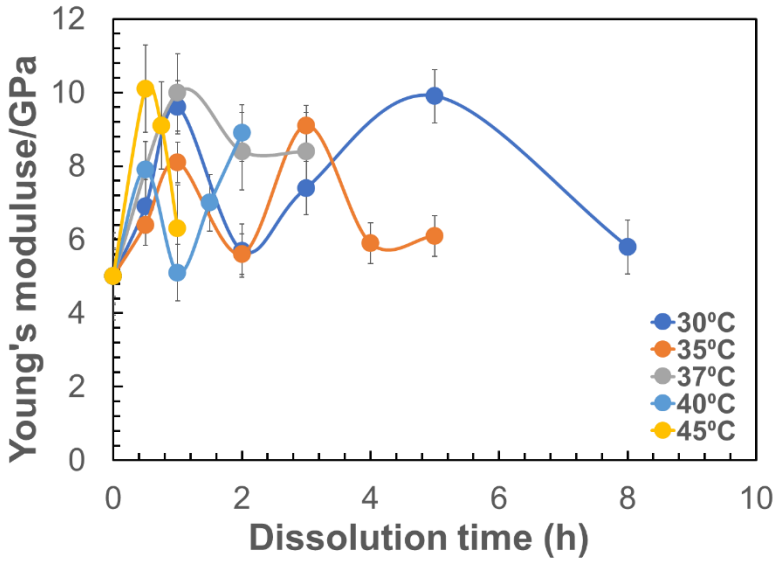

Figure 4.29: The measurements of Young's modulus at various temperature and time.

4.2.4.2 Strength Measurement.

The strength (ultimate stress) method was applied to follow changes in the composite multifilament with processing temperature and time. As the fibre strength is significantly higher than the matrix (particularly if the matrix is brittle) then this dominates the composite strength properties. The correlation between the variation of ultimate tensile strength σ_{UTS} of the Lyocell composite multifilament bundle with dissolution time at various temperatures is shown in

Figure 4.30a. The decrease of the ultimate tensile strength σ_{UTS} with an increase of time and temperature are a reflection of the dissolution of the Lyocell multifilament bundle. The data of the strength values are shifted with time and temperature, using the temperature of 35℃ as the reference temperature using the time-temperature superposition as explained above. Figure 4.30b shows the result of the final master curve after shifting the data and plotted against Ln (time).

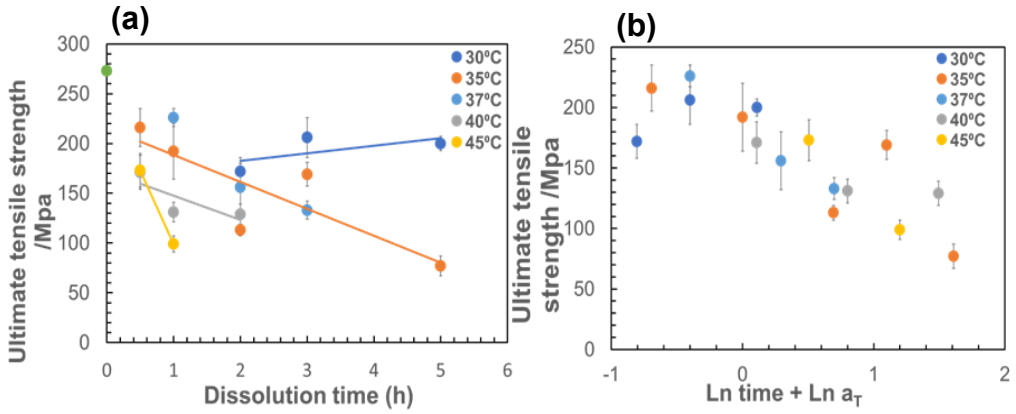

Figure 4.30: a) The measurements of ultimate tensile strength, at various temperature and time, the green point indicted to the ultimate tensile strength value of unprocessed Lyocell multifilament bundle. b) the master curve between σ and dissolution time. The

Figure 4.31 shows the variation of the predicted strength with linear time at a reference temperature of 35℃. The value of the strength of the unprocessed" Lyocell multifilament was predicted by extrapolating to zero time by utilising the correlation between the ultimate tensile strength σ_{UTS} data and the linear dissolution time. This extrapolated value of strength was taken for all times and temperatures for processed Lyocell. The data for all times and temperatures of 30℃, 35℃, 37℃, 40℃ and 45℃, was shifted by applying a

second order polynomial function to get data fitting. The best fitting gave a strength value of 237 MPa for the undissolved fibre.

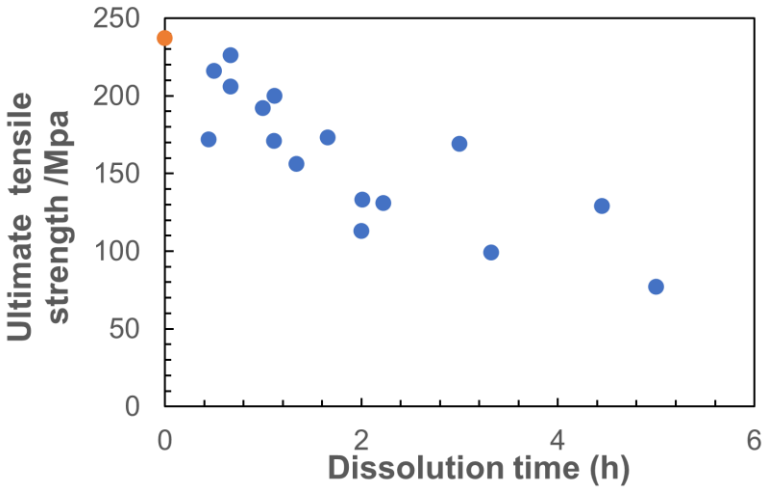

Figure 4.31: The Master curve between strength and dissolution time using TTs at 35°C as reference temperature. The orange point indicted to the ultimate tensile strength value of unprocessed Lyocell multifilament bundle.

The relationship between the shifting factors and the inverse temperature was used to measure the activation energy (as they showed a linear dependence) using the Arrhenius equation 3.2 as shown in Figure 4.32. The calculation of the activation energy gave value equal to144 ± 27 kJ/mol.

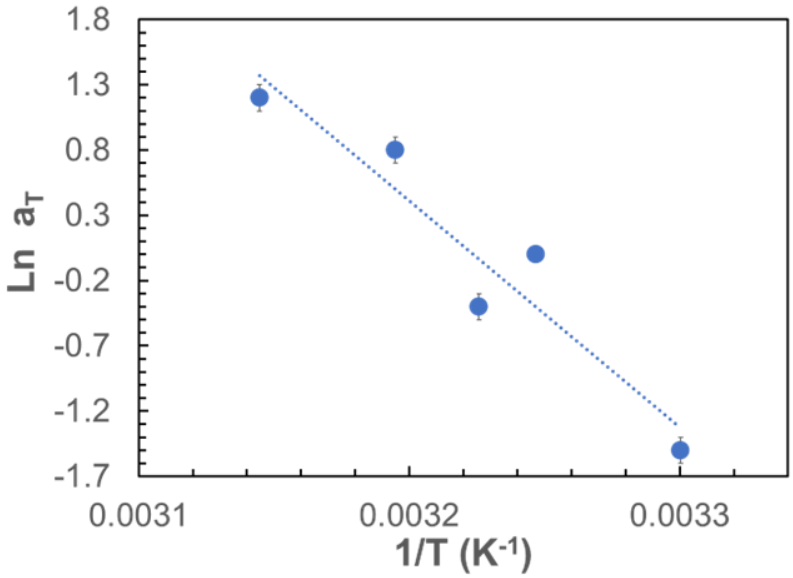

Figure 4.32: $ln\, a_T$ plotted against the inverse of temperature at 35°C as reference temperature.

The measured strength data could then be plotted with the calculated volume fraction values from the from the optical microscopy measurements. The shift factors from analysing the strength data were then applied directly to the modulus results shown in the previous section (4.3.4.2), at 35℃ as shown in Figure 4.33. As hypothesised above, it can see that the scatter in the measurements is too large compared with the scatter in the strength measurements. We could speculate that the upper values here shown as red line are the 'true' values with better adhesion between the multifilament, as also shown in Figure 4.33.

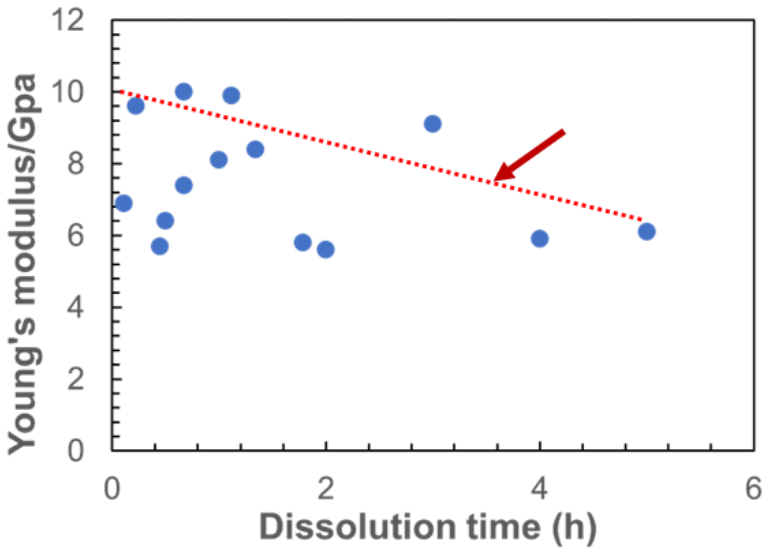

Figure 4.33: The predicted young's modulus results with dissolution time using the shift factors from the strength data at 35°C as reference temperature.

The results of plotting the measured ultimate tensile strength σ_{UTS} and the calculated, C_f (from the optical microscopy) shown in Figure 4.34, using the two mixing rules. Based on the extrapolated unprocessed Lyocell multifilament value of σ_f = 237 MPa with using $V_m = 0\%$ dissolved and the completely dissolved matrix $V_m = 100\%$, with assumed value of strength film σ_m = 24 MPa (this value of the strength assumed is the same that we measured for a completed dissolved Cordenka film). The mixing rules (upper-bound and lower-bound) are calculated by following equations 2.15 and 2.16 respectively, for measurements of strength with coagulation fraction. Although the values were found to follow time temperature superposition, the values are much lower than predicted by a parallel (Voight) rule of mixtures, unlike the Cordenka multifilament bundle. Our hypothesis is that this might be because the fibres are not bounded together with the matrix as the Lyocell multifilament bundle did not contain enough matrix. This then leads to the matrix failure before the

fibres break. Another reason could be the geometry of twist fibre influenced the force to act on all the sample, as well as the material having a lower the molecular weight. Based on these three reasons it can be concluded that it could be difficult to make all cellulose composites from twisted Lyocell multifilament bundles as the matrix phase is a key component of any composites.

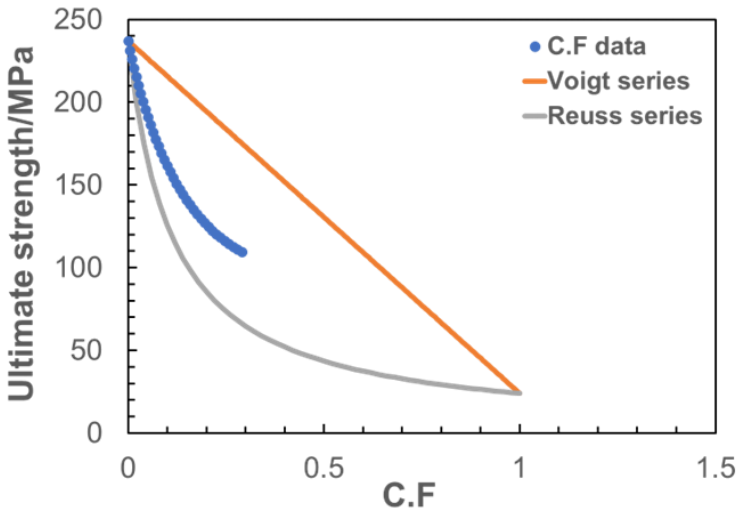

Figure 4.34: Relation between volume fraction V_m from α scan and ultimate strength with prediction of rule of mixtures, Voigt and Reuss series.

By comparing the fifth methods, the values of the activation energies of P_2 higher than the activation energy of the measured coagulated fraction, and ultimate tensile strength values. It seen that there was a much larger uncertainty in the calculation of the activation energy based on the P_2, but in close agreement. The two activation energy values within the error of inner area, coagulated fraction and strength measurement are close to each other, as shown in Table 4.2. The P_2 value is most confident value as more reliable

method compare with optical and mechanical test methods. This value quantifies the temperature dependence of dissolution, which is a useful parameter in controlling the fraction of matrix formed when creating an all-cellulose composite to obtain the optimum balance of mechanical properties.

35℃	C.F	P_2	σ	x
$E_a kJ/mol$	141 ± 16	199 ± 34	144 ± 27	127 ± 14

Table 4-2: The comparison between the values of E_{Cf} , E_σ and E_T.

4.3 Conclusion.

Optical microscopy, wide-angle X-ray diffraction and mechanical test techniques have been used in this research to follow quantitatively the physics of the dissolution, and the resulting mechanical properties of Lyocell multifilament bundle composite. The dissolution of the Lyocell multifilament bundle in the ionic liquid of 1-ethyl-3-methylimidazilum acetate [C2mim]+ [OAc]- was done at different times and temperatures. The optical microscopic method was seen to give a direct method to measure the growing area of the dissolved and coagulated Lyocell multifilament bundle with increasing time and temperature. The twisted multifilament bundle meant that the dissolved fraction formed a ring on the outside of the multifilament bundle, allowing a measurement of the decrease of the inner core and the increase in the area and thickness of the dissolved and coagulated outer ring. The dissolution was very slow at $30℃$, so we could not take any reliable results. Therefore, the

calculation of the coagulation fraction $C.F$ started from 35℃ to 45℃ with time from 0.30 mins to 5 hrs. The outer layer area (which combines both the undissolved fibres and the dissolved fraction) was found to be independent of time and temperature as dissolution proceeded, as the original multifilament bundle were replaced by dissolved and coagulated material. This results strongly suggests that density of the dissolved and coagulation fraction is very similar to the original multifilament bundle. This is not surprising as the original multifilament bundle of regenerated multifilament bundle contains no significant internal voids unlike plant fibres. For this reason, the parameter of the outer layer area could not be used to determine the dissolution activation energy. However, we could measure both the decrease of the inner core (which always contained the remaining undissolved multifilament bundle) and the increase in the area and thickness of the dissolved and coagulated outer ring.

The coagulation fraction was also calculated from optical microscopy from the ratio between the inner core (remaining fibres) and the outer layer (dissolve fraction) areas, and it was found that this increased with increasing time and temperature. All of the three measures of dissolution, that is the decreasing size of the inner core (remaining fibres), the absolute thickness of the dissolved layer and the fraction of these dissolved and coagulated fraction, were all found to follow time temperature superposition, following an Arrhenius behaviour and gave comparable values of the dissolution activation energy of ,141 ± 15 127 ± 14 kJ/mol and 141± 16 kJ/mol respectively.

A 2θ WAXS photograph was used as a qualitative measurement of the Lyocell multifilament bundle crystal structure. 2θ WAXS scans showed that the

unprocessed Lyocell multifilament bundle contains the combination of cellulose II and amorphous, with a very small amount of cellulose I.

An azimuthal α scan was employed to determine the dissolution mechanism of the Lyocell multifilament bundle by following the change in the average crystalline orientation. The azimuthal α scan at an angle 2θ=20.3° was used to follow the change in the crystal orientation with time and temperature of dissolution and hence calculate the volume fraction of the dissolved fraction. The P_2 value of the raw fibre was found to be 0.45. The measured value of P_2 for the partially dissolved composite fibres was found to decrease as time and temperature increased, indicating an increase in the random orientated crystal fraction associated with the dissolved and coagulated matrix fraction. The rule of mixtures was applied to the measured P_2 values to calculate the volume fraction v_m of Lyocell multifilament bundle dissolved, using the data from the azimuthal α scan for composite sample assuming that the orientation of the original fibres (including the twist) did not change with time and temperature.

The Young's modulus values of the Lyocell multifilament bundle composite were also measured for different processing times and temperatures. it was found that the variation in the measurements (perhaps due to the poor bonding and brittle nature of the dissolved Lyocell material) was larger than any expected underlying fall in these measurements and so could not be used for TTS measurements.

The time-temperature superposition method was applied to the experimental data of the inner area, the calculated coagulation fraction, the average P_2 values, the calculated matrix volume fraction v_m and the ultimate stress values

of the multifilament bundle composites. Each data set was transformed using time-temperature superposition to form a master curve and then the activation energy was calculated by using an Arrhenius equation (all three measured parameters followed Arrhenius behaviour). The activation energies for the four measurements of the inner core area, C_f, P_2, thickness and ultimate stress were found to be 141± 16 kJ/mol,199 ± 34 kJ/mol, 127$\pm$ 14 kJ/mol and 144 ±27 kJ/mol, respectively. P_2 is most confident method to calculate activation energy compare with optical and mechanical methods. The activation energies measured from the different methods gave similar values, which indicates they could all be used to follow the dissolution behaviour of the Lyocell multifilament bundle. By measuring the ultimate tensile strength of the unprocessed Lyocell multifilament bundle for all times and temperatures, the ultimate tensile strength of the unprocessed Lyocell multifilament bundle was measured to be σ_f = 237 MPa. Combining this with the ultimate tensile strength of a completely dissolved and coagulated film for Cordenka, allowed the ultimate stress of the composite filaments to be tested against the rules of mixture. The correlation between volume fraction from C_f measurements and the ultimate tensile strength was lower mixing rules (Voigt series). This suggest that the fibres were not bounded together with matrix and the matrix failure happened before the fibres broke.

Chapter 5 A comparison of the Dissolution Behaviour of Cordenka and Lyocell Regenerated Cellulose Multifilament Bundles in the Ionic Liquid [C2mim]+ [OAc]-

5.1 Introduction.

This chapter will examine the results presented in Chapter 3 and 4 to compare and contrast the dissolution behaviour of Cordenka and Lyocell multifilament bundles in the ionic liquid [C2mim]+ [OAc]-. All the previous analysis results described in the previous two chapters are used to assess the dissolution behaviour, including optical microscopy (OM), wide angle X-ray diffraction (WAXS) and mechanical measurements, along with molecular weight and molecular distribution analysis carried out externally by the group of Professor Antje Potthast, University of Natural Resources and Life Sciences, Vienna, (BOKU)

By studying the dissolution behaviour via several different factors, a picture of what controls dissolution behaviour and the dissolution activation energy is presented allowing the most important factors to be identified. Those factors discussed include the growth of the volume fraction and thickness of the dissolved fraction with time (the coagulation fraction), the decrease in the orientation of the partially dissolved composites (via the measurement of the average orientation factor $P2$), the geometry of the multifilament bundles (untwisted or twisted), the Young's modulus and ultimate stress, the calculated activation energy and finally the molecular weight.

5.2 Results and Discussion.

5.2.1 Optical microscopy.

Optical microscopy pictures (Figure 5.1) give a first explanation for the difference of the dissolution behaviour between the Cordenka multifilament bundle and the Lyocell fibre bundle. It is seen that the Cordenka multifilament bundle is untwisted and Lyocell multifilament bundle is twisted, as shown in Figure 5.1(a, b). We will show more about the effect of this geometry factor on the dissolution behaviour later in this chapter. To compare these two multifilament bundles of Cordenka and Lyocell, the bundle width measurement was done using Image J software. It was found that the width of unprocessed Cordenka was 1.00 ± 0.01 mm which is much larger than the unprocessed Lyocell multifilament which was 0.19 ± 0.01mm. The uncertainty for these two measurements was calculating by doing 10 measurements along the bundle and then calculating a standard error ($\frac{\sigma}{\sqrt{10}}$).

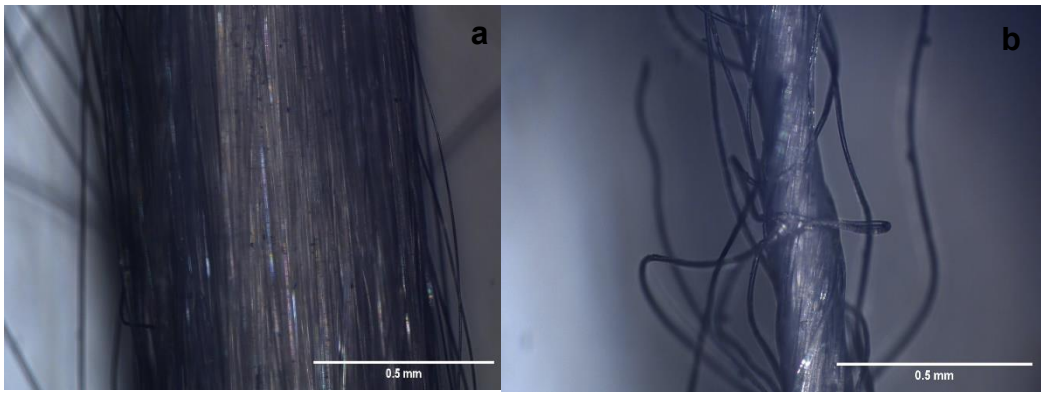

Figure 5.1: The geometry from the optical microscopy for the Cordenka filament bundle (a) and the Lyocell fibre bundle (b).

The cross-sectional area (as measured by the mass per unit length and the density of cellulose) is a further factor of difference between the unprocessed Cordenka multifilament and the unprocessed Lyocell multifilament bundles. The result, as shown in Table 5.1, indicates that the Cordenka multifilament bundles was approximately 10 times larger than the Lyocell multifilament bundles, as shown in Table 1. This is confirmed qualitatively from the optical pictures shown in both Figures 5.1 and 5.2. The cross-section area (m^2) of each processed composite was determined using a gravimetric technique in conjunction with the density of cellulose by equation:

$$A = \frac{m}{l\,\rho} \tag{5.1}$$

where *l* is the length of fibre in meter (100 mm lengths were used) and ρ is the density of cellulose, which has been recorded as 1.4 mg/mm^3 [98, 99], and *m* is the mass of the fibre in kg.

Samples	Average mass /mg	Average Length /mm	Mass per unit length (mg)/L(mm)	A Total effective area / mm^2
Cordenka multifilament	25.0 ± 0.3	98 ± 2	0.25± 0.01	0.18 ±0.01
Lyocell multifilament	2.80± 0.1	98 ± 2	0.028± 0.001	0.020 ±0.001

Table 5-1: The mass per unit length measurements.

The microscopy cross-sections of an unprocessed Cordenka multifilament bundle and an unprocessed Lyocell multifilament bundle are shown in Figure 5.2. The unprocessed Cordenka multifilament bundle has a few hundred individual filaments which appear as a loose structure with significant inner spaces in between. In comparison, the cross- section of the unprocessed Lyocell fibre bundle is comprised of a few hundred of individual filaments which are close to each other without significant inner spaces. As a reminder, these cross-section images are prepared by encapsulating in epoxy resin. The untwisted Cordenka multifilament bundle will separate when surrounded by the epoxy resin and so separate significantly as shown in Figure 5.2a. In comparison, the twisted Lyocell multifilament bundle does not separate as shown in Figure 5.2b. It could be expected that something similar may happen when each multifilament bundle is immersed in the ionic liquid, allowing easier passage to the interior of the bundle for the Cordenka multifilament while making it more difficult (if not impossible) for the ionic liquid to reach the interior of the Lyocell bundle.

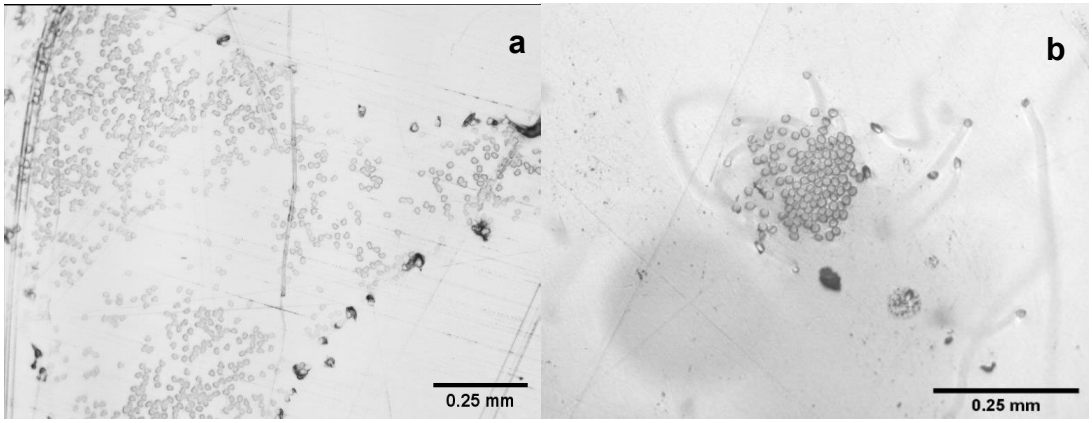

Figure 5.2: Typical Microscopy cross-sectional images of the unprocessed Cordenka filament bundle (a) and the unprocessed Lyocell fibre bundle at 20 times magnification. Both are encapsulated into epoxy resin.

Figure 5.3 shows a comparison of the two composite multifilament bundles processed for the same time and temperature, at 30℃ for 1hr. it can be seen that the small amount of dissolution is enough to bind the Cordenka multifilament bundle together and therefore it no longer spread in the epoxy.

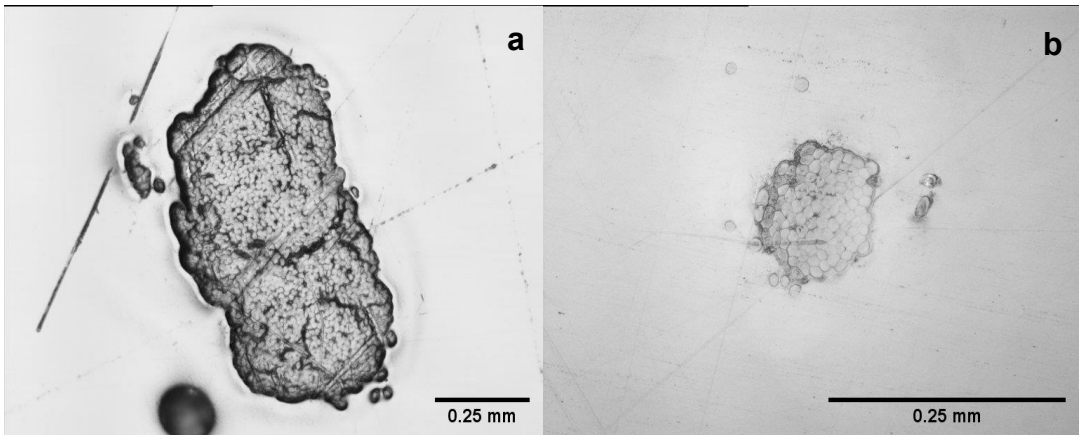

Figure 5.3: Microscopy cross-sectional images of partially dissolved fibres at the beginning of dissolution at the same temperature and time (30°C and 1 hour) (a) Cordenka multifilament bundle at 10 times magnification (b) and the unprocessed Lyocell fibre bundle at 20 times magnification.

Figures 5.4 and 5.5 shows optical micrographs of the two partially dissolved processed composite multifilament bundle, processed at a higher temperature of 45°C for 1 hour. In this work we follow the complete dissolution of each individual multifilament, which this contributes to the overall dissolution of the multifilament bundle forming a dissolved and coagulated matrix fraction. For the Cordenka untwisted multifilament bundle, the ionic liquid is able to penetrate into the interior of the bundle and so first fills the inner spaces between the individual multifilament bundles. Once all the gaps between the individual multifilaments are filled, then an outer layer of matrix is then seen as a ring of dissolved and coagulated matrix, as shown in Figure 5.4. However, it can be seen that there are also a few fibres in this outer 'matrix' region and so the matrix fraction cannot be determined optically. Instead, this was done by determining the average composite orientation ($P2$ measurements) which has a contribution from the undissolved filaments (which retain the original crystal orientation) and the dissolved and coagulated matrix fraction where the crystals are now randomly oriented.

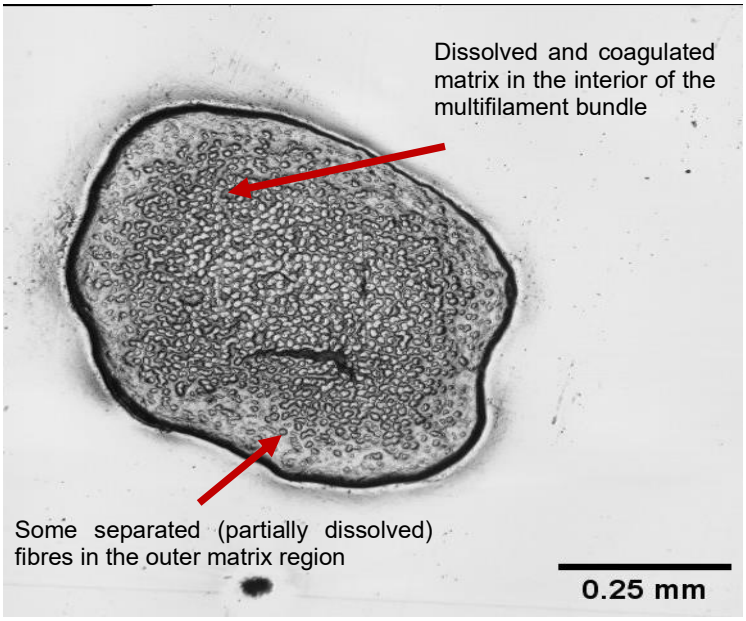

Figure 5.4: Microscopy cross-sectional images of the Cordenka filament bundle at 10 times magnification during the dissolution process at 45 ℃ for 1hr at 20 times magnification.

For the partially dissolved twisted Lyocell multifilament bundle, the structure (Figure 5.5) is different, with a more significant outer matrix layer of dissolved and coagulated cellulose around the remaining inner core area (of undissolved fibres). As the dissolution proceeds, the inner core of undissolved fibres decreases in size while the outer ring of ‘matrix’ increases linear with time. As we have seen, the total average outer area remains the same with the dissolved and coagulated matrix layer replacing the original Lyocell multifilament bundle.

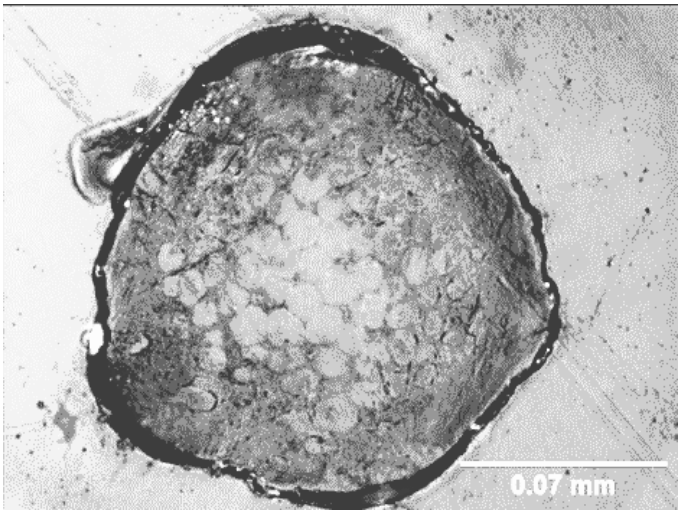

Figure 5.5: Microscopy cross-sectional images of the processed Lyocell fibre bundle during the dissolution process at 45℃ for 1hr at 50 times magnification.

This also suggests that the density of the dissolved and coagulated material is the same as the original fibres. The result is a close packing fibre microstructure, as shown in Figure 5, here processed at 45℃ for 1hr. Figure 5.5 also shows that there is no detached multifilament in the outer 'matrix' region and so an optical technique can be used to determine the growth of the matrix layer with temperature and time.

From the calculation of the dissolution fraction, at the same temperature 45℃ and time 1hr, for the Cordenka and Lyocell partially dissolved composite multifilament bundle, it was found that the dissolution fraction of the Cordenka multifilament bundle was 60 % from the P_2 orientation measurements, while the dissolution fraction of the Lyocell composite was 45% directly from the optical microscopy measurements. Our hypothesis is that it is more difficult for the ionic liquid [C2mim]+ [OAc]- to penetrate the twisted Lyocell multifilament bundle and so the dissolution can only proceed by dissolving the outer fibres

creating the outer matrix ring. For the untwisted Cordenka multifilament bundle, they can swell in the ionic liquid (as also seen in Figure 5.3 with the epoxy resin), and so dissolution proceeds more rapidly, at least initially until the interior of the bundle is filled with spread cellulose gel. The lower dissolution fraction of the Lyocell multifilament bundle, at the same processing temperature and time, confirmed the effect of twisting fibre during the dissolution. This comparison of the difference in the speed of dissolution will be shown in more quantitative detail later in this chapter.

Figure 5.6 further compares the interior of the two partially dissolved multifilament bundle (processing temperature of 45℃ for 1 hour) and shows how the matrix is located in each processed multifilament bundle. In the interior of the Cordenka multifilament bundle (Figure 5.6a and b) each individual multifilament is surrounded by a layer of dissolved and coagulated matrix, which we suggest is due to the easier penetration of the IL [C2mim]+ [OAc]- and we would further suggest that this will ultimately lead to excellent compatibility between the two phases, and the bundles will act as a good composite. In comparison the Lyocell sample shows that the multifilament bundle is aggregated in the inner core area due, we believe, to the difficulty of the IL [C2mim]+ [OAc]- to penetrate into the twisted bundle. This leads to the formation of the outer matrix ring, as shown in Figure 5.6c, which makes the dissolution process easier to follow optically. However, we might expect that the fibres in the interior of the Lyocell multifilament bundle are not so well bonded together, resulting in a less than optimum final composite, as will be confirmed by the later presented mechanical measurements.

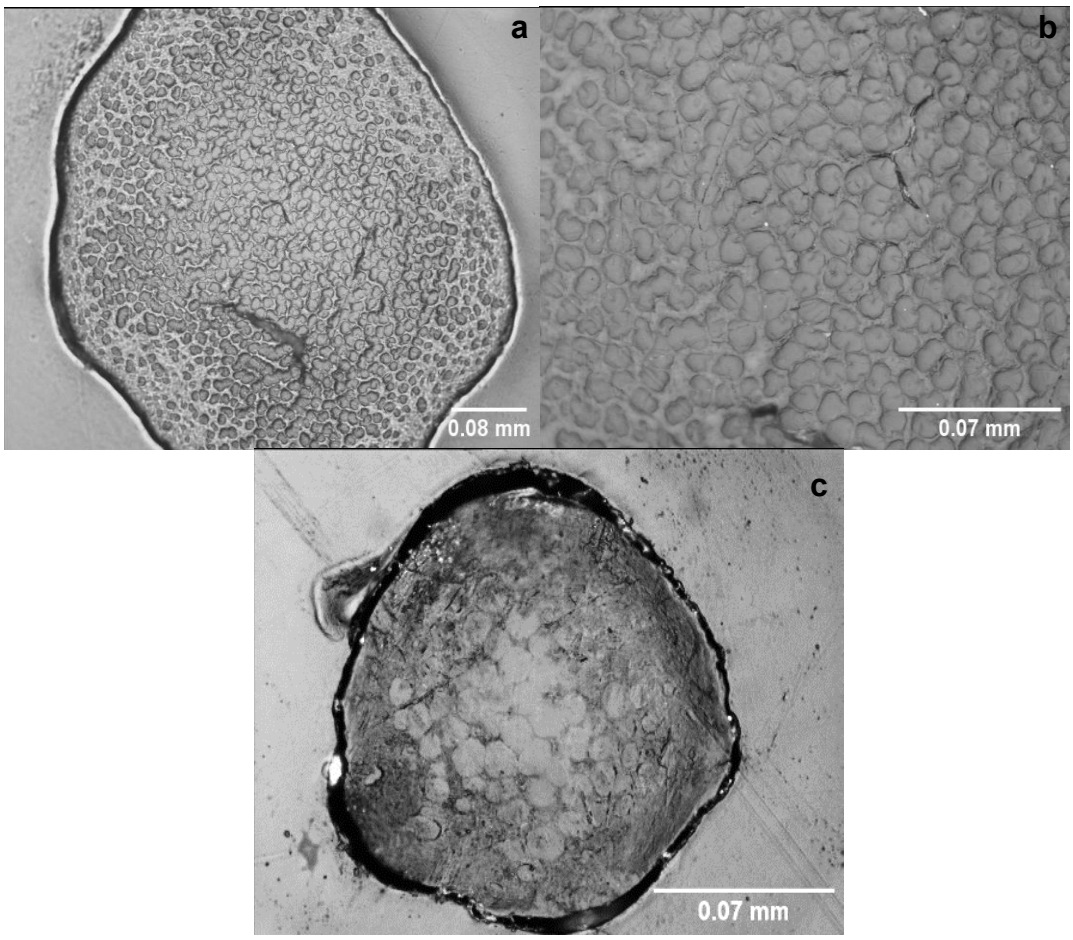

Figure 5.6: a) The cross- section image of interior of Cordenka multifilament at 20 times magnification. b) The cross- section image of interior of Cordenka multifilament at 50 times magnification and c) The cross- section image of interior of Lyocell multifilament at 50 times magnification.

5.2.2 Wide Angle X-ray Diffraction.

5.2.2.1 Two-Dimension of X-ray Diffraction Pattern.

The results of a 2D X-ray image showing the positions and reflection peaks for the Cordenka multifilament bundle and the Lyocell multifilament bundle are given in Figure 5.7. In general, the crystal structure of the two fibres is very

similar. In line scans, for Cellulose II the equatorial Bragg peak reflections of 110 and 200 are often combined into a single large peak around 20°, although in these photographs they can be seen to be resolved. These Bragg peaks indicate a crystal structure that is predominantly Cellulose II. However there is some evidence, which was completely unexpected (from reflections at locations the 14.8° and 16.5° peaks) of the presence of a small remaining fraction of Cellulose I ($1\bar{1}0$,110) Bragg peaks, respectively, for the Cordenka multifilament and Lyocell multifilament bundles, as shown in Figure 5.7 (a,b). Both materials therefore have a mixture of predominantly cellulose II and surprisingly a small amount of cellulose I, perhaps left from the original pulp source which is not completely dissolved in both manufacturing processes.

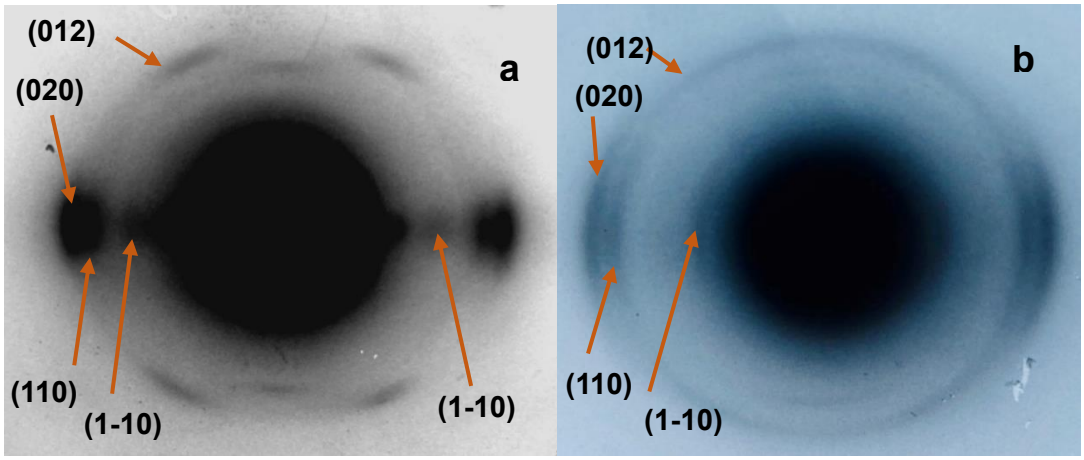

Figure 5.7: a) 2D x-ray scattering pattern from unprocessed Cordenka multifilament showing the Bragg peaks and b) 2D x-ray scattering pattern from unprocessed Lyocell multifilament showing the Bragg peaks.

The yellow lines on Figure 5.8 (a, b) show for the eye the difference in the Full width half maximum (FWHM) of the main Bragg peaks for both multifilament bundles. These were measured using a protractor from the photographs as 20 ± 1° for the Cordenka multifilament bundle and 45 ± 1° for the Lyocell multifilament bundle. This indicated qualitatively that the overall crystal orientation of the Lyocell bundle is significantly lower than the Cordenka multifilament bundle, which is to be expected due the large twist shown in Figure 5.1. This will now be quantitatively compared using the WAXS x-ray circumferential measurements. From these measurements we are not able to comment on the comparative orientation of the 'individual' Cordenka and Lyocell multifilament bundle.

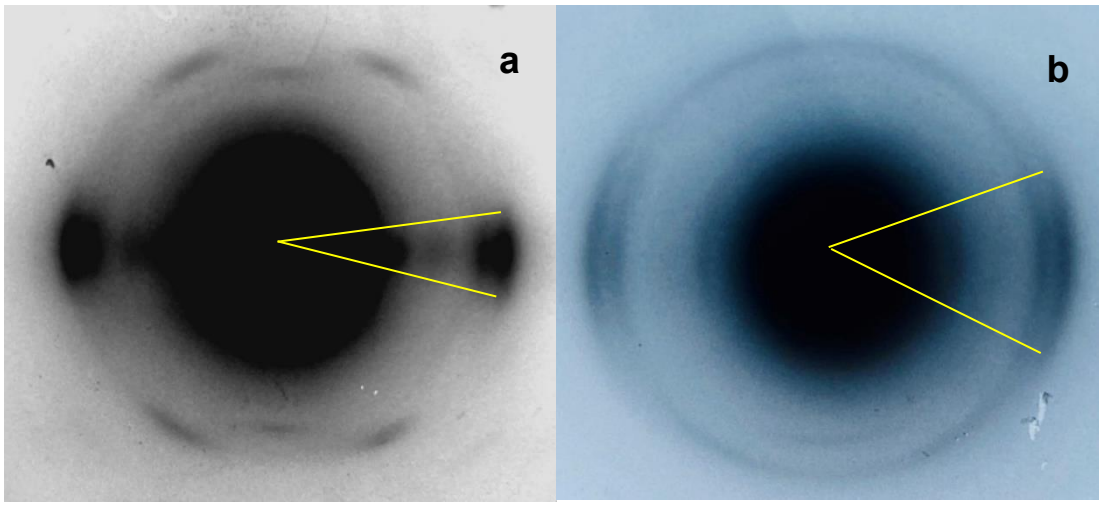

Figure 5.8: a) 2D x-ray scattering pattern from unprocessed Cordenka multifilament showing the width of FWHDM and b) 2D x-ray scattering pattern from unprocessed Lyocell multifilament showing the width of FWHDM.

There are other Bragg reflection peaks from the crystalline structure which appear in cellulose, which is due to the 012 planes in the Cordenka multifilament and Lyocell multifilament bundles. These four peaks are shown in Figure 5.9 and can be seen to have a similar angular spread as the equational peaks, as they come from the same crystal structure. These peaks are stronger in the Cordenka multifilament bundle due to the fibres being untwisted so we only show the Cordenka picture.

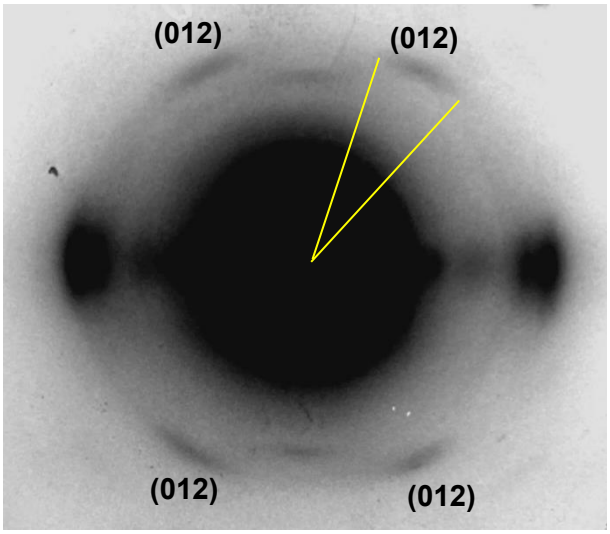

Figure 5.9: The four Bragg reflection peaks at 012 planes for Cordenka.

This 012-reflection plane has a very similar value of 2θ to the chosen equatorial position with maximum signal intensity (20.3°), and so this reflection appeared in a circumferential α scan ~+/-90° (as seen in Figure 11a). Figure 5.10(a,b) shows the path of the circumferential scans that were carried out for both multifilament bundle (α ± 90°) at a fixed value of 2θ of 20.3°, which was the position of maximum intensity on the equator (α = 0°) from a 1D line scan.

As discussed above, this is a convolution of the 110 and 200 Bragg peaks that are not resolved in the line scans with our WAXS equipment.

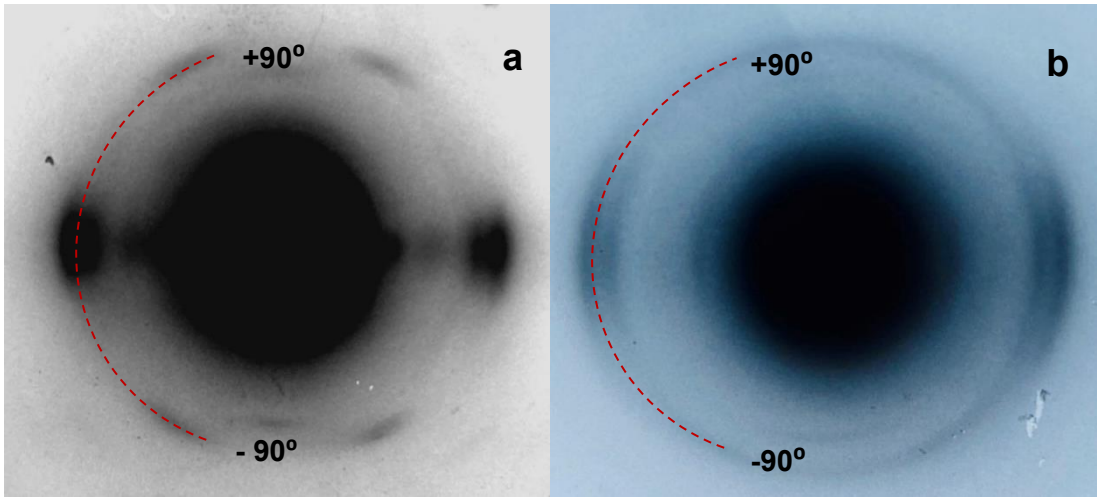

Figure 5.10: : a) 2D x-ray scattering pattern from unprocessed Cordenka multifilament showing the α Circumferential scan setting in two dimensions (2D) from -90° to 90° (red dashed line) at 2θ = 20.3° and how this includes the 012 reflection. b) 2D X-ray scattering pattern from unprocessed Lyocell multifilament showing the α circumferential scan setting in two dimensions (2D) from -90° to 90° (red dashed line) at 2θ = 20.3° and how this includes the 012 reflection.

5.2.2.2 The Azimuthal α Scan of Cordenka and Lyocell Multifilament Bundles.

The result of the azimuthal α scan measurements for the two multifilament bundles associated with the result from the 2D image, are shown in Figure 5.11 a, b. These results reflect those of the 2D pictures (e.g., Figure 8) with a much wider FWHM for the original Lyocell multifilament bundle.

The sharp small outer peaks of the unprocessed Cordenka multifilament bundle of the 012 reflection at a circumferential angle of ~+/-60°, can clearly be seen as shown in Figure 5.11a. In comparison, for the unprocessed Lyocell multifilament bundle the wider peaks appeared at 012 of Lyocell multifilament bundle were not so evident, as shown in Figure 5.11b. It can also be seen that the Full Width Half maximum angular spread for the 012 peaks, is similar to the 200 central peak as discussed qualitatively in Figures 5.8 and 5.9. The FWHM for unprocessed Cordenka multifilament bundle for the 012 peaks was measured to be $18.7^{\circ} \pm 1.3^{\circ}$ (calculated as shown schematically in Figure 5.13.

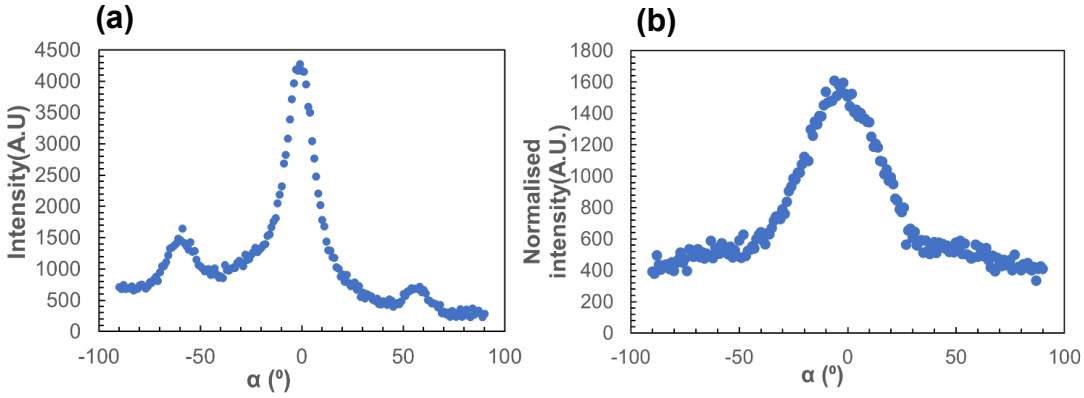

Figure 5.11: The azimuthal α scan for unprocessed Cordenka multifilament and b) for unprocessed Lyocell multifilament.

Figure 5.12 further shows a direct comparison of the (normalised) measured azimuthal α scan profiles for the unprocessed and processed multifilament bundles showing clearly the difference in FWHM, which we attribute mainly to the twist in the Lyocell multifilament bundle.

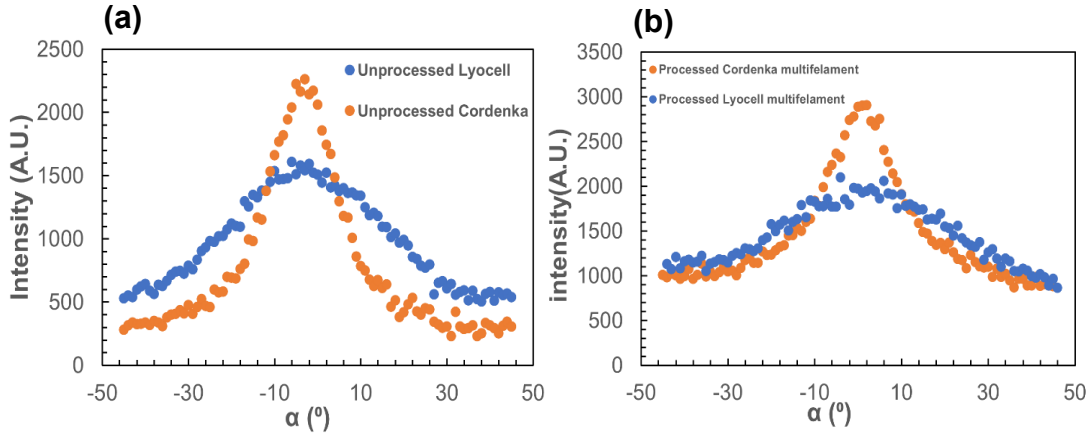

Figure 5.12: a) The azimuthal α scan for unprocessed Cordenka multifilament and Lyocell multifilament and b) The azimuthal α scan for processed Cordenka multifilament and Lyocell multifilament.

Our hypothesis to estimate the angle of twisting of the unprocessed or processed Lyocell multifilament bundle, is to determine the difference between the full width half maximum (FWHM) for the Cordenka multifilament (untwisted) and Lyocell (twisted) multifilament bundles as showed in Figure 5.13, and then use equation 5.2. We are making the assumption here that the underlying orientation of the two individual filaments is similar.

The data of azimuthal α scan in 2D from $-45°$ to $+45°$, as shown in Figure 5.12 a,b, utilised the values of FWHM for unprocessed Cordenka multifilament and Lyocell multifilament bundles were $20.0° \pm 0.3$ and $40.0° \pm 0.8$ respectively, using equation (5.2)

$$\textbf{\textit{The angle of twisting}} = \frac{\textbf{\textit{the FWHM of Cordenka filament}} - \textbf{\textit{the FWHM of Lyocell bundle fibre}}}{2} \quad (5.2)$$

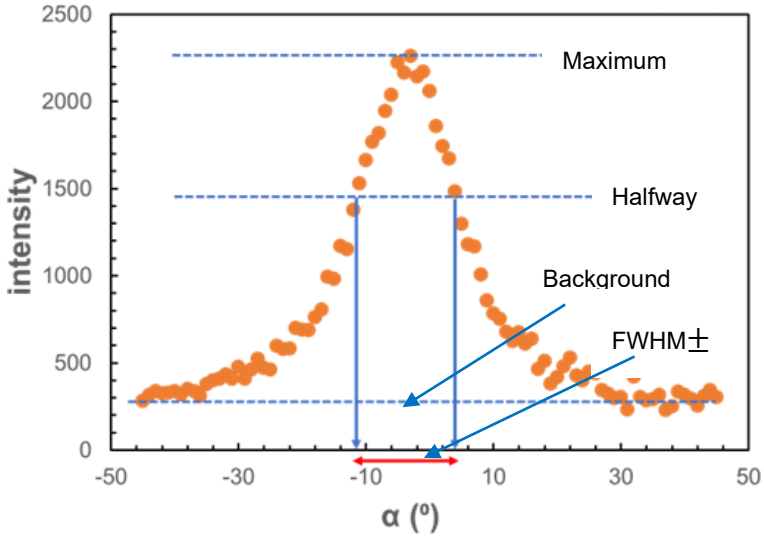

Figure 5.13: Schematic picture shown haw the Full width half Maximum measured using the data of azimuthal α scan for unprocessed Cordenka multifilament.

The angle of twisting of the unprocessed Lyocell multifilament bundle was then calculated to be $\pm 10°$. The same equation was used to calculate the angle of twisting of the processed Lyocell bundle fibre by using FWHM values and the processed Cordenka multifilament bundle which were $43° \pm 2$ and $21° \pm 0.5$ respectively. This gave a calculation of the twist angle of processed Lyocell sample equal to be $\pm 11°$ from equation 5.2 These values of FWHM for unprocessed Cordenka and Lyocell multifilament bundles are similar to the FWHM measurements results which were calculated earlier from the 2D image.

For comparison the angle of twisting of unprocessed Lyocell multifilament bundle measured directly from an optical microscopy using image J software and found to be $\pm 16.2 \pm 0.6°$, as shown in Figure 5.14 from 7 measurements.

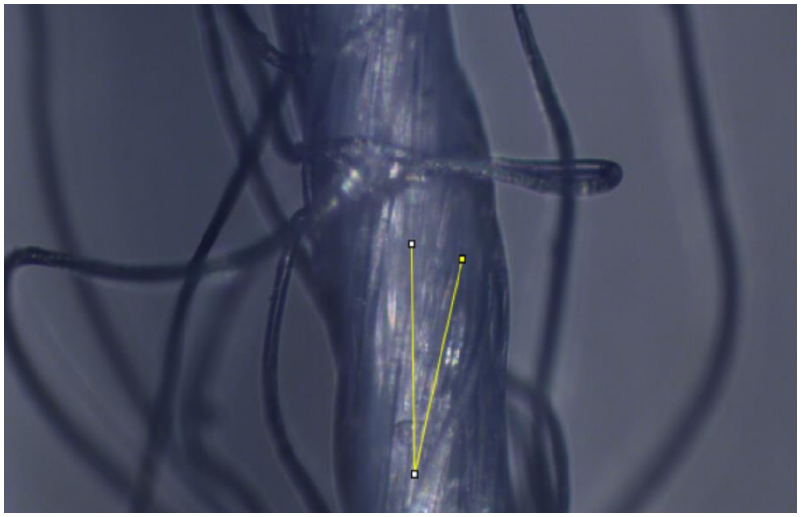

Figure 5.14: Twest angle measurments using Image j.

It can be concluded that the difference between the peaks of Cordenka multifilament and Lyocell multifilament bundles is $\pm 10°$. The initial twist angle $\pm\, 16.2 \pm 0.6°$ of the unprocessed Lyocell multifilament bundle explained the wider peak with lower orientation of Lyocell multifilament bundle.

5.3 Comparison the Molecular Weight Between unprocessed Cordenka Multifilament and Lyocell Multifilament Bundles.

Table 5.2 shows the weight-average molecular weight (M_w), number-average molecular weight (M_n) of unprocessed Cordenka multifilament and unprocessed Lyocell multifilament bundles. These values were measured by Prof. Antje Potthast, University of Natural Resources and Life Science, Vienna, Austria.

The value for Cordenka was found to be larger compared to the Lyocell multifilament bundle measurements as shown in Table 5.2. One hypothesis is that this difference could be as a result that the Lyocell multifilament bundle might be bleached. As a reminder, the Lyocell multifilament bundles were taken from a woven cloth (hence both the bundle twist is required for the weaving process and also possible bleaching to give a white cloth). This bleaching process can significantly reduce the number-average of molecular weight of multifilament and then lower the dissolution activation energy. The activation energy values for the Cordenka multifilament and Lyocell multifilament bundles were calculated using the most appropriate (and hence different) methods as shown in Table 5.2.

Methods at 35℃	**Cordenka multifilament bundle** $E_a kJ/mol$	**Lyocell multifilament bundle** $E_a kJ/mol$
C.F	_	141 ±16
P_2	199 ±34	151 ±3
σ_{UTS}	144± 27	158± 40
x	_	127± 14
E	198 ±29	_
M_n / kDa	61± 2	42±1. 2
M_w / kDa	169 ± 13	150 ± 13

Table 5-2: The activation energy for Cordenka multifilament and Lyocell multifilament from different methods that used at reference temperature of 35℃**.** Where C.F is

coagulation fraction, σ_{UTS} is the ultimate tensile strength, E is Young's modulus and X is the thickness.

5.4 Comparison of the Dissolution Speed of the Cordenka and Lyocell Multifilament Bundles.

Figure 5.15 compares the master curves (frome the data) at reference temperature of 30℃ for the two materials from the WAXS circumferential P_2 measurements. It can be seen the starting P_2 is different for the two multifilament bundles, which we have shown in the previous section is due to the twist of the Lyocell multifilament bundles. Although the starting P_2 is significantly different, our hypothesis is that as long as this starting value changes with time and temperature in a systematic way, then time temperature superposition can be used to calculate the activation energy. Table 5.3 compares the two measurements of activation energy using TTS determined in this way from these orientation measurements.

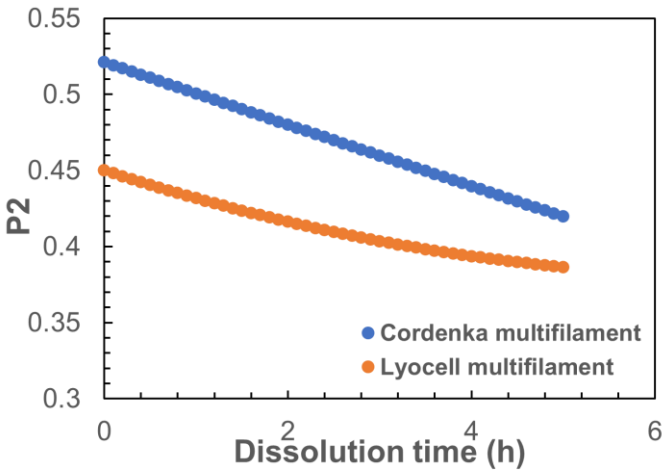

Figure 5.15: comparison between Cordenka and Lyocell multifilament using P_2 data at reference temperature 30 ℃ .

To compare the increase in the matrix volume fraction, v_m. with time, for the two-multifilament bundles, the data for each material was taken from the best method, which was different for the two materials. For the Cordenka multifilament bundle this was from the azimuthal α scan, P_2 measurement, as the optical measurement was not possible due the images discussed earlier (Figure 5.4 and 5.5). The best method found to calculate the volume fraction of the Lyocell multifilament bundle was the coagulation fraction C.F from direct optical measurements. This was because the the twisting of the Lyocell multifilament bundles lowered the starting value of P_2 measurement, and so made this less accurate. So average orientation measurements (P_2) for the untwisted Cordenka multifilament bundle and a direct optical method for the twisted Lyocell fibre bundles were used to calculate the growth of the matrix volume fraction with time and temperature.

The data of the volume fraction from the azimuthal α scan, P_2, of the Cordenka multifilament bundle was therefore used to calculate the dissolution speed

using a rule of mixtures as described in Chapter 2 and equation 2.7. By applying a polynomial function of the dissolution time as a guide around this preliminary data of Cordenka multifilament bundle, the master curve at a temperature of 35°C was calculated as shown in Figure 5.16a. The same procedure was used to calculate the dissolution speed of the Lyocell multifilament bundle, using the V_m data from the optical measurement as shown in Figure 5.16b for the same reference temperature.

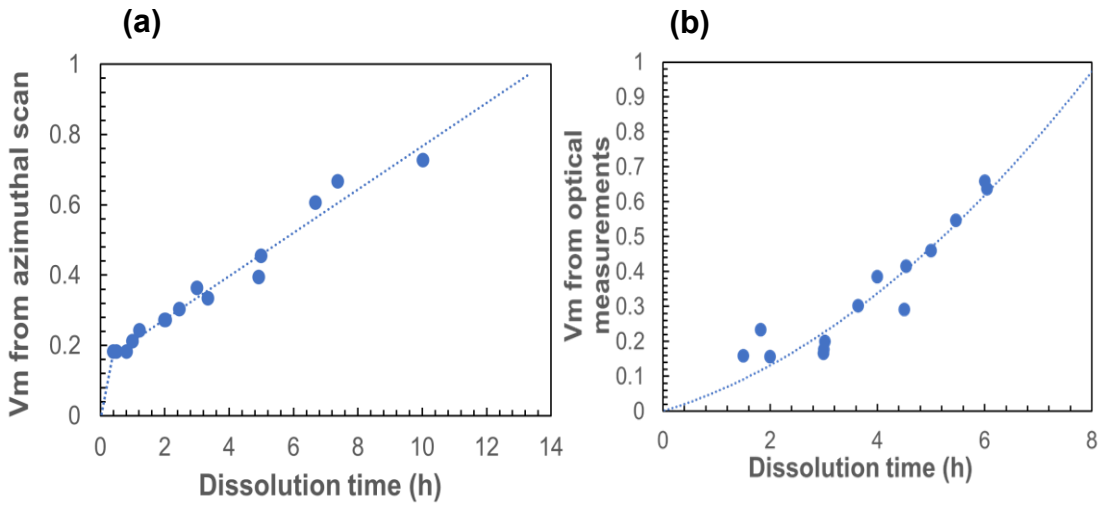

Figure 5.16: a) the resultant master curve between V_m from azimuthal α scan measurements and dissolution time for Cordenka multifilament and b) the resultant master curve between V_m and dissolution time from optical measurements for Lyocell multifilament.

By comparing between V_m from the P_2 measurement and V_m from optical measurement of the Lyocell multifilament bundle, it found that the best agreement of data was during the first 3hrs, as discussed before in the Lyocell chapter and shown again in Figure 5.17.

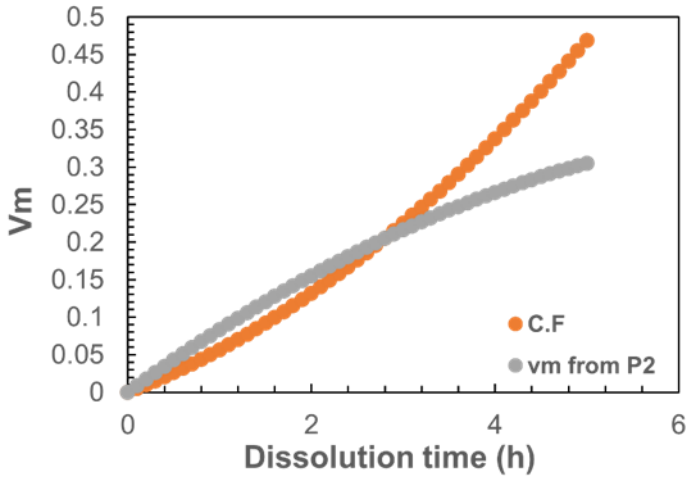

Figure 5.17: The volume fraction values of azimuthal α (a) and the C.F values of optical measurements (b) as function of the dissolution time of the Lyocell multifilament bundle. The master curves of Vm of P_2 from azimuthal α scan and the C.F of optical measurements of the Lyocell multifilament bundle.

Based on this result, the data of the Cordenka multifilament bundle was taken from zero to 3hrs to measure and compare the dissolution speed with the Lyocell multifilament bundle and the comparison is shown in Figure 5.18. Resulting from that it was found that the dissolution speed of the Cordenka multifilament bundle was faster initially than the Lyocell multifilament bundle, as shown Figure 5.18. Our hypothesis is that this is due to the easier penetration of the IL into the untwisted Cordenka multifilament bundle and shows clearly that the geometry of the multifilament bundle can have a significant effect of the speed of dissolution.

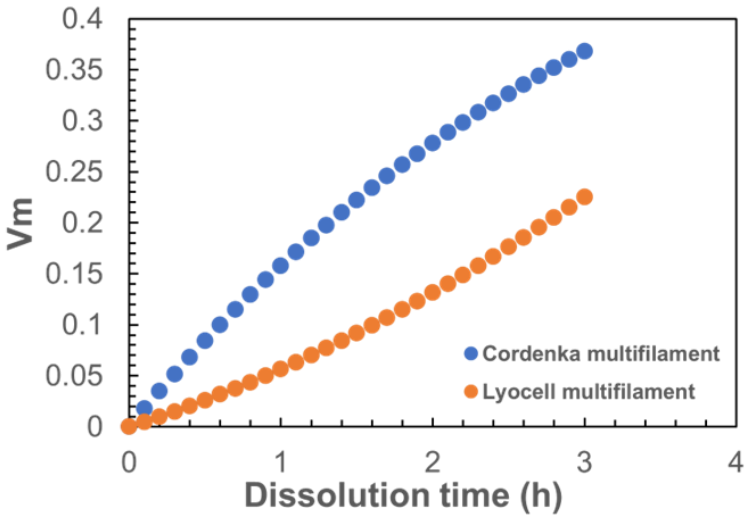

Figure 5.18: Comparison of the dissolution speed between Cordenka and Lyocell multifilament using the relationship between volume fraction and dissolution time from azimuthal α scan and optical measurements. This for dissolution times up to 3hrs as we are less confident in the lyocell data at longer time as shown above.

There is another difference between the Cordenka and Lyocell materials such as a higher activation energy and a higher molecular weight as shown in Table 5.3. We proposed earlier in this chapter that these could be linked. Although the Lyocell multifilament bundle has a lower molecular weight, however, we believe that the main reason to slow down the dissolution speed is the bundle geometry. Table 5.3 shows a final summary of the difference factors between the Cordenka and Lyocell multifilament bundles that have been studied in this work. It can be noticed that the Cordenka material has a higher activation energy, a higher molecular weight, higher initial orientation (untwisted), and a higher Young's modulus and ultimate stress (untwisted bundle). The resulting over all of dissolution behaviour depend on the structure of multifilament which

depends on the spinning and treatment parameters during the manufacturing [55, 129].

Sample	Cordenka multifilament	Lyocell multifilament
Twist	No	Yes±15.7°
M_n / kDa	61± 2	42±1. 2
Mass/unit length (g/m)	0.25 ± 0.01	0.028 ± 0.001
Total effective area/mm2	0.18 ±0.01	0.202 ± 0.001
Average P_2 for Unprocessed	0.57	0.45
E / GPa/ Extrapolated	14.8	10
Ultimate stress/MPa Extrapolated	483	273
$E_a kJ/mol$	169 ± 13	150 ± 13
Fraction of dissolution at 45℃ for 1 hr at 35℃ as reference temperature.	60% dissolved	45% dissolved

Table 5-3: comparison between Cordenka and Lyocell multifilament in various factors.

5.5 Comparison Between the mixing rule of the Cordenka Multifilament and Lyocell Multifilament Composites for Young's Modulus.

The Young's modulus data of all the partially dissolved Cordenka multifilament bundle composites followed the upper Voigt (constant strain) rule of mixtures (Figure 5.19). This shows that an excellent composite was formed which a tendency to follow the parallel rule of mixtures, indicating excellent compatibility between fibres and matrix (equal strain between the two components). This importantly confirms that the Cordenka multifilament bundle could give a good composite due to the higher number-average of molecular weight of the material and the geometry of the multifilament bundle (untwisted).

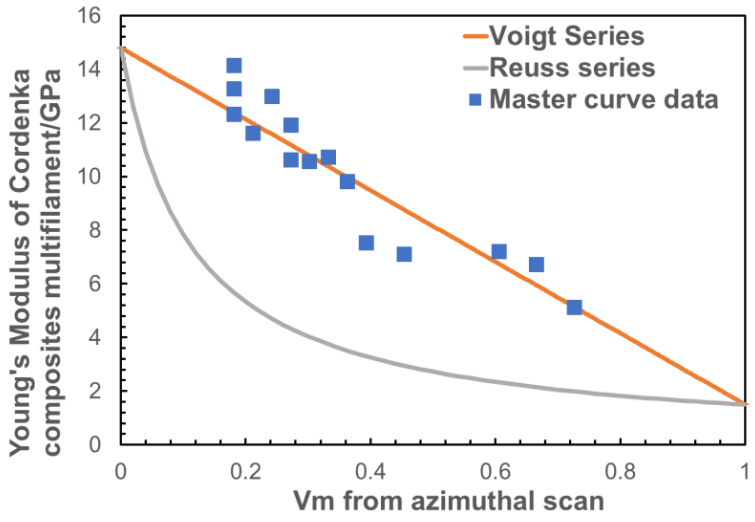

Figure 5.19: Relation between coagulation fraction $C.F$ (from $P2$ measurements) and the measured Young's modulus for the Cordenka composites as compared to the Voight and Reuss rule of mixtures.

On the other hand, the Lyocell Young's Modulus results were highly scattered as shown in Figure 5.20. This could be due to the fact that the lower molecular weight matrix is not such a good 'glue' or that the interior of the Lyocell bundles is not so well stuck together as the IL cannot penetrate.

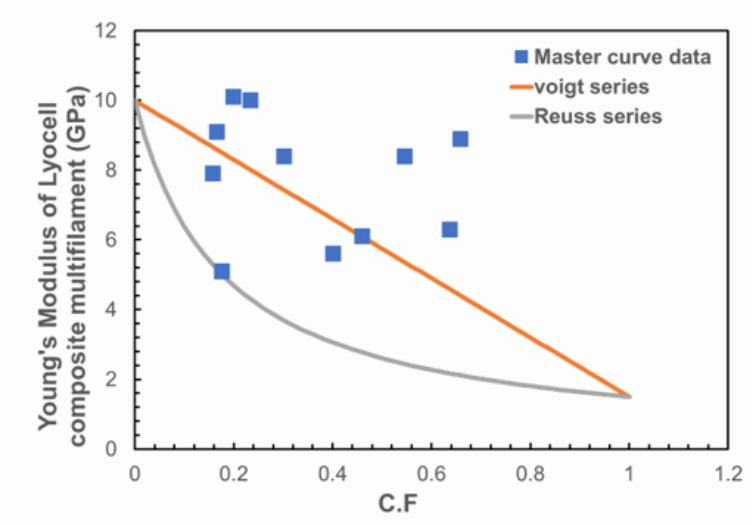

Figure 5.20: Relation between coagulation fraction C.F (from optical measurements) and the measured Young's modulus for the Lyocell composites as compared to the Voight and Reuss rule of mixtures.

5.6 Comparison Between the mixing rules for the Cordenka Multifilament and Lyocell Multifilament Composites for Ultimate Tensile Strength.

The results for the Cordenka multifilament bundle composites for the ultimate tensile strength with volume fraction is shown in Figure 5.21, along with a comparison of the Voigt and Reuss rule of mixtures. It can be noticed that the strength data of Cordenka multifilament bundle also follows the Voigt series

very well. This indicates again that to the matrix is well bounded together with the fibres.

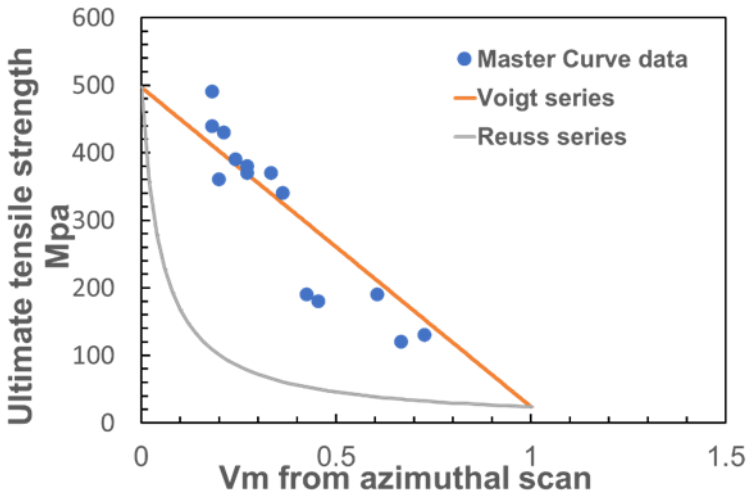

Figure 5.21: Relation between Volume fraction and ultimate tensile strength for the Cordenka multifilament composites in comparison with the Voight and Reuss rule of mixtures.

Figure 5.22 shows the same comparison for the Lyocell composites and, the values here are seen to fall well below the parallel rule of mixtures. We can suggest that this is again due to both the different geometry of the two fibre bundles, and the lower molecular weight of the Lyocell material (and hence the final dissolved matrix phase). It is likely here that either the fibres are not connected together, or the matrix breaks before the fibres.

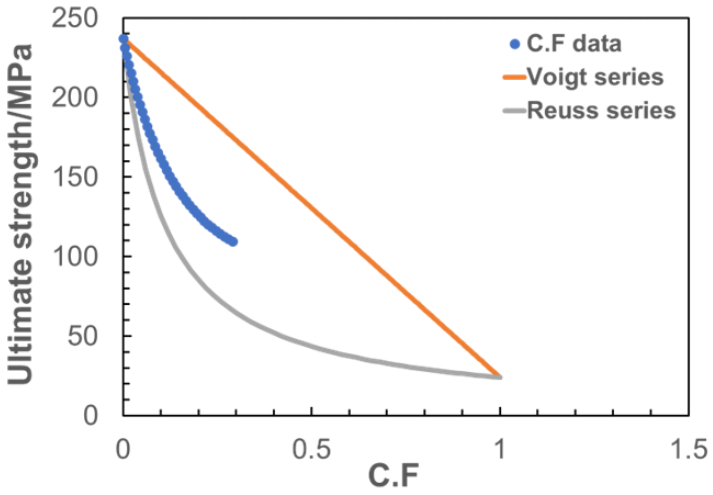

Figure 5.22: Relation between Volume fraction and ultimate stress for the Lyocell multifilament composites in comparison with the Voight and Reuss rule of mixtures.

By using the data of the Ultimate tensile strength measurements from both fibres (here again for a reference temperature of 35°C), it can be seen that the dissolution behaviour of the Cordenka multifilament bundle was faster than the processed Lyocell multifilament bundle as shown in Figure 5.23. This results confirm the results shown earlier in Figure 5.15 using $P2$ measurments.

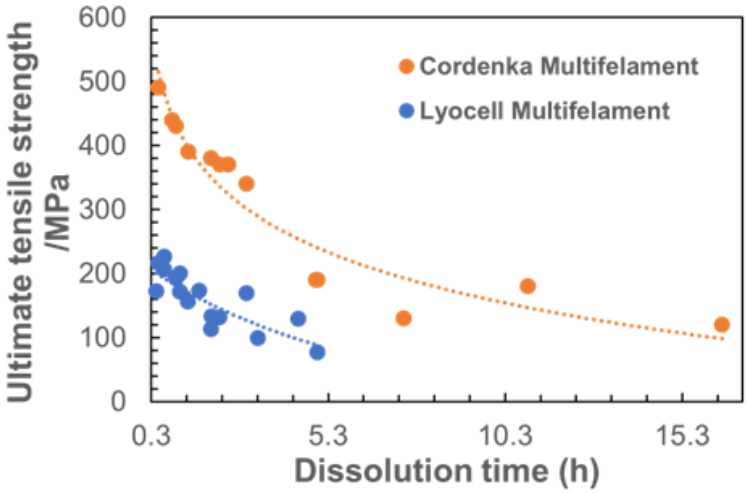

Figure 5.23: comparison between Cordenka and Lyocell multifilament using ultimate tensile strength.

It is clear from the above results in Figures 5.19 and 5.21 that the Cordenka multifilament bundles would make an excellent basis for an all-cellulose composite. However, to weave the bundles, some degree of twist would probably be required, and it would be interesting to explore how this would affect the overall properties. Is there an optimum amount of twist which would allow the IL to penetrate while allowing the fibres to survive a weaving process. Our result suggest that the lowest amount of twist would be preferable.

In terms of making all cellulose composites from the Lyocell Multifilament regenerated fibres, some twist is required to hold the bundles together for weaving and also the fibres have been treated (bleached) to give a bright white colour significantly reducing the molecular weight and leading to embrittlement. However, twist reduces modulus and strength and also slows down the dissolution so our suggestion would be to use as small number of twists as feasible for weaving. A second suggestion to make all cellulose composites from Lyocell multifilament bundle would be to use a two-step process, where the fibres are submersed in a different cellulose solution which could lead to a better matrix and good adhesion between the fibre and matrix.

5.7 Conclusion.

The properties of the Cordenka and the Lyocell multifilament bundles, including geometry, morphology, orientation, dissolution behaviour in the IL [C2mim]+ [OAc]- and the number of molecular weight were studied in this chapter.

From the Optical microscope results, the geometry (untwisted) of the Cordenka multifilament bundle was seen to be comprised of with a few hundred individual multifilament which appeared as a loose microstructure with significant inner spaces in between. The geometry (twisted) of Lyocell multifilament bundle with few hundred of individual fibres are much closer to each other without significant inner spaces.

2D WAXS images, and quantitative P2 measurements, showed that the main crystalline circumferential peak was narrower for the Cordenka multifilament bundle compared to the Lyocell multifilament bundle, which was attributed the bundle twist. In terms of orientation, the angle of twisting of the unprocessed Lyocell multifilament bundle was measured using image j software and found to be $\pm 16.2 \pm 0.6°$.

Although there are clear differences between the orientation and geometry of the Cordenka multifilament and Lyocell multifilament bundles, all data was found to follow Time temperature superposition. In terms of molecular weight, Mn and Mw, the molecular weight of Lyocell multifilament bundle was smaller than the Cordenka multifilament. As shown in Table 5.6, it is seen that the Cordenka multifilament bundle has a higher value of crystalline orientation, Young's modulus, ultimate stress, and activation energy compared to the Lyocell multifilament bundle. These findings especially the geometry and molecular weight lead to the Cordenka multifilament bundle having a faster dissolution rate than the Lyocell multifilament bundle. It is clear from the above results that the Cordenka multifilament bundle would make an excellent basis for an all-cellulose composite. To weave the bundles, some degree of twist

would probably be required, and it would be interesting to explore how this would affect the overall properties.

Chapter 6 Conclusion and outcomes

6.1 Research Outcomes.

This project was focused on an investigation of the dissolution behaviour of two regenerated cellulose multifilament bundles, Cordenka and Lyocell, in the ionic liquid [C2mim][OAc], at different times and temperatures. Using three key experimental methods, namely optical microscopy, X-Ray wide angle diffraction (WAXS) and mechanical testing, it proved possible to follow the dissolution with time and temperature of these two regenerated fibres. Both the coagulation fraction (a measure of dissolution) and the mechanical properties of the partially dissolved fibre composite bundles were found to follow time temperature dissolution, allowing an activation energy to be determined. Also, the speed of dissolution of the two multifilament bundles was compared and was linked to the different geometry of the Cordenka and Lyocell, which were untwisted and twisted respectively.

6.1.1 Introduction chapter

This chapter has presented the previous published studies from the literature, which were interested in regenerated cellulose, in particular the production process and the properties of multifilament bundle of Cordenka and Lyocell, in addition to the dissolution mechanism of cellulose in different ionic liquids.

The results of this PhD study are summarised in chapters 3, 4 and 5. Starting with **chapter 3.**

6.1.2 Dissolution of Cordenka multifilament bundle in the Ionic liquid of 1- ethyl-3-methyl- imidazolium acetate

This chapter was studied the dissolution of Cordenka multifilament bundles in the IL [C2mim] [OAc]. Various methods were used to examine both the dissolution and the properties of the resulting composite multifilament bundle. 2θ WAXS was used as the main qualitative measurement of the dissolution of the Cordenka multifilament bundle. 2θ WAXS scans and a 2D X-ray image showed that the unprocessed Cordenka multifilament bundle comprised the combination of cellulose II and amorphous, with a small (and unexpected) amount of cellulose I. Optical microscopy provided cross-sectional images of both unprocessed and processed composite multifilament bundles. It was found that the cross-sectional size of the processed multifilament bundle decreased with an increase of the coagulation fraction (the matrix proportion) during the dissolution process. We concluded that this method was insufficient to study quantitatively the volume fraction of dissolution as it proved difficult to distinguish between dissolved matrix and original fibres using ImageJ.

Therefore, other techniques were investigated for obtaining a quantitative measure of the dissolution of the Cordenka multifilament bundles, and the two most successful were found from an azimuthal α scan of X-ray diffraction and mechanical testing of the partially dissolved bundles. These methods allowed to follow quantitatively the physics of the dissolution.

The azimuthal α scan, at a chosen angle 2θ=20.3° (close to the 200 reflection and the position of maximum intensity) was used to follow the change in the crystal orientation with time and temperature of dissolution. We here made the

assumption that the orientation of the partially dissolved multifilament bundle (from a calculation of P_2 for each sample) followed a rule of mixtures between the P_2 of the original fibres and that of a completely dissolved sample. P_2 values were found for each sample processed at different times and temperatures and then used to calculate the volume fraction (coagulated fraction) of the processed Cordenka multifilament bundle. The measured values of P_2 for the processed composite multifilament was found to decrease as time and temperature increased, indicating an increase in the random orientated crystal fraction associated with the dissolved and coagulated matrix fraction. The time-temperature superposition method was applied to this experimental data of the average P_2 values. The data set was transformed used time-temperature superposition to form a master curve at particular reference temperatures and then the activation energy was calculated using an Arrhenius equation. The activation energy was found to be 151± 3 kJ/mol.

Mechanical tests were carried out on the partially dissolved processed composite multifilament bundle allowing the Young's modulus and ultimate tensile strength to be followed with time and temperature. Both measures were found to fall with time and temperature as expected from the already measured decrease in the average P_2. The activation energies from the Young's modulus and ultimate tensile strength results were found to be 198 ± 28 kJ/mol and 158±40 kJ/mol, respectively. The activation energies values, with the uncertainties obtained from the average P_2 values, Young's modulus and ultimate tensile strength are seen to be comparable, validating the different methods to follow the dissolution behaviour of the Cordenka multifilament bundle regenerated cellulose fibre bundles.

It proved difficult to measure the modulus of the unprocessed Cordenka multifilament bundles due to being untwisted (and also not bonded). Therefore, we extrapolated the values of the measured Young's modulus of the processed Cordenka multifilament bundle composites (from low temperature and early times measurements) giving a prediction of the modulus of the unprocessed Cordenka multifilament bundle to be E_f =14.8 GPa. The rule of mixtures was then applied to all the results from the partially dissolved composite multifilament bundle by using the combination of the extrapolated value of the Young's modulus with the modulus of a completely dissolved and coagulated film E_m =1.5 GPa. This method employed to assess the possibility of the moduli data following either the Voigt or Reuss mixing rules.

For this comparison, the volume fraction of each partially dissolved composite was determined from the P_2, WAXS measurements. It was found that the Young's modulus of the composite filaments fitted very well to the Voigt parallel rule of mixtures, suggesting the dissolved cellulose (obtained by partially dissolving the Cordenka fibres) forms an excellent matrix and results in excellent bonding throughout the multifilament bundles.

A similar approach was used for the measurements of the ultimate tensile strength of the partially dissolved composites bundles. Extrapolating the ultimate tensile strength results (as above for the Young's modulus), gave a value of σ_f = 479 MPa, by using the ultimate tensile strength data of the processed Cordenka multifilament bundle at all time and temperatures. The rule of mixtures was again applied by using the combination of the extrapolated value of the ultimate stress of the unprocessed Cordenka multifilament bundle. The results were again found to follow quite well the

upper (Voigt) rule of mixtures, where the matrix volume fraction came from the from the P_2 measurements as above. The molecular weight of Cordenka multifilament bundle was measured externally and was found to be (M_n) 61 ± 2 kDa.

6.1.3 Dissolution of Lyocell multifilament bundle in the Ionic liquid of 1- ethyl-3-methyl- imidazolium acetate

This chapter studied the dissolution of Lyocell multifilament bundle in the IL [C2mim] [OAc]. The same methods were used to follow the dissolution with time and temperature as in Cordenka chapter, although for the Lyocell multifilament bundles, direct optical microscopy proved to be the most successful method.

The optical microscopy method proved to offer a direct method to measure the growing area of the dissolved and coagulated Lyocell multifilament bundle samples with increasing time and temperature. The result showed that the twisted nature of Lyocell multifilament bundle meant that the dissolved fibres immediately formed a ring on the outside of the original multifilament bundle. This led to two areas that could be used to follow dissolution, the inner core (the undissolved multifilament bundle) and the outer layer (the dissolved fraction). This allowed measurement of the decrease of the inner core and the increase in the area and thickness of the dissolved and coagulated outer ring using optical micrographs and ImageJ.

It was found that for the lowest dissolution temperature of 30°C and dissolution times of 1, 2 3 and 5 hours, insufficient dissolved matrix was produced to be

easily measurable in the optical micrographs. Due to this reason, the calculation of the coagulation fraction C.F started from 35℃ to 45℃ with times between 30 mins and 5 hrs. The results showed that the area of the undissolved multifilament bundle (inner area) reduced in size with time and temperature, but this was replaced with the dissolved and coagulated matrix fraction and so the outer (total) layer area was found to be independent of time and temperature. We summarize that this is because the density of outer dissolved ring is very similar to the original multifilament bundle. This is unsurprising as the original multifilament of regenerated multifilament bundle contained no significant internal voids, unlike virgin plant fibres which have significant internal voiding. For this reason, the outer area method could not be used to follow the dissolution process and an activation energy could not be determined.

However, two direct methods could be used to determine an activation energy as both were found to follow time temperature superposition. These were the decrease in size of the original bundle (termed the ‘inner area’) and the thickness of the outer ring of dissolved and coagulated material. Interestingly, the thickness of the outer region was found to increase linearly with time (so a constant wavefront of dissolution), at a speed that also increased linearly with temperature for the temperature range studied.

The coagulation fraction C.F was also calculated, from the ratio between the inner core (remaining fibres) and the outer layer (dissolve fraction) areas, and it was found that this increased with increasing time and temperature.

All three measures of dissolution, that is the decreasing size of the inner core (remaining fibres), the absolute thickness (x) of the dissolved layer and the

coagulated fraction C.F, were all found to follow time temperature superposition, all followed Arrhenius behaviour and gave comparable values of the dissolution activation energy. For the inner core (remaining fibres), the absolute thickness (x) of the dissolved layer and the coagulated fraction C.F these were 140 ± 30 kJ/mol, 127 ± 14 kJ/mol and 141± 16 kJ/mol respectively.

A 2θ WAXS scans was used as a qualitatively measurement of the Lyocell multifilament bundle crystal structure. This measurement presented that the unprocessed Lyocell multifilament bundle contains the combination of cellulose II and amorphous, with a very small amount of cellulose I.

An azimuthal α scan of X-ray diffraction and mechanical testing used as quantitative methods to measure the dissolution behave of Lyocell multifilament bundle. An azimuthal α scan was employed at an angle 2θ=20.3° to determine the dissolution mechanism of the Lyocell multifilament bundle by following the change in the average crystalline orientation with time and temperature of dissolution and hence calculate the volume fraction of the dissolved fraction.

The P_2 value of the unprocessed multifilament bundle was found to be 0.45 (lower than the Cordenka multifilament bundles due to these bundles being twisted). The measured value of P_2 for the partially dissolved composite multifilament bundle decreased as time and temperature increased, this indicating an increase in the random orientated crystal fraction associated with the dissolved and coagulated matrix fraction. The rule of mixtures was applied to the P_2 data from the azimuthal α scan to calculate the volume fraction v_m of processed Lyocell multifilament bundle, assuming that the orientation of the original fibres (including the twist) did not change with time and temperature.

The values of Young's modulus from mechanical testing were measured for different processing times and temperatures. The Young's modulus values of the processed Lyocell composite multifilament bundle were found to show significant scatter (compared to the previous Cordenka results). We speculate that this could be due to the poor bonding and brittle nature of the dissolved Lyocell material, but also the twisted nature of the bundles did allow the IL to penetrate and so there could also be insufficient matrix in the Lyocell bundle interior. For this reason, this data could not be used for TTS measurements.

The time-temperature superposition method was applied to the experimental data of the average P_2 values, the calculated matrix volume fraction v_m and ultimate stress values of the processed composite multifilament bundle. Each data set was transformed and made a master curve using the time-temperature superposition and then the activation energy calculated by an Arrhenius equation. It found that all three measured parameters followed Arrhenius behaviour. The activation energies for the three measurements P_2, matrix volume fraction v_m and ultimate tensile strength were found to be 199 ± 34 kJ/mol,197 kJ/mol and 144 ±27 kJ/mol, respectively. The overall average of activation energy value was found 158 ± 13 kJ/mol GPa from different methods. But the activation energy from $P2$ found most confident for the two materials that could be used. By extrapolating the ultimate tensile strength value of the unprocessed Lyocell multifilament bundle for all times and temperatures found σ_f = 237 MPa. This value combined and used with the ultimate tensile strength value of a completely dissolved and coagulated film of Cordenka multifilament bundle, to test the ultimate stress values against the rules of mixture. The correlation between volume fraction from C.F.

measurements and the ultimate stress was lower mixing rules (Voigt series) as the Lyocell multifilament bundle did not contain enough matrix to bounded together with fibre. The molecular weight of Cordenka multifilament bundle was measured externally and was found to be (M_n) 42$\pm$ 1.2 kDa.

6.1.4 A comparison of the Dissolution Behaviour of Cordenka and Lyocell Regenerated Cellulose Multifilament Bundles in the Ionic Liquid [C2mim]+ [OAc]-

Theis chapter studied the difference of the dissolution process for both Cordenka and Lyocell multifilament bundle by comparing their properties of geometry, morphology, orientation, dissolution behaviour in the IL [C2mim]+ [OAc]- and the number of molecular weight. Starting with optical microscopy results were found that the unprocessed Cordenka multifilament bundle has geometry (untwisted) with a few hundred individual filaments which appeared as a loose microstructure with significant inner spaces. In contrast, the Lyocell multifilament bundle have geometry (twisted) of with few hundred of individual fibres are close to each other.

X-ray 2D photographs showed that the crystal structure of the two fibres is very similar and each multifilament bundle is mixture of predominantly cellulose II and amorphous and a small fraction of cellulose I. The 2D pictures of the Cordenka multifilament bundle showed that main Bragg peak (200) was quite narrow with outer smaller 012 peaks which had a similar FWHM. In comparison, the main peak 200 peak for the Lyocell multifilament bundle was

much wider. The twist angle of the unprocessed Lyocell multifilament was measured by image J to be $\pm 15.7^0$, which explains the wider peak.

All the data of the Cordenka multifilament and Lyocell multifilament bundles was found to follow Time -Temperature Superposition (TTS) and then used to calculate the activation energy. The activation energy from $P2$ found most confident for the two materials that could be used for each fibre were 151 ± 3 kJ/mol and 199 ± 34 kJ/mol for the Cordenka multifilament and Lyocell multifilament bundles respectively.

In terms of molecular weight, Mn and Mw, the molecular weight of the Lyocell multifilament bundle was smaller than the Cordenka multifilament bundle, suggesting that the lower activation energy could be linked to this. In summary, the results showed that the Cordenka original multifilament bundle have higher values of orientation, Young's modulus, ultimate stress, and also activation energy compared to the Lyocell multifilament bundle. We suggest that the first three parameters are due to the fact that the Lyocell multifilament bundles are twisted, while the Cordenka multifilament bundles are untwisted, while the activation energy could be more influenced by the molecular weight.

The dissolution fraction, at the same temperature 45 ℃ and time 1hr, for the Cordenka partially dissolved composite multifilament bundle was 60 % (from the P_2 measurements), while the dissolution fraction of the Lyocell multifilament bundle composite was 45% (directly from the optical microscopy measurements). We can speculate that the twisted geometry of the Lyocell multifilament bundles does not allow the IL to penetrate as quickly as the untwisted Cordenka multifilament bundles.

These findings, especially the comparative geometry (untwisted fibres), the speed of dissolution and the higher molecular weight, lead to the important conclusion that the Cordenka multifilament bundle would make an excellent basis for an all- cellulose regenerated fibre composite (ACC). However, if a woven cloth is to be used for ACC production, then some degree of twist would probably be required, and it would be interesting to explore how this would affect the overall properties. Some twist is required to hold the bundles together for weaving. However, twist reduces modulus and strength and also slows down the dissolution so our suggestion would be to use as small number of twists as feasible for weaving. This could prove an interesting area for future research in manufacturing all-cellulose composites from regenerated fibres.

As final conclusion the Cordenka fibre with minimum of amount of twist required for weaving would make an excellent basis for an all cellulose composite combining high stiffness and strength with matrix and mechanical properties.

6.2 References.

[1] Terinte, N., Ibbett, R., and Schuster, K. C. J. L. B., Overview on native cellulose and microcrystalline cellulose I structure studied by X-ray diffraction (WAXD): Comparison between measurement techniques. 2011. **89**: p. 118-131.

[2] Ohira, K., et al., Design of cellulose dissolving ionic liquids inspired by nature. *ChemSusChem*, 2012. **5**(2): p. 388-391.

[3] Phyo, P., et al., Direct determination of hydroxymethyl conformations of plant cell wall cellulose using 1H polarization transfer solid-state NMR. *Biomacromolecules*, 2018. **19**(5): p. 1485-1497.

[4] Gautam, S., et al., A review on systematic study of cellulose. *Journal of Applied and Natural Science*, 2010. **2**(2): p. 330-343.

[5] Samiee, S., et al., Algae as a source of microcrystalline cellulose, in *Advanced bioprocessing for alternative fuels, biobased chemicals, and bioproducts*. 2019, Elsevier. p. 331-350.

[6] McKeen, L. W., 3 - Plastics Used in Medical Devices, in *Handbook of Polymer Applications in Medicine and Medical Devices*, K. Modjarrad and S. Ebnesajjad, Editors. 2014, William Andrew Publishing: Oxford. p. 21-53.

[7] Eriksen, M., et al., Plastic pollution in the South Pacific subtropical gyre. *Marine pollution bulletin*, 2013. **68**(1-2): p. 71-76.

[8] Nishino, T., Matsuda, I., and Hirao, K., All-cellulose composite. *Macromolecules*, 2004. **37**(20): p. 7683-7687.

[9] Mat Salleh, M., et al., Parametric optimization of the processing of all-cellulose composite laminae. *Advanced Manufacturing: Polymer & Composites Science*, 2017. **3**(2): p. 73-79.

[10] Nishino, T. and Arimoto, N. J. B., All-cellulose composite prepared by selective dissolving of fiber surface. 2007. **8**(9): p. 2712-2716.

[11] Huber, T., et al., A critical review of all-cellulose composites. 2012. **47**(3): p. 1171-1186.

[12] Kalia, S., et al., Cellulose-based bio-and nanocomposites: a review. *International journal of polymer science* 2011. **2011**.

[13] Notley, S. M., Pettersson, B., and Wågberg, L., Direct measurement of attractive van der Waals' forces between regenerated cellulose surfaces in an aqueous environment. *Journal of the American Chemical Society*, 2004. **126**(43): p. 13930-13931.

[14] Cousins, S. K. and Brown Jr, R. M., Cellulose I microfibril assembly: computational molecular mechanics energy analysis favours bonding by van der Waals forces as the initial step in crystallization. *Polymer*, 1995. **36**(20): p. 3885-3888.

[15] Bluhm, T. L. and Sarko, A., Packing analysis of carbohydrates and polysaccharides. V. Crystal structures of two polymorphs of pachyman

triacetate. *Biopolymers: Original Research on Biomolecules*, 1977. **16**(9): p. 2067-2089.

[16] Pinkert, A., et al., Ionic liquids and their interaction with cellulose. 2009. **109**(12): p. 6712-6728.

[17] French, A. D., Glucose, not cellobiose, is the repeating unit of cellulose and why that is important. *Cellulose*, 2017. **24**(11): p. 4605-4609.

[18] Payen, A. J. C. r., Mémoire sur la composition du tissu propre des plantes et du ligneux. 1838. **7**: p. 1052-1056.

[19] Postek, M. T., et al., *Production and applications of cellulose*. 2013: Tappi Press. Peachtree Corners.

[20] Wertz, J.-L., Mercier, J. P., and Bédué, O., *Cellulose science and technology*. 2010: EPFL press.

[21] Sescousse, R., et al., Viscosity of cellulose− imidazolium-based ionic liquid solutions. *The Journal of Physical Chemistry* 2010. **114**(21): p. 7222-7228.

[22] Eo, M. Y., et al., Cellulose membrane as a biomaterial: from hydrolysis to depolymerization with electron beam. *Biomaterials Research*, 2016. **20**(1): p. 1-13.

[23] Zugenmaier, P., Conformation and packing of various crystalline cellulose fibers. *Progress in polymer science* 2001. **26**(9): p. 1341-1417.

[24] Revol, J. F. and Goring, D., On the mechanism of the mercerization of cellulose in wood. *Journal of Applied Polymer Science*, 1981. **26**(4): p. 1275-1282.

[25] Uusi-Tarkka, E.-K., Skrifvars, M., and Haapala, A., Fabricating Sustainable All-Cellulose Composites. *Applied Sciences*, 2021. **11**(21): p. 10069.

[26] Isogai, A., et al., Catalytic oxidation of cellulose with nitroxyl radicals under aqueous conditions. *Progress in Polymer Science*, 2018. **86**: p. 122-148.

[27] Lindman, B., Karlström, G., and Stigsson, L., On the mechanism of dissolution of cellulose. *Journal of molecular liquids*, 2010. **156**(1): p. 76-81.

[28] Khodayari, A., et al., Tensile behaviour of dislocated/crystalline cellulose fibrils at the nano scale. *Carbohydrate polymers*, 2020. **235**: p. 115946.

[29] Varlas, S., et al., Self-assembled nanostructures from amphiphilic block copolymers prepared via ring-opening metathesis polymerization (ROMP). *Progress in Polymer Science*, 2020. **107**: p. 101278.

[30] Glasser, W. G., et al., About the structure of cellulose: debating the Lindman hypothesis. *Cellulose*, 2012. **19**: p. 589-598.

[31] Langan, P., Nishiyama, Y., and Chanzy, H., A revised structure and hydrogen-bonding system in cellulose II from a neutron fiber diffraction

analysis. *Journal of the American Chemical Society*, 1999. **121**(43): p. 9940-9946.

[32] Northolt, M., et al., The structure and properties of cellulose fibres spun from an anisotropic phosphoric acid solution. *Polymer*, 2001. **42**(19): p. 8249-8264.

[33] Cuissinat, C. and Navard, P. *Swelling and Dissolution of Cellulose Part 1: Free Floating Cotton and Wood Fibres in N-Methylmorpholine-N-oxide–Water Mixtures*. in *Macromolecular Symposia*. 2006. Wiley Online Library.

[34] Chanzy, H., Cellulose-amine oxide systems. *Carbohydrate Polymers*, 1982. **2**(4): p. 229-231.

[35] Heinze, T. and Koschella, A., Solvents applied in the field of cellulose chemistry: a mini review. *Polímeros*, 2005. **15**: p. 84-90.

[36] Sayyed, A. J., Deshmukh, N. A., and Pinjari, D. V., A critical review of manufacturing processes used in regenerated cellulosic fibres: viscose, cellulose acetate, cuprammonium, LiCl/DMAc, ionic liquids, and NMMO based lyocell. *Cellulose*, 2019. **26**(5): p. 2913-2940.

[37] Hall, C. A., et al., Macroscopic and microscopic study of 1-ethyl-3-methyl-imidazolium acetate–water mixtures. *The Journal of Physical Chemistry*, 2012. **116**(42): p. 12810-12818.

[38] Pinkert, A., et al., Ionic liquids and their interaction with cellulose. *Chemical reviews*, 2009. **109**(12): p. 6712-6728.

[39] Walden, P., Molecular weights and electrical conductivity of several fused salts. *Bull. Acad. Imper. Sci.(St. Petersburg)*, 1914. **1800**.

[40] Zavrel, M., et al., High-throughput screening for ionic liquids dissolving (ligno-) cellulose. *Bioresource technology* 2009. **100**(9): p. 2580-2587.

[41] Seydibeyoğlu, M. Ö. and Oksman, K., Novel nanocomposites based on polyurethane and micro fibrillated cellulose. *Composites Science and Technology*, 2008. **68**(3-4): p. 908-914.

[42] Zhang, J., et al., Application of ionic liquids for dissolving cellulose and fabricating cellulose-based materials: state of the art and future trends. *Materials Chemistry Frontiers*, 2017. **1**(7): p. 1273-1290.

[43] Swatloski, R. P., et al., Dissolution of cellose with ionic liquids. *Journal of the American chemical society*, 2002. **124**(18): p. 4974-4975.

[44] Ghandi, K. J. G. and chemistry, s., A review of ionic liquids, their limits and applications. 2014. **4**(01): p. 44.

[45] Joglekar, H. G., et al., The path ahead for ionic liquids. 2007. **30**(7): p. 819-828.

[46] Sun, N., et al., Complete dissolution and partial delignification of wood in the ionic liquid 1-ethyl-3-methylimidazolium acetate. *Green Chemistry*, 2009. **11**(5): p. 646-655.

[47] Köhler, S., et al., Interactions of Ionic Liquids with Polysaccharides 1. Unexpected Acetylation of Cellulose with 1-Ethyl-3-methylimidazolium

Acetate. *Macromolecular Rapid Communications* 2007. **28**(24): p. 2311-2317.

[48] Liebner, F., et al., Thermal aging of 1-alkyl-3-methylimidazolium ionic liquids and its effect on dissolved cellulose. 2010.

[49] Zweckmair, T., et al., On the mechanism of the unwanted acetylation of polysaccharides by 1, 3-dialkylimidazolium acetate ionic liquids: Part 1—Analysis, acetylating agent, influence of water, and mechanistic considerations. *Cellulose*, 2015. **22**: p. 3583-3596.

[50] Bowron, D., et al., Structure and dynamics of 1-ethyl-3-methylimidazolium acetate via molecular dynamics and neutron diffraction. *The Journal of Physical Chemistry B*, 2010. **114**(23): p. 7760-7768.

[51] Adusumalli, R. B., et al. *Tensile testing of single regenerated cellulose fibres*. in *Macromolecular Symposia*. 2006. Wiley Online Library.

[52] Cuissinat, C. and Navard, P. *Swelling and dissolution of cellulose part II: Free floating cotton and wood fibres in NaOH–water–additives systems*. in *Macromolecular Symposia*. 2006. Wiley Online Library.

[53] Woodings, C., A brief history of regenerated cellulosic fibers. *Regenerated cellulose fibers*, 2001: p. 1-21.

[54] Shen, L. and Patel, M. K., Life cycle assessment of man-made cellulose fibres. *Lenzinger Berichte*, 2010. **88**: p. 1-59.

[55] Woodings, C., Regenerated Cellulose Fibres. 2001, Woodhead Publishing.

[56] Zhu, C., et al., High modulus regenerated cellulose fibers spun from a low molecular weight microcrystalline cellulose solution. *ACS Sustainable Chemistry & Engineering*, 2016. **4**(9): p. 4545-4553.

[57] Yu, M.-c. and Wan, J.-x., Environmental friendly development of regenerated cellulose fiber production. *DEStech Transactions on Engineering and Technology Research*, 2017(apetc).

[58] Wang, S., Lu, A., and Zhang, L., Recent advances in regenerated cellulose materials. *Progress in Polymer Science*, 2016. **53**: p. 169-206.

[59] Meredith, J., et al., On the static and dynamic properties of flax and Cordenka epoxy composites. *Composites Science and Technology* 2013. **80**: p. 31-38.

[60] Cordenka. Reinforcement of tires and other rubber products. 2022 20 JUN 2022; Available from: https://www.cordenka.com/en/rayon-cord-and-fabric.

[61] Chen, F., et al., Swelling and dissolution kinetics of natural and man-made cellulose fibers in solvent power tuned ionic liquid. *Cellulose*, 2020. **27**: p. 7399-7415.

[62] The composites materials Handbook-MIL 17, Materials, usage, Design and Analysis. *Technomic publishing company, Inc. 851 new Holland Avenue, Box 3535, Lancaster, Pennsylvania 17604, USA.*, Access to website on 4.4.2019. **3**.

[63] Gindl, W. and Keckes, J. J. P., All-cellulose nanocomposite. 2005. **46**(23): p. 10221-10225.

[64] Nishino, T., Matsuda, I., and Hirao, K. J. M., All-cellulose composite. 2004. **37**(20): p. 7683-7687.

[65] Duchemin, B. J., et al., All-cellulose composites by partial dissolution in the ionic liquid 1-butyl-3-methylimidazolium chloride. 2009. **40**(12): p. 2031-2037.

[66] Zhao, Q., et al., Novel all-cellulose ecocomposites prepared in ionic liquids. *Cellulose*, 2009. **16**(2): p. 217-226.

[67] Hajlane, A., et al., Chemical modification of regenerated cellulose fibres by cellulose nano-crystals: towards hierarchical structure for structural composites reinforcement. 2017. **100**: p. 41-50.

[68] Zhao, Q., et al., Novel all-cellulose ecocomposites prepared in ionic liquids. 2009. **16**(2): p. 217-226.

[69] Hermanutz, F., et al., Processing of Cellulose Using Ionic Liquids. *Macromolecular Materials and Engineering*, 2019. **304**(2): p. 1800450.

[70] Amash, A. and Zugenmaier, P., Morphology and properties of isotropic and oriented samples of cellulose fibre–polypropylene composites. *Polymer*, 2000. **41**(4): p. 1589-1596.

[71] Seavey, K. C., et al., Continuous cellulose fiber-reinforced cellulose ester composites. I. Manufacturing options. *Cellulose*, 2001. **8**: p. 149-159.

[72] Ganster, J., Fink, H.-P., and Pinnow, M., High-tenacity man-made cellulose fibre reinforced thermoplastics–injection moulding compounds with polypropylene and alternative matrices. *Composites Part A: Applied Science and Manufacturing*, 2006. **37**(10): p. 1796-1804.

[73] Ganster, J. and Fink, H.-P. J. C., Novel cellulose fibre reinforced thermoplastic materials. 2006. **13**(3): p. 271-280.

[74] Alrefaei, N. S., Hine, P. J., and Ries, M. E., Dissolution of hemp yarns by 1-ethyl-3-methylimidazolium acetate studied with time-temperature superposition. *Cellulose*, 2023: p. 1-17.

[75] Albarakati, F. A., Hine, P. J., and Ries, M. E., Effect of water on the dissolution of flax fiber bundles in the ionic liquid 1-ethyl-3-methylimidazolium acetate. *Cellulose*, 2023. **30**(12): p. 7619-7632.

[76] Hawkins, J. E., et al., Time temperature superposition of the dissolution of cellulose fibres by the ionic liquid 1-ethyl-3-methylimidazolium acetate with cosolvent dimethyl sulfoxide. *Carbohydrate Polymer Technologies and Applications*, 2021. **2**: p. 100021.

[77] Liang, Y., et al., Dissolution of cotton by 1-ethyl-3-methylimidazolium acetate studied with time–temperature superposition for three different fibre arrangements. *Cellulose*, 2021. **28**: p. 715-727.

[78] Victoria, A., et al., Design of experiments in the optimization of all-cellulose composites. *Cellulose*, 2023: p. 1-27.

[79] Mansikkamäki, P., Lahtinen, M., and Rissanen, K., The conversion from cellulose I to cellulose II in NaOH mercerization performed in alcohol–water systems: An X-ray powder diffraction study. *Carbohydrate Polymers*, 2007. **68**(1): p. 35-43.

[80] Morgenstern, B. and Kammer, H.-W., On the particulate structure of cellulose solutions. *Polymer*, 1999. **40**(5): p. 1299-1304.

[81] Oladapo, B. I., Oshin, E. A., and Olawumi, A. M., Nanostructural computation of 4D printing carboxymethylcellulose (CMC) composite. *Nano-Structures & Nano-Objects*, 2020. **21**: p. 100423.

[82] Grząbka-Zasadzińska, A., Skrzypczak, A., and Borysiak, S., The influence of the cation type of ionic liquid on the production of nanocrystalline cellulose and mechanical properties of chitosan-based biocomposites. *Cellulose*, 2019. **26**: p. 4827-4840.

[83] Voronova, M. I., et al., The effect of drying technique of nanocellulose dispersions on properties of dried materials. *Materials letters*, 2012. **68**: p. 164-167.

[84] Gu, B. and Burgess, D. J., Polymeric materials in drug delivery, in *Natural and Synthetic Biomedical Polymers*. 2014, Elsevier. p. 333-349.

[85] Girolami, G. S., X-Ray Crystallography. 2016, University Science Books.

[86] Kohli, R., Methods for monitoring and measuring cleanliness of surfaces, in *Developments in Surface Contamination and Cleaning: Detection, Characterization, and Analysis of Contaminants*. 2012, Elsevier. p. 107-178.

[87] Bunaciu, A. A., UdriŞTioiu, E. G., and Aboul-Enein, H. Y. J. C. R. i. A. C., X-ray diffraction: instrumentation and applications. 2015. **45**(4): p. 289-299.

[88] Le Pevelen, D. D., Small Molecule X-Ray Crystallography, Theory and Workflow. 2010.

[89] Thompson, W. J. J. C. i. P., Numerous neat algorithms for the Voigt profile function. 1993. **7**(6): p. 627-631.

[90] Wada, M. and Okano, T., Localization of Iα and Iβ phases in algal cellulose revealed by acid treatments. *Cellulose*, 2001. **8**: p. 183-188.

[91] Pang, J., Mehandzhiyski, A. Y., and Zozoulenko, I., A computational study of cellulose regeneration: Coarse-grained molecular dynamics simulations. *Carbohydrate Polymers*, 2023. **313**: p. 120853.

[92] Poletto, M., Pistor, V., and Zattera, A. J., Structural characteristics and thermal properties of native cellulose. *Cellulose-fundamental aspects*, 2013. **2**: p. 45-68.

[93] Howell, C. L., Understanding wood biodegradation through the characterization of crystalline cellulose nanostructures. 2008, University of Maine.

[94] Sawada, D., et al., Tension wood structure and morphology conducive for better enzymatic digestion. *Biotechnology for biofuels*, 2018. **11**(1): p. 44.

[95] Ciolacu, D., Ciolacu, F., and Popa, V. I., Amorphous cellulose—structure and characterization. *Cellulose chemistry and technology*, 2011. **45**(1): p. 13.

[96] Lafrance, C.-P., et al., On the relationship between the order parameter and the shape of orientation distributions. *Canadian journal of chemistry*, 1995. **73**(9): p. 1497-1505.

[97] Rusznák, I., et al., ANALYSIS OF THE ORIENTATION OF POLYPROPYLENE-BASED SHEETS SUITABLE FOR FIBRILLATED YARN PRODUCTION. *Periodica Polytechnica Chemical Engineering*, 1975. **19**(3): p. 201-217.

[98] Mwaikambo, L. Y. and Ansell, M. P., The determination of porosity and cellulose content of plant fibers by density methods. *Journal of materials science letters*, 2001. **20**(23): p. 2095-2096.

[99] Sun, C. C., True density of microcrystalline cellulose. *Journal of pharmaceutical sciences*, 2005. **94**(10): p. 2132-2134.

[100] Lakes, R. and Drugan, W., Dramatically stiffer elastic composite materials due to a negative stiffness phase? *Journal of the Mechanics and Physics of Solids*, 2002. **50**(5): p. 979-1009.

[101] Luo, Y., Isotropized Voigt-Reuss model for prediction of elastic properties of particulate composites. *Mechanics of Advanced Materials and Structures*, 2021: p. 1-13.

[102] William D. Callister, J., An Introduction Materials Science and Engineering *John Wiley & Sons, Inc.*, 2007. **chapter 16**(7th edition): p. 585-589.

[103] Liang, Y., et al., Dissolution of cotton by 1-ethyl-3-methylimidazolium acetate studied with time–temperature superposition for three different fibre arrangements. *Cellulose*, 2021. **28**(2): p. 715-727.

[104] Chimestry, L. The Arrhenius Law- Activation Energies. 2022 17 Oct Available from: https://chem.libretexts.org.

[105] Olowoyo, S. O., Kinetics and Activation Energy Parameters for Hydrolysis of Acetic Anhydride in a Water-Acetone Cosolvent System. 2018, East Tennessee State University.

[106] Budtova, T. and Navard, P., Viscosity-temperature dependence and activation energy of cellulose solutions. *Nordic Pulp & Paper Research Journal*, 2015. **30**(1): p. 99-104.

[107] Ries, M. E., et al., Microscopic and macroscopic properties of carbohydrate solutions in the ionic liquid 1-ethyl-3-methyl-imidazolium acetate. *The Journal of Physical Chemistry B*, 2018. **122**(37): p. 8763-8771.

[108] Piskulich, Z. A., Mesele, O. O., and Thompson, W. H., Activation energies and beyond. *The Journal of Physical Chemistry A*, 2019. **123**(33): p. 7185-7194.

[109] Vyazovkin, S., Activation energies and temperature dependencies of the rates of crystallization and melting of polymers. *Polymers*, 2020. **12**(5): p. 1070.

[110] Röhrling, J., et al., A novel method for the determination of carbonyl groups in cellulosics by fluorescence labeling. 1. Method development. *Biomacromolecules*, 2002. **3**(5): p. 959-968.

[111] Silbermann, S., et al., Improving molar mass analysis of cellulose samples with limited solubility. *Carbohydrate polymers*, 2017. **178**: p. 302-310.

[112] Cotts, R., et al., Pulsed field gradient stimulated echo methods for improved NMR diffusion measurements in heterogeneous systems. *Journal of Magnetic Resonance (1969)*, 1989. **83**(2): p. 252-266.

[113] Nam, S., et al., Segal crystallinity index revisited by the simulation of X-ray diffraction patterns of cotton cellulose Iβ and cellulose II. *Carbohydrate polymers*, 2016. **135**: p. 1-9.

[114] Brian.P.Grady, Simple SAXS and WAXS Software written in Excel. http://coecs.ou.edu/Brian.P.Grady/saxssoftware, 2018.

[115] Garvey, C. J., Parker, I. H., and Simon, G. P., On the interpretation of X-ray diffraction powder patterns in terms of the nanostructure of cellulose I fibres. *Macromolecular Chemistry and Physics*, 2005. **206**(15): p. 1568-1575.

[116] Daicho, K., et al., The crystallinity of nanocellulose: dispersion-induced disordering of the grain boundary in biologically structured cellulose. *ACS Applied Nano Materials*, 2018. **1**(10): p. 5774-5785.

[117] Driemeier, C. and Calligaris, G. A., Theoretical and experimental developments for accurate determination of crystallinity of cellulose I materials. *Journal of Applied Crystallography*, 2011. **44**(1): p. 184-192.

[118] French, A. D., Idealized powder diffraction patterns for cellulose polymorphs. *Cellulose*, 2014. **21**(2): p. 885-896.

[119] Trilokesh, C. and Uppuluri, K. B., Isolation and characterization of cellulose nanocrystals from jackfruit peel. *Scientific Reports*, 2019. **9**(1): p. 1-8.

[120] Thomas, L. H., et al., Diffraction evidence for the structure of cellulose microfibrils in bamboo, a model for grass and cereal celluloses. *BMC plant biology*, 2015. **15**(1): p. 1-7.

[121] Isogai, A., et al., Solid-state CP/MAS carbon-13 NMR study of cellulose polymorphs. *Macromolecules*, 1989. **22**(7): p. 3168-3172.

[122] Zhang, X., Ries, M. E., and Hine, P. J., Time–Temperature Superposition of the Dissolution of Silk Fibers in the Ionic Liquid 1-Ethyl-3-methylimidazolium Acetate. *Biomacromolecules*, 2021.

[123] Ries, M. E., et al., Diffusion of 1-ethyl-3-methyl-imidazolium acetate in glucose, cellobiose, and cellulose solutions. *Biomacromolecules*, 2014. **15**(2): p. 609-617.

[124] Laidler, K. J., THE DEVELOPMENT OF THE ARRHENIUS EQUATION. *Journal of Chemical Education*, 1984. **61**(6): p. 494-498.

[125] Uto, T., Yamamoto, K., and Kadokawa, J.-i., Cellulose crystal dissolution in imidazolium-based ionic liquids: A theoretical study. *The Journal of Physical Chemistry B*, 2018. **122**(1): p. 258-266.

[126] Sescousse, R. and Budtova, T., Influence of processing parameters on regeneration kinetics and morphology of porous cellulose from cellulose–NaOH–water solutions. *Cellulose*, 2009. **16**: p. 417-426.

[127] Sescousse, R., Gavillon, R., and Budtova, T., Aerocellulose from cellulose–ionic liquid solutions: Preparation, properties and comparison with cellulose–NaOH and cellulose–NMMO routes. *Carbohydrate Polymers*, 2011. **83**(4): p. 1766-1774.

[128] Paul, A., et al., Fick's laws of diffusion. *Thermodynamics, diffusion and the kirkendall effect in solids*, 2014: p. 115-139.

[129] Röder, T., et al., Man-made cellulose fibres–a comparison based on morphology and mechanical properties. *Lenzinger Berichte*, 2013. **91**: p. 7-12.